

**SEISMIC ANISOTROPY IN TIGHT GAS SANDSTONES,  
RULISON FIELD, PICEANCE BASIN, COLORADO**

by

Gerardo J. Franco

A thesis submitted to the Faculty and Board of Trustees of the Colorado School of Mines in partial fulfillment of the requirements for the degree of Master of Science (Geophysical Engineering).

Golden, Colorado

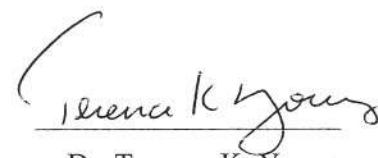
Date April 12, 2007

Signed:   
Gerardo J. Franco

Approved:   
Dr. Thomas L. Davis  
Professor of Geophysics  
Thesis Advisor

Golden, Colorado

Date April 12, 2007

  
Dr. Terence K. Young  
Department Head  
Department of Geophysics

## ABSTRACT

I have integrated borehole seismic, surface seismic, well log data and lab-based rock physics to estimate the seismic anisotropy of the tight gas reservoir at Rulison Field. Seismic anisotropy depends on the reservoir rock quality and can be used to improve reservoir characterization of tight gas sands.

Tight-gas sandstones are important unconventional hydrocarbon resources that contain a quarter of the proven natural gas reserves in the United States. Rulison Field, located in the Piceance Basin, Colorado, produces gas from a thick section of stacked, discontinuous sandstone channels, interbedded with siltstones, shales, and coals. Typically small sizes of the sand channels make them difficult to image with surface seismic data, while low porosities (under 10%) and permeabilities (in the microdarcy range) challenge production.

This research uses different datasets and techniques to demonstrate that anisotropy of tight-gas sandstones at Rulison varies and generally correlates with lithology and fractures. The results are obtained assuming VTI and orthorhombic symmetries.

At the reservoir's overburden (VSP interval) azimuthal anisotropy is evident at small and medium offsets, with an orientation that varies from north to north-west. This azimuthal anisotropy is indicative of an orthorhombic symmetry.

Thomsen anisotropy parameters have been estimated using P-wave VSP inversion and ultrasonic core plugs measurements. For VTI, all the parameters are positive and have a range of  $\epsilon$  values from 0.04 to 0.19,  $\gamma$  values from 0.01 to 0.05 (without including fracture areas),  $\delta$  values from 0.02 to 0.1,  $\eta$  values from 0.02 to 0.08, and  $\sigma$  values from 0.05 to 0.13.

A correlation between high shear wave splitting and lithologies was detected. Fractures are common in sandstones and coal layers. The fracture density increases at least four times in coal zones below the top Cameo coal. A correlation between high shear wave splitting zones and gas concentrations is observed. This correlation suggests that gas migration is enhanced by the natural fracture system at Rulison Field.

P-wave NMO azimuthal anisotropy indicated a high eccentricity area on the west side of the Reservoir Characterization Project (RCP) area that correlates with faults below the Cameo coal layer. Orientation of the fractures within this area shows an N70°W to N85°W preference direction that correlates with observations from well logs and VSP data.

There is a poor correlation between P-wave NMO azimuthal anisotropy and EUR (Estimated Ultimate Recovery) at Rulison Field. This lack of correlation could be caused by the small eccentricity values of NMO ellipses at the reservoir intervals and other geological factors, such as: (1) multiple sets of fractures, (2) sandstone net pay distribution, (3) fault distribution, and (4) compartments within the reservoir.

## TABLE OF CONTENTS

<b>ABSTRACT</b> .....	<b>iii</b>
<b>LIST OF FIGURES</b> .....	<b>ix</b>
<b>LIST OF TABLES</b> .....	<b>xvi</b>
<b>ACKNOWLEDGEMENTS</b> .....	<b>xvii</b>
<b>CHAPTER 1 INTRODUCTION</b> .....	<b>1</b>
1.1 Research Objectives.....	2
1.2 Seismic Anisotropy.....	3
1.3 Rulison Field Description.....	3
1.4 Geological Setting.....	5
1.5 Reservoir Properties.....	12
1.6 Previous Work at Rulison Field.....	14
1.7 Research Approach.....	16
<b>CHAPTER 2 ESTIMATION OF SEISMIC ANISOTROPIC USING CORE PLUGS ULTRASONIC MEASUREMENTS</b> .....	<b>18</b>
2.1 Rock Properties of Core Plugs.....	19
2.1.1 Mineralogy and Cracks of Core Plugs.....	22
2.1.2 Fluid Composition at Rulison Field.....	26
2.2 Seismic Anisotropy Orientation.....	27
2.3 Ultrasonic Seismic Anisotropy Measurements at Varying Confining Pressure.....	30

2.3.1 Experimental Setup.....	30
2.3.2 Elastic Coefficient and Thomsen Parameters Estimation.....	33
2.3.3 Measurement Uncertainties .....	35
2.3.4 Dry Core Plug Ultrasonic Measurements Results .....	36
2.3.5 Discussion of Results.....	38
2.4 Seismic Anisotropy Parameters and Lithology.....	44
2.5 Assumptions and Shortcomings.....	48
2.6 Summary.....	49
<b>CHAPTER 3 ELASTIC PROPERTIES FROM CROSS-DIPOLE SONIC LOGS.</b>	<b>51</b>
3.1 Quality Control of the Data.....	51
3.2 Maximum Stress Orientation and Fractures from Well Logs.....	52
3.3 Shear Wave Splitting and Fracture Analysis .....	54
3.4 Cross-dipole Well Logs .....	54
3.4.1 Well RWF 332-21 .....	54
3.4.2 Well RWF 542-20.....	63
3.4.3 Well RWF 441-20.....	65
3.6 Summary.....	66
<b>CHAPTER 4 ESTIMATION OF SEISMIC ANISOTROPY USING P-WAVE VSP DATA .....</b>	<b>68</b>
4.1 P-wave Slowness-Polarization Technique.....	69
4.1.1 VTI Media.....	69
4.1.2 Orthorhombic Media.....	71

4.2 Anisotropic Parameter Estimation .....	72
4.2.1 VTI Inversion – Polar Anisotropy .....	75
4.2.2 Orthorhombic Inversion – Azimuthal Anisotropy .....	79
4.3 Correlation with Rock Physics Measurements and Cross-dipole Analysis .....	81
4.4 Anisotropy Parameters to Improve Seismic Imaging .....	83
4.5 Summary .....	85
<b>CHAPTER 5 ESTIMATION OF AZIMUTHAL ANISOTROPY USING P-WAVE SEISMIC.....</b>	<b>86</b>
5.1 Quality Control of Surface Seismic Data.....	87
5.2 Processing Sequence.....	89
5.3 Azimuthal Anisotropy Analysis in P-wave Data using Fractograms .....	91
5.4 Azimuthal Anisotropy Results.....	94
5.4.1 Azimuthal Anisotropy Percentage Sections.....	99
5.5 Correlation between Azimuthal Anisotropy Zones and Production Areas.....	103
5.6 Assumptions and Shortcomings of P-wave Azimuthal Anisotropy Analysis .....	104
5.6.1 Multiple Sets of Fractures.....	104
5.6.2 Sandstone Net Pay Distribution.....	106
5.6.3 Fault Distribution.....	107
5.6.4 Compartments .....	109
5.7 Shear Wave Splitting Surface Seismic Analysis .....	110
5.8 Summary .....	111
<b>CHAPTER 6 CONCLUSIONS AND RECOMMENDATIONS .....</b>	<b>113</b>

6.1 Conclusions from this Study.....	113
6.2 Recommendations.....	115
<b>REFERENCES.....</b>	<b>117</b>

## LIST OF FIGURES

- Figure 1-1. RCP study area (inside red rectangle). The main characterization wells are indicated with red dots. These include two 3D VSP, three cross-dipole sonic logs and five image logs. Black dots indicated other wells in the area (more than 80 wells). ..... 4
- Figure 1-2. Rulison Field (shown in green) is located in the Piceance Basin, northwest Colorado. Major gas fields in the area (shown in red) produce from the Williams Fork Formation of the Mesaverde Group. From Hoak and Klawitter (1997) modified by Matesic (2007). ..... 6
- Figure 1-3. Stratigraphic column of the Rulison Field area. Tight gas sandstones are within the Late Cretaceous Mesaverde Group. From Cole and Cumella (2003). ..... 8
- Figure 1-4. Petroleum system events chart showing timing of elements and processes related with to the hydrocarbon generation and accumulation in Piceance basin. From Magoon and Dow (1994) modified by Guliyev (2007). ..... 9
- Figure 1-5. Schematic cross-section showing gas migration model for the Mesaverde Group. From Scheevel and Cumella (2005). ..... 10
- Figure 1-6. Schematic showing the tectonic history of Piceance basin. From Kuuskraa et al. (1997b). ..... 11
- Figure 1-7. Development of major fractures at Rulison Field, Piceance Basin. From Kuuskraa et al. (1997b). ..... 12
- Figure 1-8. Pore pressure gradient measurements as function of depth at the MWX site. Pore pressure increases with depth to progressively higher gradients. Top of the reservoir show in dashed line. From Spencer (1989) modified by Rojas (2005). ..... 14
- Figure 2-1. Horizontal and vertical core plugs. From left to right samples: R-5566H, R-5566V, R-5702H and R-5702V. Vertical scale is shown in centimeters. .... 21
- Figure 2-2. Horizontal and vertical core plugs. From left to right samples: R-5727H, R-5727V, R-6451H and R-6451V. Vertical scale is shown in centimeters. .... 21
- Figure 2-3. SEM pictures of interval 6451 at different magnifications (50x, 100x, 500x, 1000x). A natural fracture (1000x image) shows cementation. From Rojas (2005). ..... 22

Figure 2-4. CAT scan of core plug R-5566H. Laminations occur in multiple directions and produce a highly heterogeneous sample. ....	24
Figure 2-5. CAT scan of core plug R-5702H. Laminations occur in a preference direction (90°).....	24
Figure 2-6. CAT scan of core plug R-5727H. Sample is close to homogeneous without cracks or laminations. ....	25
Figure 2-7. CAT scan of core plug R-6451H. Cracks occur in the direction of 0°.....	25
Figure 2-8. $V_p/V_s$ versus differential pressure for a saturated sample. Fluid substitution using Gassmann's equation was done for 100% water saturation (salinity 25000 ppm), butane, methane and a mixture of gases (85% methane, 10% nitrogen, and 5% ethane), which represents Rulison Field gas. From Rojas (2005). ....	26
Figure 2-9. Schematic showing azimuthal dependence of shear wave propagation in a core sample. Modified from Sondergeld and Rai (1986). ....	28
Figure 2-10. Shear wave velocities at different core sample angles at room pressure conditions.....	29
Figure 2-11. Sample setup for ultrasonic core plug measurements. From Rojas (2005)..	31
Figure 2-12. Schematic showing the P and S-waves measured in the vertical and horizontal samples. At the left is the vertical sample: two pairs of transducers are used to measure the $V_{p0}$ and $V_{p45}$ waves. At right is the horizontal sample: a pair of transducers is used to measured $V_{p90}$ , $V_{SH0}$ and $V_{SH90}$ waves. ....	32
Figure 2-13. Compressional and shear waveforms for the sample 5566H.....	37
Figure 2-14. P and S-wave velocities versus logarithmic pressure for samples at 5566 feet. a) Velocity of P-waves for 0, 45 and 90 degrees. b) Velocity of fast and slow S-waves for 90 degrees.....	39
Figure 2-15. Five components of the stiffness tensor for sample 5566.....	39
Figure 2-16. Thomsen anisotropy coefficient $\epsilon$ (blue line) and $\gamma$ (red line) for samples a) R-5566, b) R-5702, c) R-5727, and d) R-6451.....	40
Figure 2-17. Thomsen anisotropy coefficient $\delta$ (orange line) and $\eta$ (purple line) for samples a) R-5566, b) R-5702, c) R-5727, and d) R-6451.....	41

Figure 2-18. a)  $\gamma$  versus  $\epsilon$  for different core samples at reservoir pressure. Sandstones and siltstones samples with few laminations have low anisotropy and values below 5%. Shaley sandstones with high number of laminations have higher anisotropy values with  $\epsilon$  close to 15% and  $\gamma$  close to 5%. b)  $\delta$  versus  $\epsilon$  for different core samples at reservoir pressure. Shaley sandstones with high number of siltstone laminations have higher anisotropy values with  $\delta$  close to 9%..... 45

Figure 2-19. Shear wave anisotropy versus P-wave anisotropy for different lithologies. a)  $\gamma$  versus  $\epsilon$  for shale, coals, sands and carbonates. From Wang (2002b). b)  $\gamma$  versus  $\epsilon$  for tight gas sands. Created from Wang (2002b)..... 47

Figure 2-20. Well logs and summary of the core sample measurements results. Left column shows a gamma ray normalized log, middle column shows sample number, lithology and anisotropy coefficients and right column shows a NPHI (neutron) and DPHI logs. Pink zones at the right column are possible gas areas. .... 48

Figure 3-1. RWF 332-21 well logs from UMV shale to Cameo coal. From left to right: normalized gamma ray (brown log), shear wave splitting (blue log),  $\epsilon$  estimated from  $\gamma$  (red log), fast and slow shear (blue and red log), DPHI and NPHI (blue and red log), density (green log), and gas units (black log)..... 55

Figure 3-2. Crossplot shear wave splitting versus lithology from UMV shale to Cameo. Y axis plotted shear wave splitting values in percentage. X axis plotted  $V_{shale}$  values (from 0 to 1). Colors indicated gamma ray values from shaley sands (hot colors) to shales (cold colors). Upper graph shows a histogram for  $\gamma$  values higher than 3% (dots outside the shaded black box). .... 56

Figure 3-3. RWF 332-21 well logs from Cameo Coal to the Rollins Member. From left to right: normalized gamma ray (brown log), shear wave splitting (blue log),  $\epsilon$  estimated from  $\gamma$  (red log), fast and slow shear (blue and red log), DPHI and NPHI (blue and red log), density (green log), and gas units (black log)..... 57

Figure 3-4. Crossplot of shear wave splitting versus lithology from Cameo coal to the Rollins Formation. Y axis plotted shear wave splitting values in percentage. X axis plotted  $V_{shale}$  values (from 0 to 1). Colors indicated density values. Density values less than 2.4 gr/cc (blue dots) represented coals. Upper graph shows a histogram for  $\gamma$  values higher than 3% (dots outside the shaded black box)..... 58

Figure 3-5. RWF 332-21 image logs showing a fracture and unfractured coal. From Keighley (2006). .... 59

Figure 3-6. Fracture areas in RWF 332-21 from UMV to the Rollins Formation. From left to right: Vshale plot, fracture zones (indicated by blue lines), shear wave splitting percentage and azimuth frequency calculated by Halliburton. Yellow lines indicated areas of more than 5% of shear wave splitting and gamma ray less than 85 GAPI..... 60

Figure 3-7. RWF 331-20 well logs from KMV gas to the Rollins Formation. From left to right: shear wave splitting (blue log) and gas units (black log). High shear wave anisotropy and gas zones correlation is indicated in green color and areas of poor correlation is indicated in pink color. .... 61

Figure 3-8. Mean gas units versus shear wave splitting at RWF 332-21. There is a good correlation between areas of high shear wave splitting and an increase in the mean gas unit content..... 62

Figure 3-9. Combination of fractures (R=Resistivity or healed fractures, O=Open fractures and I=Induced fractures), gamma ray, gas seep, gas seep density, and mud-weight logs in the RWF 542-20 well. From Matesic (2007). .... 64

Figure 4-1. Measurements carried out for estimating anisotropy in a typical VSP geometry. The travel-time difference,  $dt$ , between geophones located at a distance  $dh$  along the wellbore defines the apparent slowness,  $q = dt/dh$ . Three-component traces recorded by each downhole geophone yield the direction of particle motion,  $U$ , or the polar polarization angle,  $\psi$ , and azimuth,  $\phi$ . Modified from Grechka and Mateeva (2007). .... 69

Figure 4-2. a) Plan view of the main wells with respect to the VSP (red star). b) The VSP dataset contains 19 geophones that cover the depth interval from 4,510 to 5,220 ft (yellow) and are shown on the background of seismic reflection data..... 73

Figure 4-3. a) Travel time of the first arrival for the shallow receiver (depth 4509 feet) and b) Regional faults at 1130 ms (two-way travel time) from Jansen, 2005. .... 74

Figure 4-4. The first arrival times of P-waves and particle motion can be estimated in the three component VSP data. From left to right is shown the vertical component (Z), the horizontal component X and the horizontal component Y. .... 74

Figure 4-5. a) Anisotropic coefficients estimated from the upper 11 geophones and b) anisotropic coefficients estimate from the lower 11 geophones. Red line shows isotropic curve. Black dots are the data points (one dot for every shot gather use in the estimation) with their standard deviation. Blue dots are the best VTI fit to this dataset. .... 76

Figure 4-6. Depth profile at the VSP interval showing a) P-wave vertical velocity versus a virtual check shot and b) $\eta$ and $\delta$ anisotropy parameters. ....	77
Figure 4-7. a) Depth profile using a window of 400 feet at the VSP interval and b) Gamma-ray log showing the lithology interpreted in the VSP interval.....	78
Figure 4-8. Azimuthal variations of the measured a) and fitted b) apparent slownesses (both are corrected for isotropy) as functions of the P-wave horizontal polarization components for the best-fit orthorhombic model in the depth range 4510 – 4910 ft. Model parameters and their standard deviations are: $\alpha = 0^\circ \pm 5^\circ$ , $V_{p0} = 14.527 \pm 0.048$ kft/s, $\delta^{(1)} = -0.01 \pm 0.06$ , $\delta^{(2)} = 0.12 \pm 0.05$ , $\eta^{(1)} = 0.07 \pm 0.03$ , $\eta^{(2)} = 0.04 \pm 0.02$ , and $\eta^{(3)} = -0.02 \pm 0.03$ . Color scale shows the difference between the measure data and the isotropic model. White circles indicate the slowness variations expected in the absence of azimuthal anisotropy.....	80
Figure 4-9. Azimuthal variations of the measured a) and fitted b) apparent slownesses (both are corrected for isotropy) as functions of the P-wave horizontal polarization components for the best-fit orthorhombic model in the depth range 4830 - 5230ft. Model parameters and their standard deviations are: $\alpha = 45^\circ \pm 5^\circ$ , $V_{p0} = 14.44 \pm 0.05$ kft/s, $\delta^{(1)} = 0.03 \pm 0.07$ , $\delta^{(2)} = -0.1 \pm 0.06$ , $\eta^{(1)} = 0.07 \pm 0.04$ , $\eta^{(2)} = 0.13 \pm 0.02$ , and $\eta^{(3)} = -0.14 \pm 0.06$ . Color scale shows the difference between the measure data and the isotropic model. White circles indicate the slowness variations in the absence of azimuthal anisotropy... ..	81
Figure 4-10. a) Anisotropy parameters $\delta$ and $\eta$ for a shaley sandstone core plug b) Shear wave splitting percentage at the overburden. Red trend indicates the shear wave splitting and the black line indicates an average shear wave splitting over 40 feet.....	82
Figure 4-11. 700 foot interval from well RWF 441-20 equivalent to the 2003 VSP interval. Notice the high amount of fractures in the below price coal layer (blue line). From Halliburton (2006).....	83
Figure 4-12. S11 and S22 percent impedance change around VSP location. Gamma ray log and well perforations are also displayed. From Rumon (2006).....	84
Figure 5-1. a) RCP's 2003 seismic acquisition design. Red squares represent P-wave sources (708 shots), and the blue crosses represent receiver locations (1500 geophones). b) Rulison 2003 survey fold map. Color scale represents the subsurface fold: 175 to 220 (purple), 110 to 175 (green and blue), 75 to 110 (red) and less than 20 (yellow). .....	88
Figure 5-2. a) Areal gathers before noise attenuation processing. b) Kirchoff Prestack Time Migration (KPSTM) image from one of the four bins (azimuth 45 to 90).....	92

Figure 5-3. Percent of anisotropy for a) UMV shale (reservoir's overburden) and b) Cameo Coal. The blue color indicates areas of small azimuthal anisotropy, and the white and red colors indicate areas of high azimuthal anisotropy.....	94
Figure 5-4. Percent of azimuthal anisotropy from UMV shale to Cameo coal including the production of the wells (legend at left bottom side are EUR quantities in BCF). .....	96
Figure 5-5. Fractogram from UMV to Cameo Coal for a) Modulus and b) RMS Error. .	97
Figure 5-6. a) Fractogram showing the average orientation of the fractures at Cameo coal level. b) Natural fracture orientation for the main wells at Rulison Field. Created from Matesic (2007). .....	98
Figure 5.7 Histogram showing the angles distribution before calibrated with the well logs orientation. ....	98
Figure 5-8. Percent anisotropy volume for different seismic sections a) Inline 33 with the location of the VSP (yellow rectangle) and b) Inline 95 with the location of one of the main well producers. Y axis are the two-way travel time and X axis is the inline or crossline number. Color scale indicated the amount of azimuthal anisotropy or eccentricity.....	100
Figure 5-9. Percent azimuthal anisotropy section at crossline 52. Seismic traces are overlapping the volume and the main horizons are indicated at the right side. Purple colors indicate values with less than 4% of azimuthal anisotropy and hot colors represent areas of high azimuthal anisotropy. The white lines indicate suggests compartments below the Cameo coal layer. West side is at the left of the section. ....	101
Figure 5-10. Xline 72 is displayed. a) Cross correlation time-shift for the $S_{22}$ volume between the 2003 and 2004 survey. Negative values (blue colors) indicate a pull up or velocity decrease from 2003 to 2004 survey. From Rumon (2006) b) Azimuthal anisotropy volume with blue values indicating low azimuthal anisotropy in the 2003 survey.....	102
Figure 5-11. Left-lateral shear model proposed for Rulison Field. The arrows in the sketch (at left) represent the mean of interpreted structural features. Present-day stress orientation shows the same orientation of the stress axes as the proposed model (extension of the Piceance basin). Abbreviations: Ind frac=drilling induced fractures, Res frac= natural resistive (healed) fractures, and Open frac = natural open fractures. From Matesic (2007). ....	105

Figure 5-12. a) Estimated Ultimate Recovery (EUR) vs. Net Pay. b) Net Pay thickness map from Williams Company..... 107

Figure 5-13. Similarity volumes for  $S_{11}$  (pure fast shear, in red) and  $S_{22}$  (pure slow shear, in blue) at the Cameo interval (depth slice of 7080). Color bar: “1” means that there are no trace-to-trace differences. “.5” means that there is a 50% change in the wavelet shape from one trace to the next. Linear feature (possible fault) is interpreted with the dashed line. Modified from LaBarre (2006). ..... 108

Figure 5-14. a) Schematic showing idealized wrench faults. The splays are referred to as palm tree structures. At the splays’ zone, the location of fracture areas and increased well productivity are expected. From Christie-Blick and Biddle (1985). b) Cross-section showing fault system and wrench faults at Rulison Field. RCP survey area is outlined by dotted lines. Vertical exaggeration is close to 20 times. From Jansen (2005)..... 110

Figure 5-15. Shear-wave splitting coefficients calculated between the UMV and Cameo horizons for the 2003 and 2004 surveys. From Rumon (2006). ..... 111

## LIST OF TABLES

Table 2-1. Rock properties of the eight core plugs from Mesaverde Group. The table indicates the sample, depositional environment, lithology, porosity, permeability and grain density. H=Horizontal. V=Vertical. Modified from Rojas (2005).....	20
Table 2-2. Shear-wave velocities and shear wave splitting at different core samples angles at room pressure conditions. ....	28
Table 2-3. Thomsen anisotropy parameters values at different reservoir confining pressures for samples R-5566, R-5702, R-5727, and R-6451. ....	43
Table 4-1. Anisotropy parameters for Rulison Field overburden (depth range 4690 to 4870 feet) in a sandstone to shaley sandstone interval. ....	75

## ACKNOWLEDGEMENTS

This research was sponsored by the Reservoir Characterization Project (RCP) at the Colorado School of Mines. I am grateful for their support and this learning experience. I thank Dr. Tom Davis for his support, guidance and encouragement at all times. A special thanks to all my committee members--Dr. Mike Batzle, Dr. Ilya Tsvankin and Dr. John Curtis--for their comments and teaching. A special thanks to Colorado School of Mines faculty that dedicate great effort to provide high-level academic courses.

This research is a combination of different works in several locations. My special thanks to all the groups that allowed me to completed this work with their mentorship and knowledge:

- Dr. Vladimir Grechka and Dr. Jorge Lopez from the Reservoir Geophysicist Group at Shell Exploration & Production (SIEP), who supervised me in my summer internship with Shell and provided one of the best and most enjoyable work experiences that I have ever had. Special thanks to all the research group members--Dr. Albena Mateeva, Carol Gentry, Patsy Jorgensen and Dr. Andrei Bakulin--for their time. I thank my fellow interns Maria Alejandra, Kurang and Rongrong for the good times.

- Dr. Michael Batzle and Dr. Ronny Hofmann from the Center of Rock Abuse, who guided me in the laboratory and taught me about rock physics and experimental work. Special thanks to all the members of the CRA for their valuable help.

- Gabriela Suarez and Rich Van Dok, who guided me in the WesternGeco processing center, teaching me the new Omega and azimuthal processing analysis.

Thanks to all the people that helped me with their knowledge or support. Special thanks to Dr. Bruce Mattocks and Dr. Bob Benson.

Thanks to my fellow students and their families at Colorado School of Mines. The time in the University was amazing and enjoyable thanks to “you all”: Mila, Ramses, Carlos, Gaby, Manuel, Elmar, Eldar, Jyoti, Steve, Gaby, Matthew, Liz, Marin, Xiaoxia, Rodrigo, Jia, Marta, Gilberto, Fernando, Manuel Paz, Wladimir, Jeff, Walter, Neil, Praj, Nelson, Kurt, Shannon, Laurie, Mike, Donny.

Finally to my beloved family, who call me and remind me of their love everyday. Gaby, Mom, and Dad I love you.

## CHAPTER 1

### INTRODUCTION

As the demand for energy increases and conventional resources decline, there is a growing need to develop unconventional resources. According to the estimates of the Energy Information Agency (EIA, 2004), 23% of the total natural gas reserves are in tight gas sandstones and 51% of the proven reserves in these types of reservoirs are located in the Rocky Mountains (McCallister, 2000). Unconventional gas plays represent large volume resources that are difficult to produce.

Despite the rich concentration of gas in place, only a small percentage has been produced. Hemborg (2000) provide a historical review about the various attempts to exploit the tight gas sandstones in Piceance Basin and the disappointing results obtained until recent years. A significant growth in production has occurred in the last few years. Average annual gas production per well during the 80's was 32 million cubic feet and the averaged climbed to 84 MMcf in 2006.

The main goal of the Reservoir Characterization Project (RCP) is to incorporate high-resolution multicomponent seismic data into dynamic reservoir characterization. RCP Phase X and XI are dedicated to improving reservoir characterization and production of tight gas sandstones. Phase X concluded that multicomponent seismic data detects changes in pressure, helps to detect fracture areas and improves the reservoir characterization.

Phase XI objectives include previous results and future research to generate, calibrate and refine a geomechanical model of the reservoir (Davis, 2005). Estimation and analysis of seismic anisotropy is fundamental to create and calibrate a geomechanical model. The use of borehole imaging, surface seismic, well logs and rock measures will

allow the calibration of elastic parameters and help to reveal the rock heterogeneity, detect fracture areas and improve seismic imaging.

Most sedimentary rocks are anisotropic. Their seismic anisotropy, or dependence of seismic velocities on the direction of wave propagation or angle, is an important physical attribute. Relating anisotropy to its physical causes such as lithology, fractures, and stresses enables the determination of valuable information for reservoir characterization. Measurements of anisotropy are an obvious prerequisite to improving seismic imaging and reservoir characterization.

I used different datasets and techniques to estimate seismic anisotropy in the reservoir and the results improve the understanding of tight gas sandstones at Rulison Field.

## **1.1 Research Objectives**

The purpose of this research is to estimate seismic anisotropy in tight gas sandstones and use the estimations to characterize the overburden and reservoir at Rulison Field. The study of seismic anisotropy will reveal lithology and fracture areas. There are two main objectives to this study:

- 1.- Estimate the anisotropy parameters in the reservoir and overburden using core sample measurements, well logs and VSP analysis.
- 2.- Infer the fracture networks in the reservoir using P-wave NMO ellipses.

## 1.2 Seismic Anisotropy

An elastic medium exhibits seismic anisotropy if seismic waves of a given type propagate with a different velocity dependent upon direction (Tsvankin, 2001; Thomsen, 2002). Anisotropy in sedimentary rocks is caused by the following factors:

- Intrinsic anisotropy due to preferred orientation of anisotropic mineral grains or aligned pores;
- thin bedding of isotropic layers on a scale small compared to the wavelength;
- vertical or dipping fractures or microcracks;
- nonhydrostatic stress.

How is anisotropy different from heterogeneity? Heterogeneity is the dependence of physical properties upon position (Thomsen, 2002). Heterogeneity within a core sample, channel or reservoir produces seismic anisotropy at different scales. Heterogeneity and seismic anisotropy are scale dependent properties. Whenever the seismic wavelengths are large compared to the scale of the ordered heterogeneities, they obey the laws of anisotropy (Thomsen, 2002).

## 1.3 Rulison Field Description

A review of the geology, reservoir properties and previous works in the field is presented in this section.

Rulison Field, located in the Piceance Basin, Garfield County, Colorado, produces gas from 1700 to 2400 feet of stacked discontinuous sandstones and coals (Cumella and Ostby, 2003) within the non-marine Late Cretaceous Williams Fork Formation. The

sandstone channels are highly discontinuous fluvial sandstones, 20 to 60 feet in thickness and are interbedded in layers of siltstones, shales and coals. Production challenges include low porosities (1-10%) and low permeabilities (1-60  $\mu\text{d}$ ).

Rulison field area includes a 10-acre well spacing pilot (Figure 1-1) in an area of 2.15  $\text{mi}^2$  (5.5  $\text{Km}^2$ ). Even with this well density, observed connectivity between individual channels rarely occurs. Conventional P-wave seismic data is not able to locate sandstones channels, fracture networks, “sweet spots” or to image the reservoir in detail.

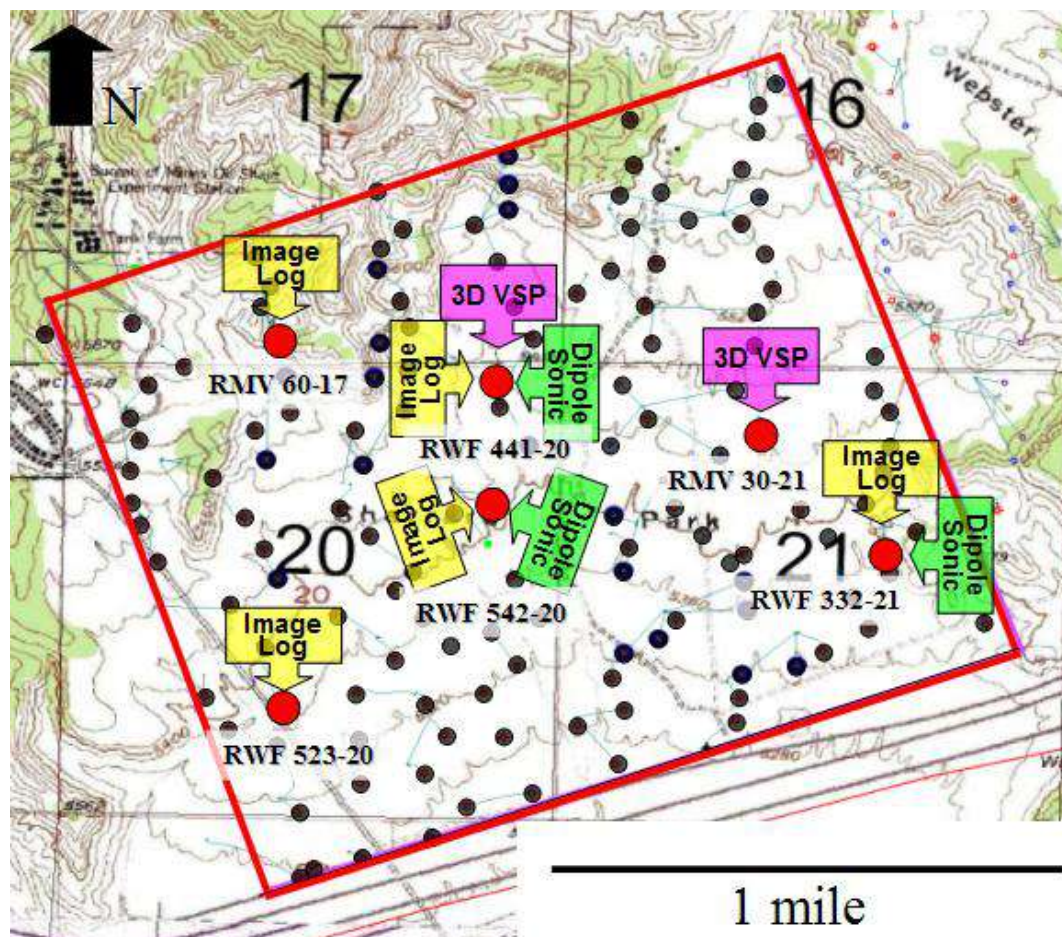


Figure 1-1. RCP study area (inside red rectangle). The main characterization wells are indicated with red dots. These include two 3D VSP, three cross-dipole sonic logs and five image logs. Black dots indicated other wells in the area (more than 80 wells).

Rulison Field is produced in a simple fashion. Currently, three to four wells are drilled out from one surface location, and are steered vertically throughout the reservoir. After drilling and logging, the largest sandstones intersecting the well are then completed with hydraulic fracturing. The well is then opened and the gas is allowed to flow under its own pressure to the surface.

RCP combines several datasets and uses them to improve the reservoir characterization. Some of the datasets are:

- Three high-resolution 4D multicomponent seismic data surveys (acquired in 2003, 2004 and 2006) with an area of 2.12 mi<sup>2</sup> (5.5 km<sup>2</sup>);
- Two high-resolution 3D wellbore imaging surveys (Vertical Seismic Profile);
- Three passive monitoring studies;
- Three crossdipole sonic logs, five image logs and conventional well logs and;
- Cores available from the U.S. DOE's. Multiwell Experiment (MWX)

#### **1.4 Geological Setting**

Piceance basin, a major Rocky mountain foreland basin, covers an area of 7,255 mi<sup>2</sup> (Figure 1-2). The basin trends northwest-southeast and is approximately 100 miles long and 50 miles wide (Spencer, 1989). Rulison Field is located in the southern portion of the Piceance Basin, close to Grand Valley, Parachute and Mamm Creek natural gas fields.

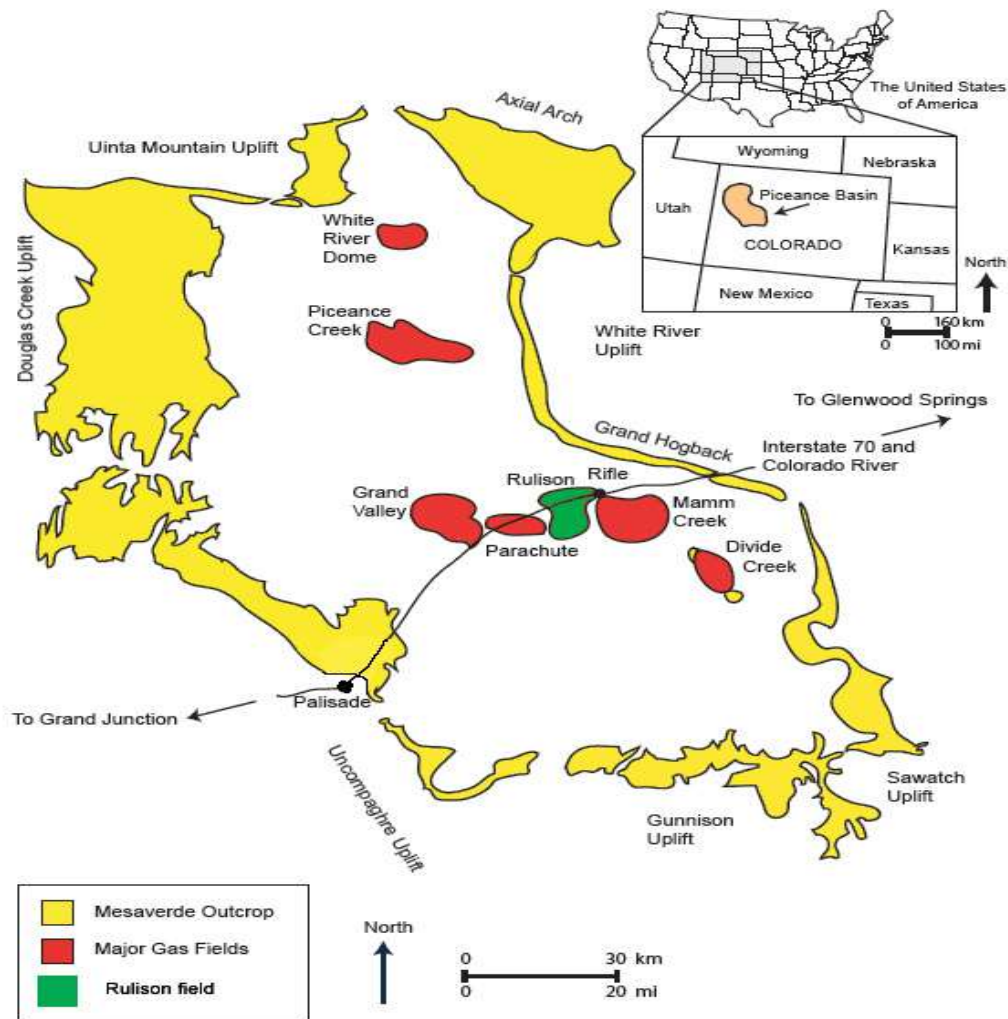


Figure 1-2. Rulison Field (shown in green) is located in the Piceance Basin, northwest Colorado. Major gas fields in the area (shown in red) produce from the Williams Fork Formation of the Mesaverde Group. From Hoak and Klawitter (1997) modified by Matesic (2007).

Gas production is primarily from the Late Cretaceous Williams Fork Formation involving 1700-2400 ft of stacked, highly discontinuous fluvial channels (Cumella and Ostby, 2003). The Williams Fork Formation is characterized principally as a meandering fluvial system, where most of the sand bodies were deposited as point bars and overbank

deposits during the lateral migration of rivers. The stacked sandstone bodies are highly lenticular, with typical lateral extent of 500-800 ft. Thicker, more laterally continuous sandstones, can reach a thickness of over 100 ft and are probably the result of amalgamation (Lorenz et al. 1985, Cole and Cumella, 2003). In addition, internal permeability barriers such as accretionary bedding and scour surfaces are present (Cumella and Ostby, 2003). A thin shale interval in the upper part of the William Fork Formation is a strong seismic reflector and is a possible seal that creates overpressure in the basin-centered gas accumulation.

During the Sevier Orogeny, the late Cretaceous Rocky Mountain foreland basin was flooded by marine waters to form the Western Interior Seaway. Sediments from the Sevier Orogeny were deposited as alluvial fans and graded progressively into braided-plain, coastal-plain, deltaic, shoreline, and offshore environments within the Mesaverde Group (Johnson, 1989).

Figure 1-3 shows the stratigraphic nomenclature used in this study. The Williams Fork is underlain by the Iles Formation and includes the Corcoran, Cozzette, and Rollins Sandstone members, which were deposited in inner-shelf, deltaic and lower coastal-plain settings (Cole and Cumella, 2003). The lower part of the Williams Fork is a coal-bearing interval known as Cameo-Wheeler that was deposited in a coastal-plain setting by meandering streams (Johnson, 1989).

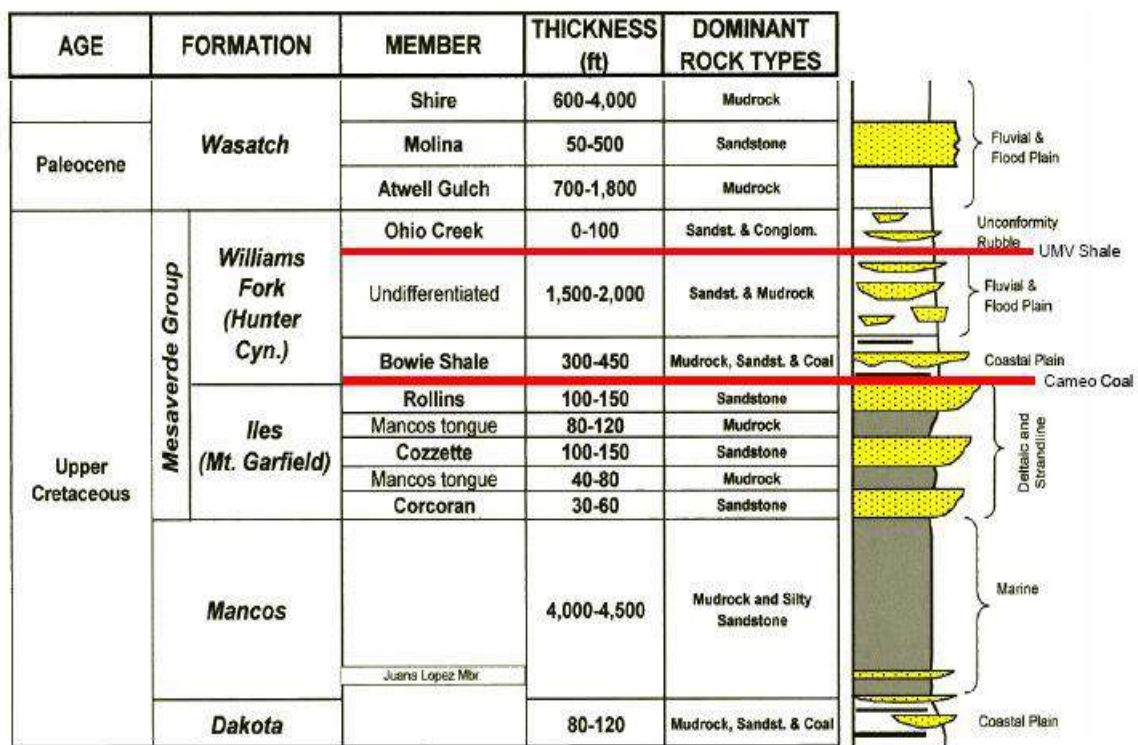


Figure 1-3. Stratigraphic column of the Rulison Field area. Tight gas sandstones are within the Late Cretaceous Mesaverde Group. From Cole and Cumella (2003).

The Williams Fork is overlain by the Ohio Creek Member of the Mesaverde Group and represents part of a shoreline progradational sequence. Laramide tectonics caused a regional unconformity, which separates the Cretaceous and Tertiary deposits.

The largest volume of gas was generated from the Cameo coal interval within the Mesaverde Group. Figure 1-4 shows the petroleum system in Piceance Basin. Timing of gas generation coincides with maximum burial of the reservoir interval during the Oligocene Epoch (33.7 to 23.8 Ma). The dominant trapping mechanism is stratigraphic, related to the stacking of fluvial sand bodies surrounded by floodplain mudstones.

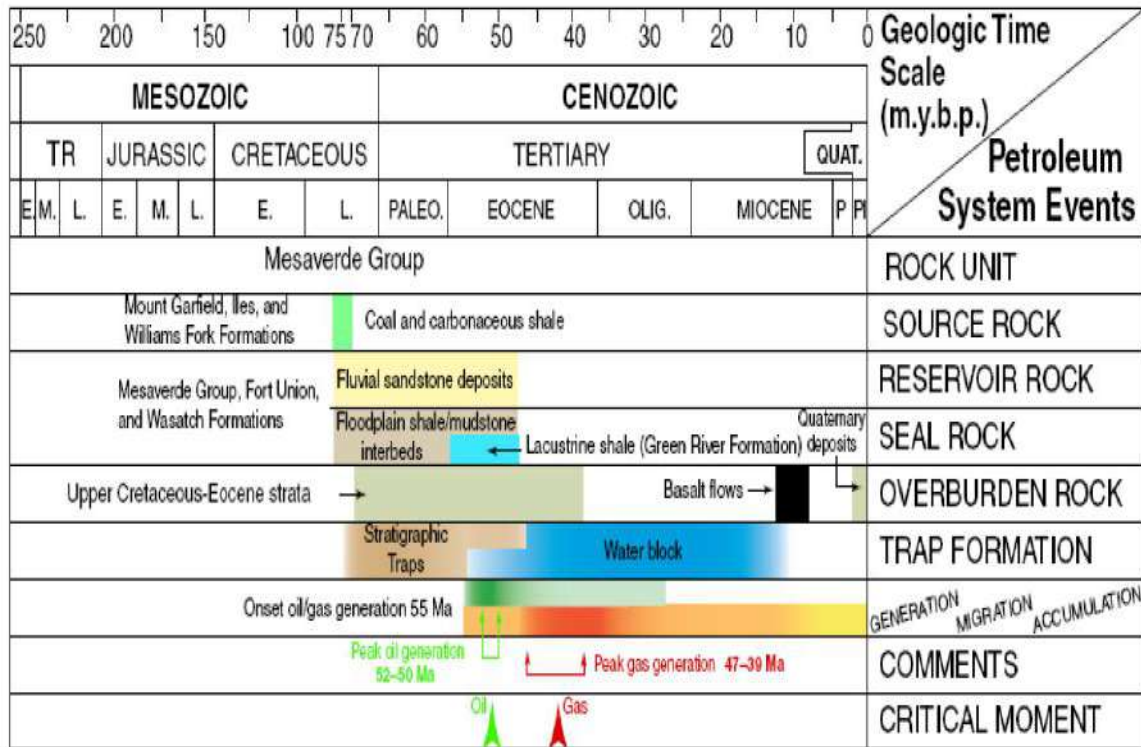


Figure 1-4. Petroleum system events chart showing timing of elements and processes related with to the hydrocarbon generation and accumulation in Piceance basin. From Magoon and Dow (1994) modified by Guliyev (2007).

The fault and natural fracture system has been documented to have a major role in migration of gas from the deeper part of the basin (Cumella 2006; Jansen 2005). Subtle fracture networks control gas migration and typically correspond to good well production. In this field, small thrusts, related to deeper basement structures, terminate up-section in the coals and fluvial sandstones of Mesaverde Group. Logically, at the tip-line terminations of the faults, fracture permeability is greatly enhanced and it is likely that the natural fractures are related to the splays (Cumella and Ostby, 2003).

Scheevel and Cumella (2005) show that overpressuring resulted in pervasive natural fracturing. Figure 1-5 sketches the gas migration through the fracture system from

the lower part of the Williams Fork Formation to the upper part. The continuous gas saturated interval is overlain by a transition zone containing gas and water bearing sandstones.

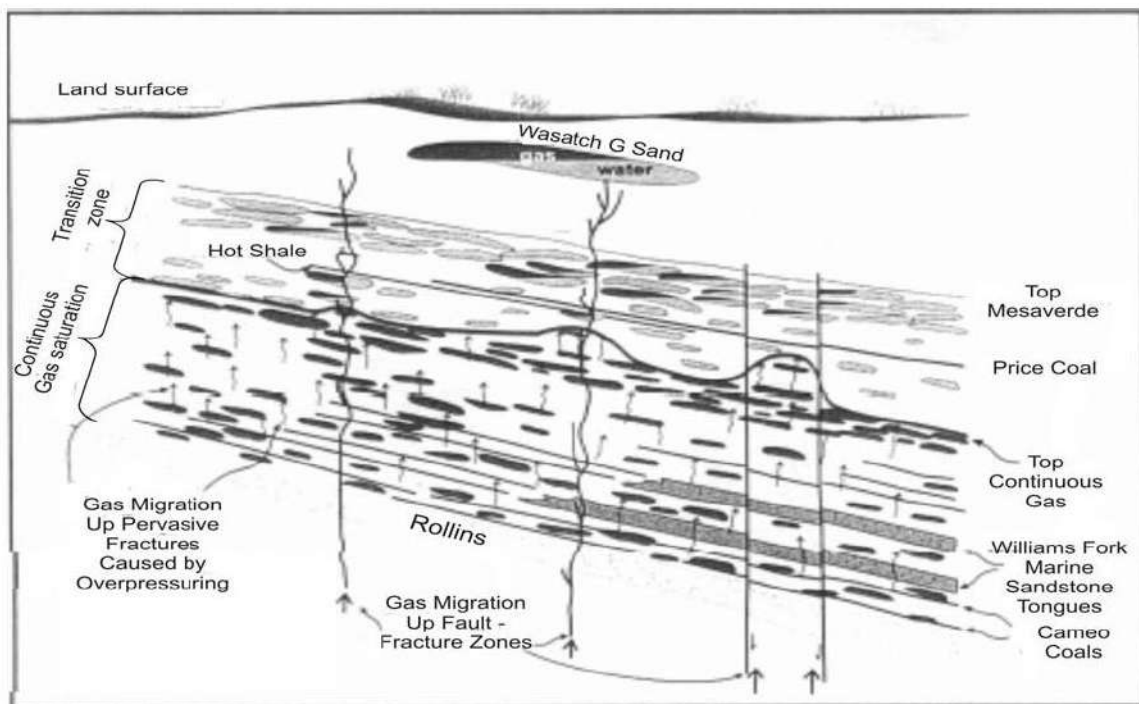


Figure 1-5. Schematic cross-section showing gas migration model for the Mesaverde Group. From Scheevel and Cumella (2005).

Figure 1-6 shows the tectonic history of the Piceance Basin. Kuuskraa et al. (1997b) suggested that a reactivated paleohorst and SW-NE directed regional shortening produced the dominant regional deformation and structures like the Rulison anticline. The basin has experienced an EW and WNW compression from Holocene to present.

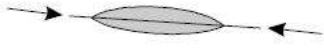
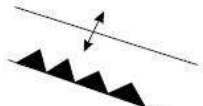
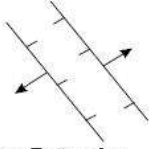
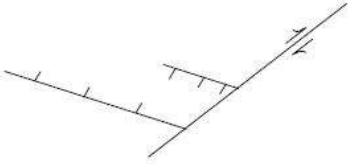
<b><i>Geologic Age</i></b>	<b><i>Structural Style</i></b>	<b><i>Schematic</i></b>
<b>Miocene to Recent</b>	<b>Regional Uplift</b>	 WNW Maximum Compression
<b>Cretaceous to Eocene</b>	<b>Laramide Thrust Faults and Related Folding</b>	 SW Directed Shortening
<b>Pennsylvanian/ Permian</b>	<b>Faulting and Graben Development</b>	 NW Trending Extension
<b>Precambrian</b>	<b>Regional Crustal Shearing and Extension</b>	 JAF00609.CDR

Figure 1-6. Schematic showing the tectonic history of Piceance basin. From Kuuskraa et al. (1997b).

Cumella and Ostby (2003) used 3D seismic data to interpret a series of faults in the Rulison area. They suggested that wrench tectonics is the dominant structural style of the northwest-trending features. They indicated left-lateral transpressional structural style. The first set of faults showed a northwest trend ( $N45^{\circ}W$ ), near-vertical dip, and left-lateral slip. The second set, showed a north-northwest trend ( $N20^{\circ}W$ ), dips of 30 to 60 degrees, and showed reverse character. A possible explanation for this system is an east-west Laramide compression that produces left-lateral slip along pre-existing northwest-trending faults.

Kuuskræa et al. (1997b) suggested that the vertical overburden stress appears to be similar in magnitude to the maximum horizontal compressive stress. Therefore, fracturing has occurred perpendicular to the least and intermediate stress orientation, creating fractures with a mix of N30°W, N60°E and N70-80°W trends. The development of the major fracture in the Rulison field is shown in Figure 1-7.

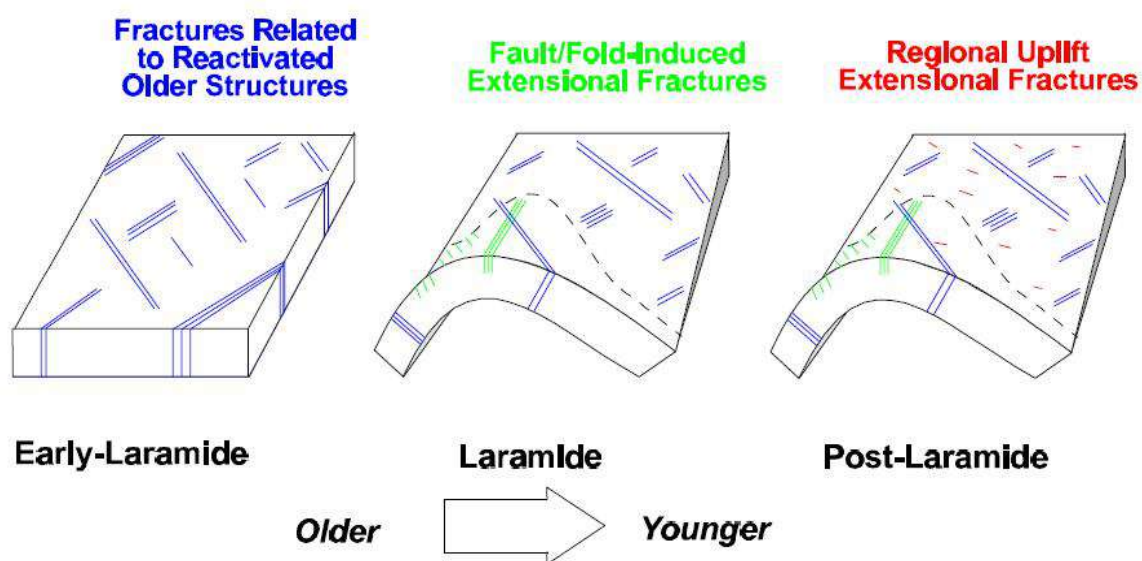


Figure 1-7. Development of major fractures at Rulison Field, Piceance Basin. From Kuuskræa et al. (1997b).

## 1.5 Reservoir Properties

Many of the reservoir properties were obtained from the research done during the U.S. DOE's Multiwell Experiment (MWX), a field laboratory designed to improve the characterization and production of tight gas sandstones. The MWX research is located less than 2 miles from the RCP survey area.

Tight gas sandstones are highly heterogeneous and complex. The reservoir is characterized by sandstone channels, interbedded with siltstones, shales and coals. The

discontinuous nature of the channels requires well spacing of 20 acres or less to adequately drain the reservoir (Cumella and Ostby, 2003).

Williams Fork Formation sandstones porosities range from 1 to 10%. Changes in porosity are less than 2% for a 1000 psi confining pressure change (Sattler, 1989). Permeabilities range from 1 to 60  $\mu$ D. Water saturations range from 30 to 35% in productive sands (Cumella and Ostby, 2003) and 65% at the top of the Mesaverde Group.

Log porosities range from 10 to 12%, but measured porosities in core are lower as mentioned earlier. The upper one-third of the Williams Fork Formation is considered to have low reserve potential, due to high water saturation.

The gas composition in Rulison Field is mainly methane. Reinecke et al. (1991) noted that gases above and below Cameo coal have a different composition. Coal gases are chemically drier (90 to 93% methane, 1 to 3% ethane, and 3 to 6% carbon dioxide) compared to sandstones gases, which are wetter (89 to 92% methane, 3 to 6% ethane, and 1 to 4% carbon dioxide).

The reservoir pore pressure gradients vary from 0.433 psi per foot (normal hydrostatic gradient) to 0.68 psi per foot. During primary depletion processes, reservoir pressure decreases; however, areas not connected to the depletion zone stay at higher pore pressures. The pore pressure data at the MWX site is shown in Figure 1-8.

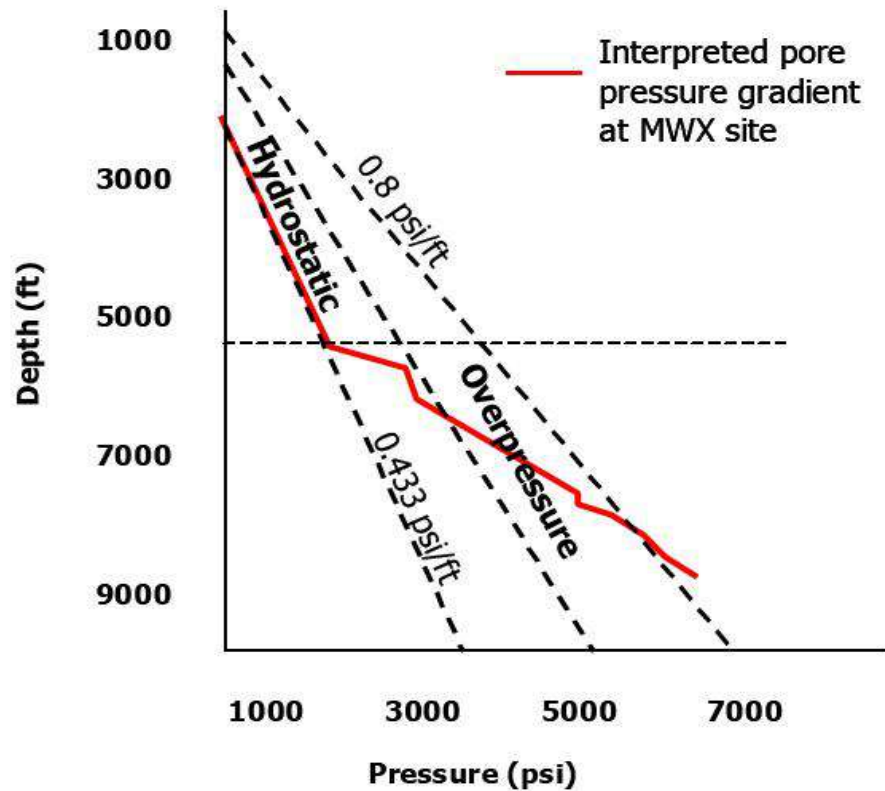


Figure 1-8. Pore pressure gradient measurements as function of depth at the MWX site. Pore pressure increases with depth to progressively higher gradients. Top of the reservoir show in dashed line. From Spencer (1989) modified by Rojas (2005).

## 1.6 Previous Work at Rulison Field

Previous researchers had conducted studies at Rulison Field to improve the reservoir characterization and production. The study areas include geological and engineering modeling, rock physics, geomechanics, time-lapses, and multicomponent analyses that improve the understanding of tight gas sandstones. A brief overview of the results from different researchers follows:

Jansen (2005) analyzed P and S wave seismic data to identify and delineate fault and fracture zones in the Rulison survey area. His study showed that the occurrence of natural fractures is linked to the faults and areas of deformation. He suggested that wrench faulting occurred in the field.

Burke (2005) analyzed two cross-dipole sonic logs. She found multiple fracture orientations in the sandstones layers and shear-wave splitting around 5%.

Higgins (2006) related stress, rock strength and pressure to create a one-dimensional geomechanical model. She found that most natural fractures and drilling fractures are aligned in the same direction as the direction of present day maximum horizontal stress (east-west with slight northwest-southeast trend). She showed that stress magnitudes were lithology dependent.

Matesic (2007) analyzed well logs to identify fractures and faults. He found that the current in-situ stress orientation ( $S_{hmax}$ ) is N70°W and suggested that natural open fractures are solely developed in sandstones. He found three sets of resistive fractures in the field (N30°W, N60°W and N70°W).

Vasconcelos & Grechka (2006) used multicomponent surface seismic to characterized multiple fracture sets assuming an orthorhombic model. The study showed a set of cracks oriented WNW-ESE in the western part of the study and multiple fracture sets in its eastern part.

Xu (2006) analyzed azimuthal AVO and NMO ellipses using P-wave surface seismic. She found that the AVO-gradient anomalies at the bottom of the reservoir coincide with intersections of wrenching fault systems. The study showed a poor correlation between the azimuthal AVO and NMO attributes.

Rojas (2005) studied the elastic rock properties of tight gas sandstones. The study showed that lithology and fluid effects have a significant influence on  $V_p/V_s$ . Tight gas

sandstones will have a  $V_p/V_s$  lower than 1.7 and shales will have a  $V_p/V_s$  higher than 1.7. Gas-saturated sandstones will produce a  $V_p/V_s$  of 1.6 or lower.

Guliyev (2007) used the results from Rojas (2005) to create a high resolution  $V_p/V_s$  volume of Rulison Field. The results showed a good correlation between the  $V_p/V_s$  volume and reservoir rock quality.

Mattocks (2004) analyzed the 2003 VSP and provided additional insight into the shear wave polarizations and delay times. He found a fast shear-wave orientation of N45°W.

Kusuma (2005) studied P-wave time-lapse seismic monitoring at Rulison Field within a 7 year interval (1996-2003). He found that the field had different P-wave time-lapse anomalies and that faults bounded those anomalies.

Keighley (2006) studied P-wave time-lapse seismic monitoring at Rulison Field. He suggested that P-wave time lapse can detected time shift measured at the reservoir in a limited extent. He found high changes in the Cameo coal interval that could be related with production and associated stress changes.

Rumon (2006) studied shear-wave time-lapse seismic monitoring at Rulison Field. He suggested that time-lapse shear-wave splitting changes correlated with depletion areas and that by-passed zones occur in the reservoir.

## **1.7 Research Approach**

This research provides valuable insight about seismic anisotropy at Rulison Field using different datasets and techniques. The thesis is divided into four main chapters, cores, well logs, borehole seismic and surface seismic.

Chapter Two includes the estimation of seismic anisotropy parameters using ultrasonic core plug measurements from the MWX-1 location. This chapter includes: (1) rock properties of the core plugs; (2) methodology; (3) estimation of seismic anisotropy parameters; and (4) relation between seismic anisotropy parameters and lithology.

Chapter Three includes the analysis of well logs in the RCP survey area. This chapter includes: (1) analysis of three cross-dipoles and shear wave splitting; (2) fracture analysis results from Matesic (2007); and (3) correlation of gas production with fractures.

Chapter Four includes the estimation of seismic anisotropy parameters and azimuthal anisotropy at the reservoir overburden using P-wave 3D VSP data. This chapter includes: (1) inversion methodology for VTI and orthorhombic media; (2) inversion results assuming VTI symmetry; (3) inversion results assuming orthorhombic symmetry; and (4) relation between seismic anisotropy parameters and their physical causes (lithology and fractures).

Chapter Five includes the estimation of azimuthal anisotropy using the 2003 P-wave prestack data at Rulison Field. This chapter includes: (1) azimuthal anisotropy methodology; (2) processing sequence; (3) discussion of results; and (4) correlation between azimuthal anisotropy and production areas.

## CHAPTER 2

### ESTIMATION OF SEISMIC ANISOTROPIC USING CORE PLUGS ULTRASONIC MEASUREMENTS

Ultrasonic velocity measurements were made on core plugs to determine the anisotropy parameters of tight gas sands. The measurements provided an estimation of anisotropy parameters ( $\epsilon$ ,  $\gamma$ ,  $\delta$ ,  $\sigma$  and  $\eta$ ) assuming vertical transverse isotropy (VTI) symmetry for different intervals within the Mesaverde Group in well MWX-1.

The core plugs were used to relate seismic anisotropic parameters with heterogeneities (such as clay content, laminations, and micro-fracture) present in the core plugs matrix and provide a qualitative linkage between heterogeneity and seismic anisotropy.

There are evident assumptions and shortcomings in the use of ultrasonic measurements to characterize the rocks in a tight gas reservoir. They include:

1. Frequency range: ultrasonic frequencies (500 Hz in this case) measurements may vary from seismic frequencies. The main reason for this is the dispersion: the variation of velocity with frequency. Fortunately, in high-velocity rocks, as in tight gas sands, dispersion is less of a factor, and it is possible that the estimation of anisotropy parameters is not affected.

2. Scaling: seismic anisotropy depends on scale, and the values measured in a core sample can be different from the values measured at the reservoir. Ultrasonic data are measured in wavelengths of millimeters, while seismic data are recorded in wavelengths of tens to hundreds of meters.

3. Heterogeneity and sampling: a few core samples could not represent all the heterogeneity of the subsurface. Also, it is difficult to select the appropriate core samples that represent all the features in the reservoir, mainly faults, fractures, stresses and channels.

## **2.1 Rock Properties of Core Plugs**

Eight core samples (four intervals, each with a vertical and horizontal sample) were selected for this study from the samples used by Rojas (2005) during her elastic rock properties studies. These samples are from the MWX-1, one of the U.S. Department of Energy's Multiwell Experiment wells, and include different lithologies and rock properties values. MWX-1 was selected by Rojas (2005) due to the data available. The well is the best producer among the experimental wells, with a EUR between 2-2.5 BCF.

Rojas (2005) found the  $V_p/V_s$  properties for the different core plugs. In this study seismic anisotropy parameters are found from additional measurements at the core samples, providing a valuable insight about lithology and heterogeneities at the Mesaverde Group.

All the core plugs are from the Mesaverde Group and correspond to fluvial and coastal depositional environments, which include sandstones, shaley sandstones and shales. The fluvial depositional environment consists of irregularly shaped, multistory, composite sandstones that were deposited by meandering-stream systems. The coastal depositional environment is characterized by distributary channel sandstones that were deposited in an upper delta-plain environment. Table 2-1 summarizes the properties calculated by Rojas (2005) for the core plugs selected for the anisotropy measures.

Table 2-1. Rock properties of the eight core plugs from Mesaverde Group. The table indicates the sample, depositional environment, lithology, porosity, permeability and grain density. H=Horizontal. V=Vertical. Modified from Rojas (2005)

Sample	Environment	Lithology	Porosity (%)	Permeability ( $\mu\text{D}$ )	Grain density (g/cc)
R-5566 V	Fluvial	Very fine grained sand with siltstone laminations intervals	2.6	2	2.66
R-5566 H	Fluvial		3.7	9	2.71
R-5702 V	Fluvial	Siltstone	1.7	1	2.69
R-5702 H	Fluvial		1.7	2	2.68
R-5727 V	Fluvial	Coarse grained sands, mainly massive	7.7	6	2.65
R-5727 H	Fluvial		7.6	12	2.65
R-6451 V	Coastal	Very fine grained sand with siltstone laminations	7.9	9	2.65
R-6451 H	Coastal		8.1	19	2.65

Lithology and grain density showed that the samples are mainly sandstones (quartz density 2.65 g/cc) with different clay content. The distribution of the components of the samples will generate different levels of heterogeneity. Porosity (1.7 to 8.1%  $\pm$  0.5%) and permeability (1 to 19  $\mu\text{D}$   $\pm$  1 $\mu\text{D}$ ) values are very low. Permeability values are higher for horizontal core plugs showing the permeability anisotropy of the reservoir. Permeability, in most of the cases, will be higher in the horizontal direction than the vertical direction due to deposition and compaction effects.

Figure 2-1 shows four core samples used in the experiment. Core plugs R-5566V and R-5566H consist of very fine grained sand with multiple siltstone laminations intervals. These core samples have different porosity and a different composition between the horizontal and vertical core plug. Core plugs R-5702H and R-5702V consist of

siltstone. Figure 2-2 shows the other four core samples used in the experiment. Core plugs R-5727V and R-5727H consist of coarse grained sand. Core plugs R-6451H and R-6451V consist of very fine grained sand with siltstone laminations deposited in a coastal environment.

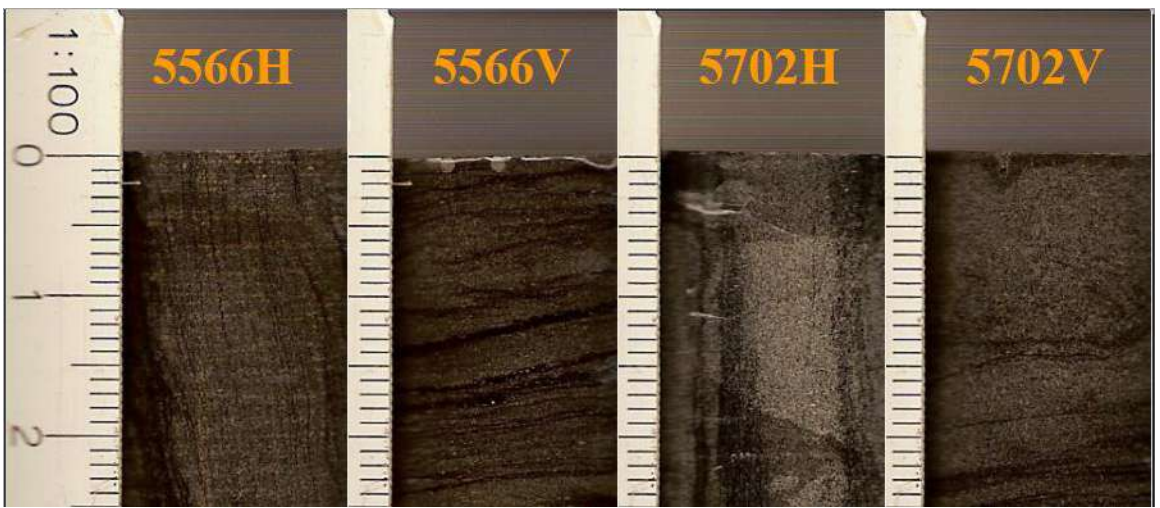


Figure 2-1. Horizontal and vertical core plugs. From left to right samples: R-5566H, R-5566V, R-5702H and R-5702V. Vertical scale is shown in centimeters.

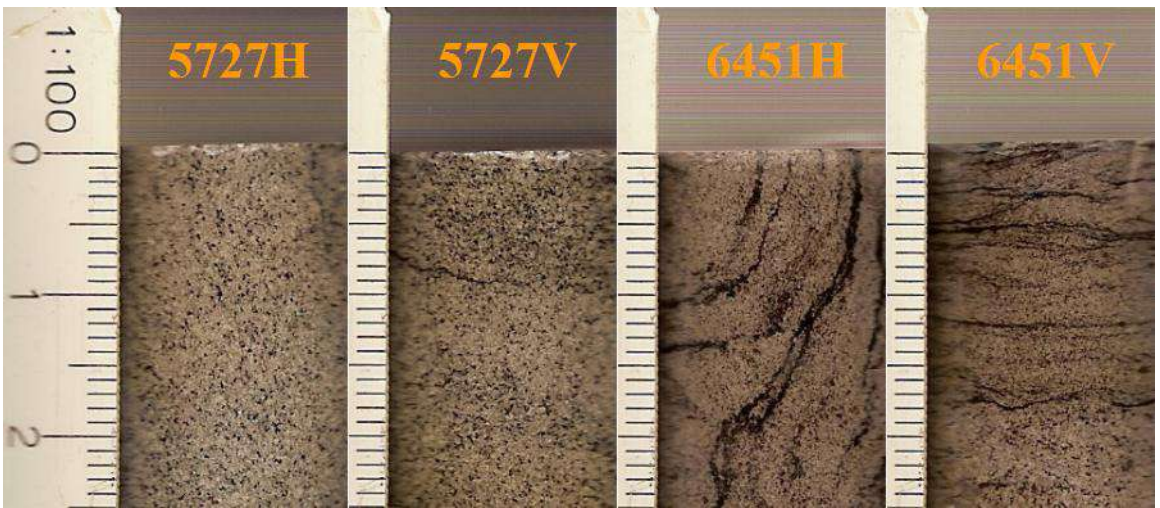


Figure 2-2. Horizontal and vertical core plugs. From left to right samples: R-5727H, R-5727V, R-6451H and R-6451V. Vertical scale is shown in centimeters.

### 2.1.1 Mineralogy and Cracks of Core Plugs

It is important to know the material and heterogeneity of the core samples. The mineralogical description of the samples was done by Rojas (2005), using X-ray diffraction methods. The three sandstones samples are compound by quartz (68% to 73%), plagioclase (10% to 12%) and phyllosilicates (13% to 15%). The siltstone sample has 18% of calcite and lower percentages of quartz (58%) and phyllosilicates (10%).

Figure 2-3 shows scanning electron microscope (SEM) images at different magnifications (50x, 100x, 500x, 1000x) from sample 6451. Dark areas in the SEM indicate pore space, while lighter gray colors indicate mineral surfaces. Natural fractures are identified due to the presence of cementation that fills the fractures.

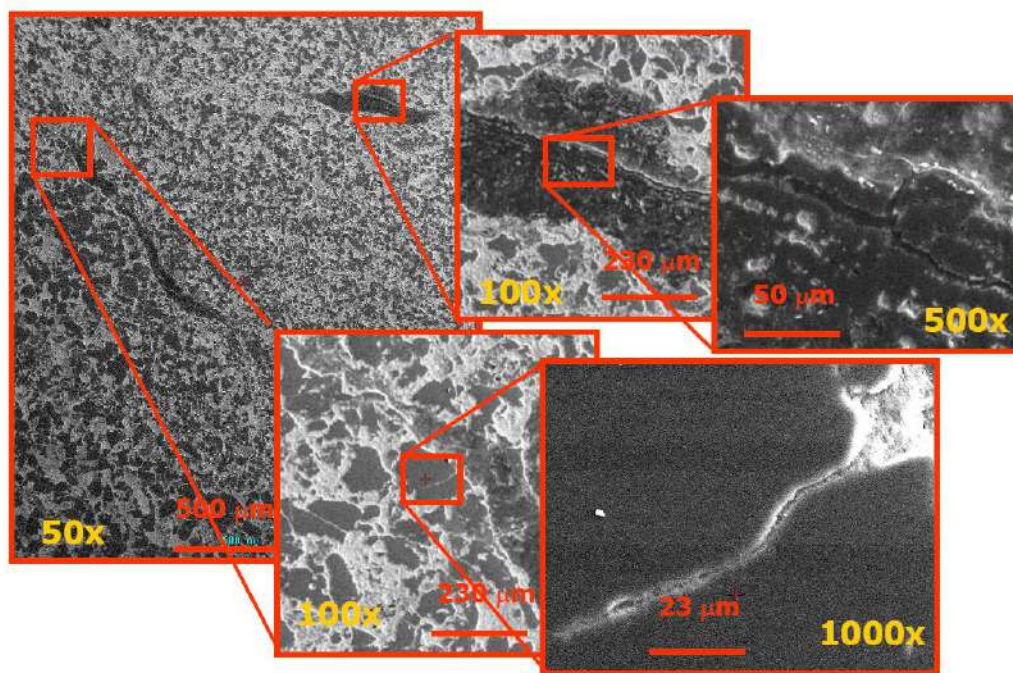


Figure 2-3. SEM pictures of interval 6451 at different magnifications (50x, 100x, 500x, 1000x). A natural fracture (1000x image) shows cementation. From Rojas (2005).

Computed axial tomography (CAT) scan analyses were made on each core plug to verify the heterogeneity of the sample. Figure 2-4 shows the imaging of core plug R-5566H for three different directions ( $0^\circ$ ,  $90^\circ$  and axial). There is an evident heterogeneity in the distribution of laminations in this sandstone with shaley laminations in multiple directions. The vertical sample R-5566V was highly laminated. A difference in the grain density between the horizontal and vertical core plugs suggest mineralogy heterogeneities.

Figure 2-5 shows the imaging of core plug R-5702H for three different directions ( $0^\circ$ ,  $90^\circ$  and axial). There is an evident heterogeneity in the distribution of laminations in this siltstone sample with a preference direction of  $90^\circ$ . This direction is equivalent to a vertical lamination distribution within the interval.

Figure 2-6 shows imaging of core plug R-5727H for three different directions ( $0^\circ$ ,  $90^\circ$  and axial). The sample is highly homogeneous due to massive coarse grain sandstone. There are no laminations or cracks within the sample.

Figure 2-7 shows the imaging of core plug R-6151H for three different directions ( $0^\circ$ ,  $90^\circ$  and axial). The sample is highly homogeneous, but some cracks can be seen in the direction of  $0^\circ$ . These small cracks are similar to those observed in the SEM picture from the same interval and correspond to cracks with a horizontal orientation.

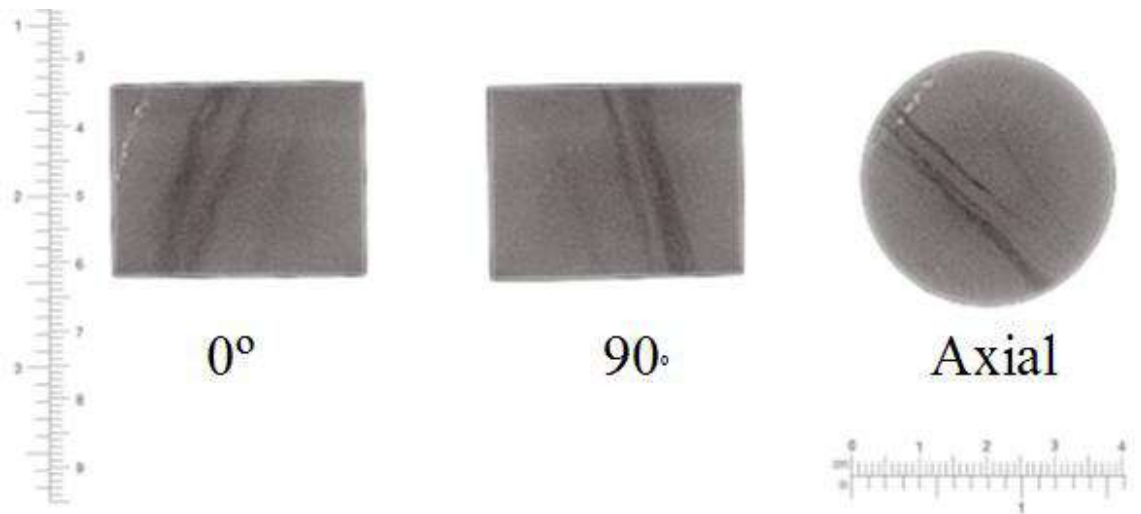


Figure 2-4. CAT scan of core plug R-5566H. Laminations occur in multiple directions and produce a highly heterogeneous sample.

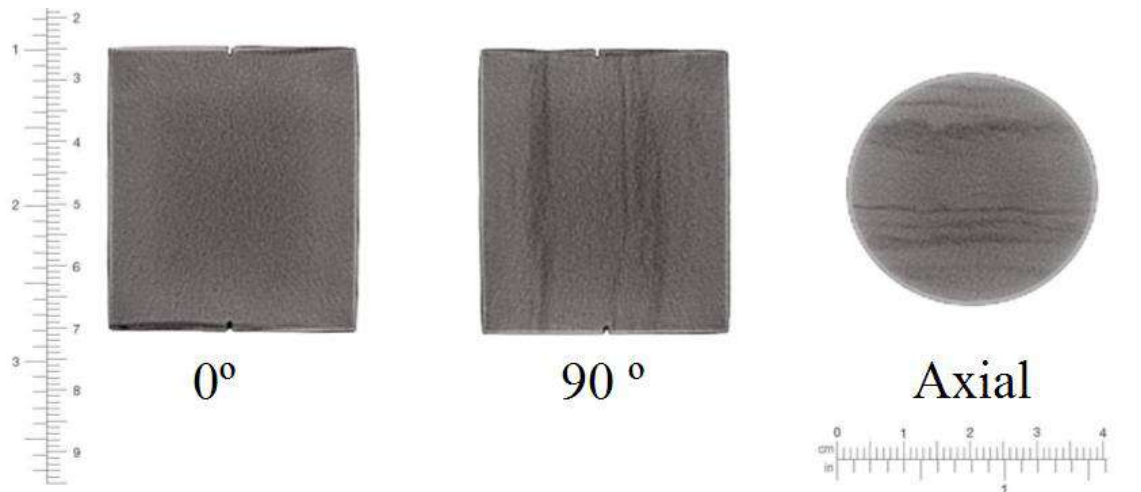


Figure 2-5. CAT scan of core plug R-5702H. Laminations occur in a preference direction (90°).

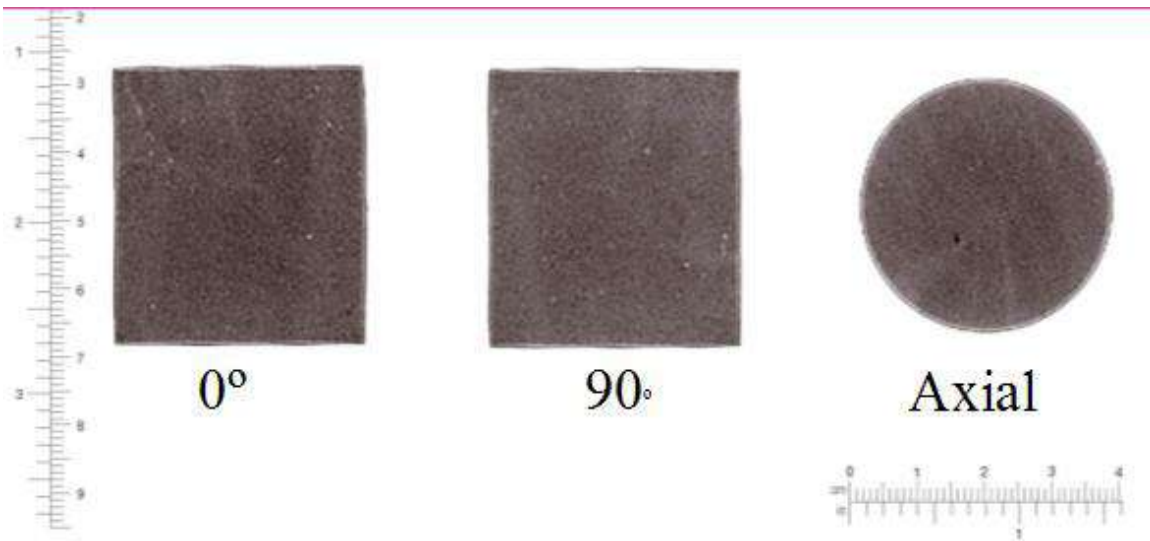


Figure 2-6. CAT scan of core plug R-5727H. Sample is close to homogeneous without cracks or laminations.

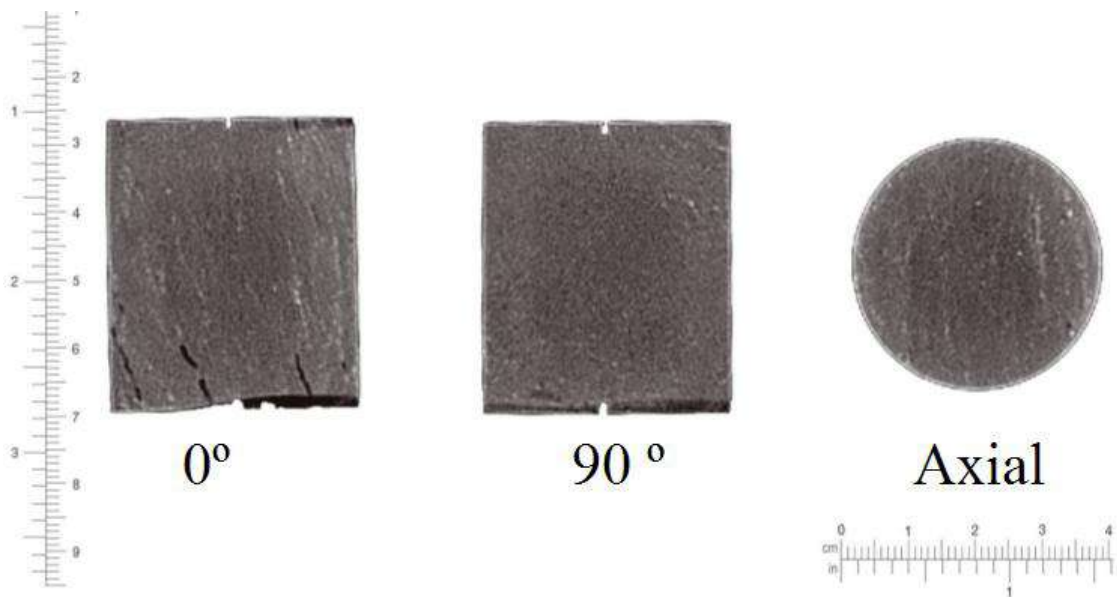


Figure 2-7. CAT scan of core plug R-6451H. Cracks occur in the direction of 0°.

### 2.1.2 Fluid Composition at Rulison Field

The composition of Rulison's fluid is a light gas, mainly a mixture of methane, ethane, nitrogen and CO<sub>2</sub>. Rojas (2005) calculated acoustic properties using different fluids and the results are shown in the Figure 2-8. The acoustic velocities are similar for dry, methane, and Rulison gas (composed of 85% methane, 10% nitrogen, and 5% ethane) fill samples.

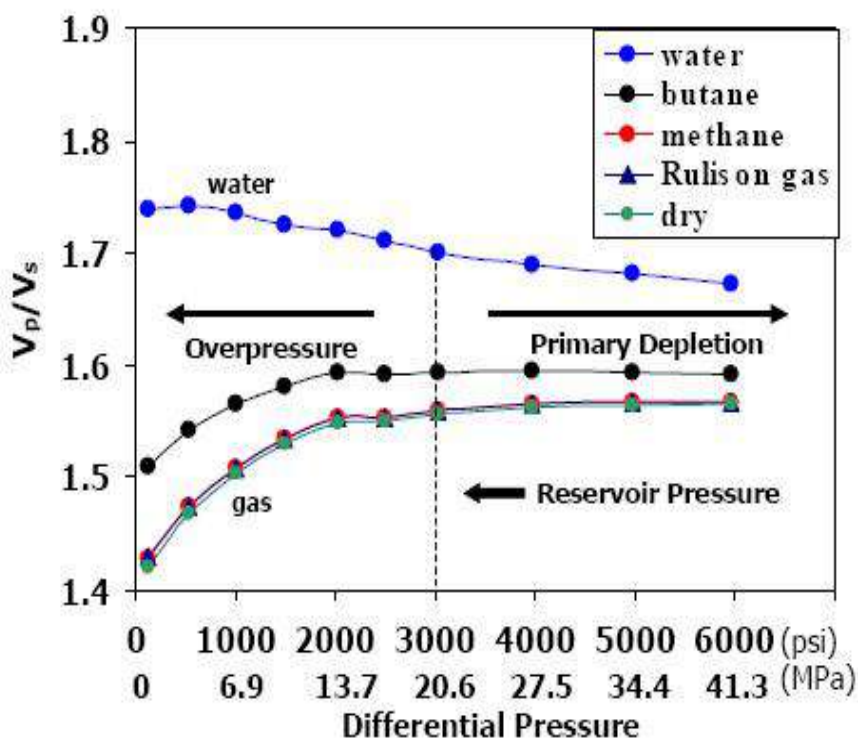


Figure 2-8.  $V_p/V_s$  versus differential pressure for a saturated sample. Fluid substitution using Gassmann's equation was done for 100% water saturation (salinity 25000 ppm), butane, methane and a mixture of gases (85% methane, 10% nitrogen, and 5% ethane), which represents Rulison Field gas. From Rojas (2005).

## 2.2 Seismic Anisotropy Orientation

Compressional and shear waves were propagated through each sample to identify fast and slow directions of shear wave propagation in the core plugs and were used to determine the orientation of the transducers for the pressure measurements. One transducer and one receiver were used in the experiment. The samples were recorded every 10 degrees while rotating the sample.

The S-wave transducers need to be aligned, one to the fastest and the other to the slowest direction of shear wave propagation in each core sample. In most of the cases, fast shear wave velocity is measured when one of the S-wave transducers is aligned parallel to the shaley layers or cracks present in the plugs, and the slow shear velocity is orthogonal to the fast shear wave velocity.

Figure 2-9 shows a schematic of the azimuthal dependence of shear wave propagation in a core sample. As the sample is rotated the shear wave propagation changes at each angle, one of the angles corresponds to the direction of the fast shear and the slow shear is orthogonal to the fast shear.

Once the fast and slow shear-waves directions are known, the shear wave splitting for an anisotropic rock with VTI symmetry can be calculated (Thomsen, 1986) using Equation 2-1:

$$\gamma \cong \frac{V_{s1}^2 - V_{s2}^2}{2V_{s2}^2}, \quad (2-1)$$

where  $\gamma$  is the shear-wave splitting parameter for the SH wave,  $V_{s1}$  is the fast shear-wave velocity, and  $V_{s2}$  is the slow shear-wave velocity. Table 2-2 shows the S-wave velocities with angle and the shear wave splitting percentage ( $\gamma$ ) for every sample at room conditions.

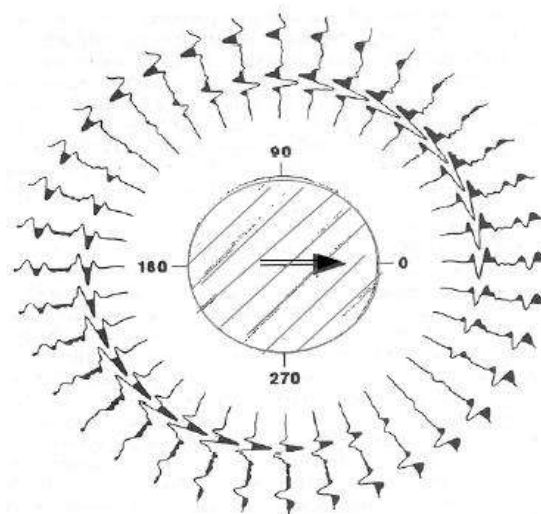


Figure 2-9. Schematic showing azimuthal dependence of shear wave propagation in a core sample. Modified from Sondergeld and Rai (1986).

Table 2-2. Shear-wave velocities and shear wave splitting at different core samples angles at room pressure conditions.

Angle	Vs 5566H (ft/s)	Vs 5702H (ft/s)	Vs 5727H (ft/s)	Vs 6451H (ft/s)
0 (Fast S)	8439	9738	7864	7534
10	8439	9738	7773	7534
30	8439	9738	7684	7534
50	8028	9738	7597	7534
70	7864	9264	7684	6939
90 (Slow S)	7811	9153	7512	6739
110	7811	9264	7512	7150
130	8258	9378	7773	7224
150	8378	9615	7773	7299
170	8378	9738	7773	7454
180 (Fast S)	8439	9738	7864	7533
$\Gamma$ (%)	8.4	6.6	4.8	12.5

Figure 2-10 shows the shear-wave velocities of different horizontal core samples at room pressure conditions and with angle rotation (see Figure 2-9). Fast shear-wave velocity is plotted in the 0 degrees angle and slow shear-wave velocity is plotted in the 90 degrees angle. The sample with the smaller anisotropy is the coarse sand. The samples with the highest anisotropy are the siltstone and sandstones with siltstone laminations. The uncertainty in the velocity estimation and angle is  $\pm 2\%$  and  $\pm 1^\circ$  respectively.

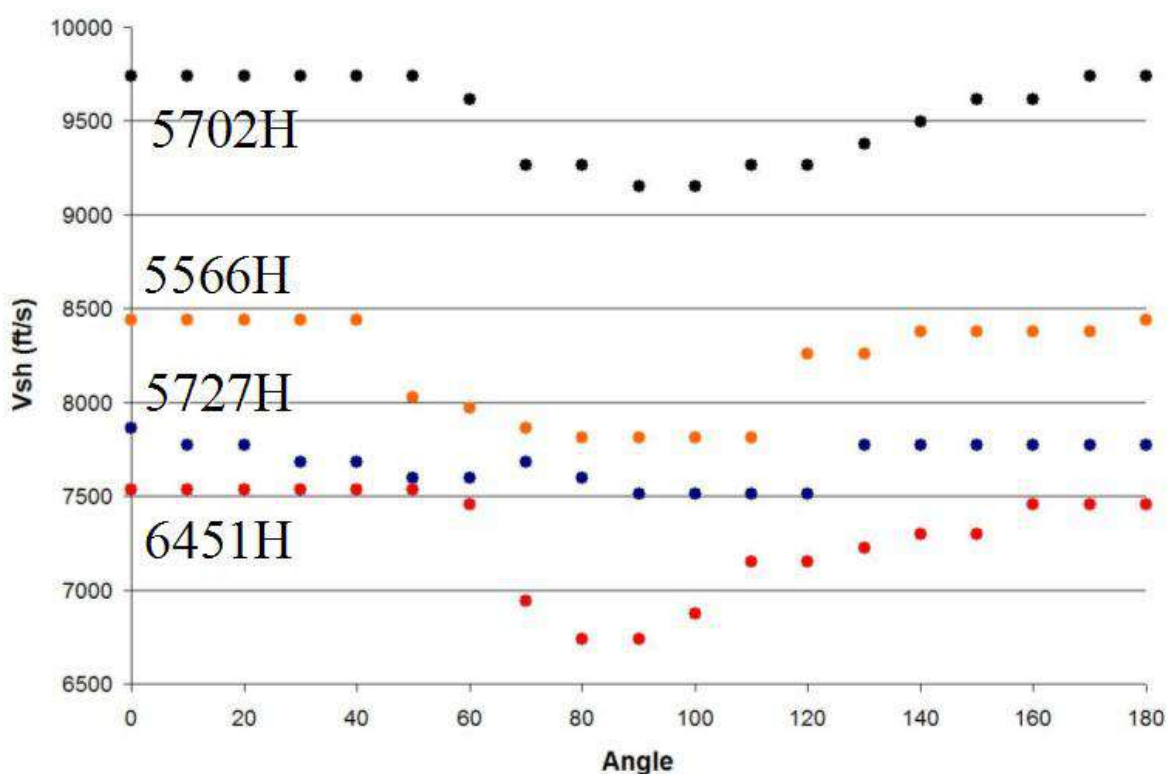


Figure 2-10. Shear wave velocities at different core sample angles at room pressure conditions.

The minimum  $\gamma$  of 4.8% for the coarse grained sandstone suggests that the sample is the most isotropic for shear wave propagation. The other three samples with  $\gamma$  from 6.6% to 12.5% suggest that shear wave splitting is detectable at room conditions for

sandstones, shaley sandstone and siltstone core samples. At room pressure conditions the anisotropy will be at the maximum due to the microfractures or cracks at the samples will remain open. The amount of shear wave splitting at reservoir pressure was verified with laboratory measurements.

## **2.3 Ultrasonic Seismic Anisotropy Measurements at Varying Confining Pressure**

The experiment setup, instrumental error and analysis of results are shown in this section.

### **2.3.1 Experimental Setup**

The P and S wave velocities of dry samples were measured as a function of hydrostatic confining pressure using an ultrasonic pulse transmission technique. One of the ultrasonic systems from the Center for Rock Abuse at the Colorado School of Mines was used during the experiments at different pressures. The experimental setup consisted of a pulse generator, a digital oscilloscope, and a pressure vessel. Piezo-ceramic transducers were used to generate P and S waves at a frequency of 500 Hz. Hydrostatic confining pressure was ranged between 500 to 6000 psi (3.4 to 41 Mpa) with increment intervals of 500 psi.

The sample preparation included measurement of the length, diameter, and weight. The transducers used were tested to verify that they worked properly. The core plugs were jacketed with rubber tubing and clamped with metal wire (Figure 2-11) to isolate them from the confining pressure. The transducers' wires and pore fluid lines are

connected to the ultrasonic testing equipment, and the sample is enclosed in a metal confining pressure vessel.

A pulse generator is used to send a signal to the piezo-ceramic transducers and to trigger the digital oscilloscope used for recording the output signal. A transducer (transmitter) transforms the electrical signal into mechanical vibrations. The pulses (P and S waves) travel through the rock sample and are received by a transducer (receiver) that transforms the mechanical vibrations into electrical signals. The signal received by the digital oscilloscope is recorded on a computer, and first arrival interpretation is done for velocity calculations. The receive time needs to be adjusted for the delay time introduced by the transducers. Further details can be found in Rojas (2005).

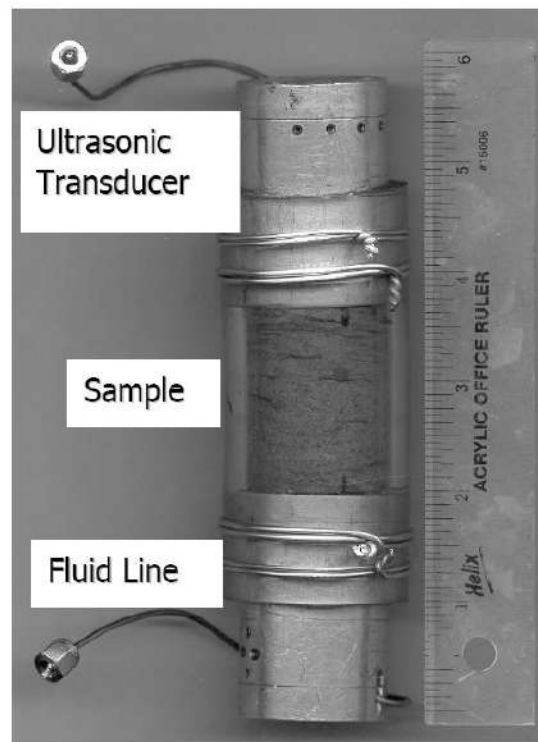


Figure 2-11. Sample setup for ultrasonic core plug measurements. From Rojas (2005).

Figure 2-12 shows a schematic with different P and S-waves measured in the experiment. In the vertical sample were measured  $V_{p0}$  and  $V_{p45}$  waves using two pair of transducers: one parallel to the core plug and one at 45°. In the horizontal sample were measured  $V_{p90}$ ,  $V_{SH0}$  and  $V_{SH90}$  using one pair of transducers. One quality control step is to verify that  $V_{s1}$  and  $V_{s2}$  in the vertical sample were the same. This similarity verified the Vertical Transverse Isotropy symmetry assumption used in the experiment. Also S-wave velocity from the vertical sample should be the same or similar to the perpendicular S-wave or  $V_{SH90}$  from the horizontal sample.

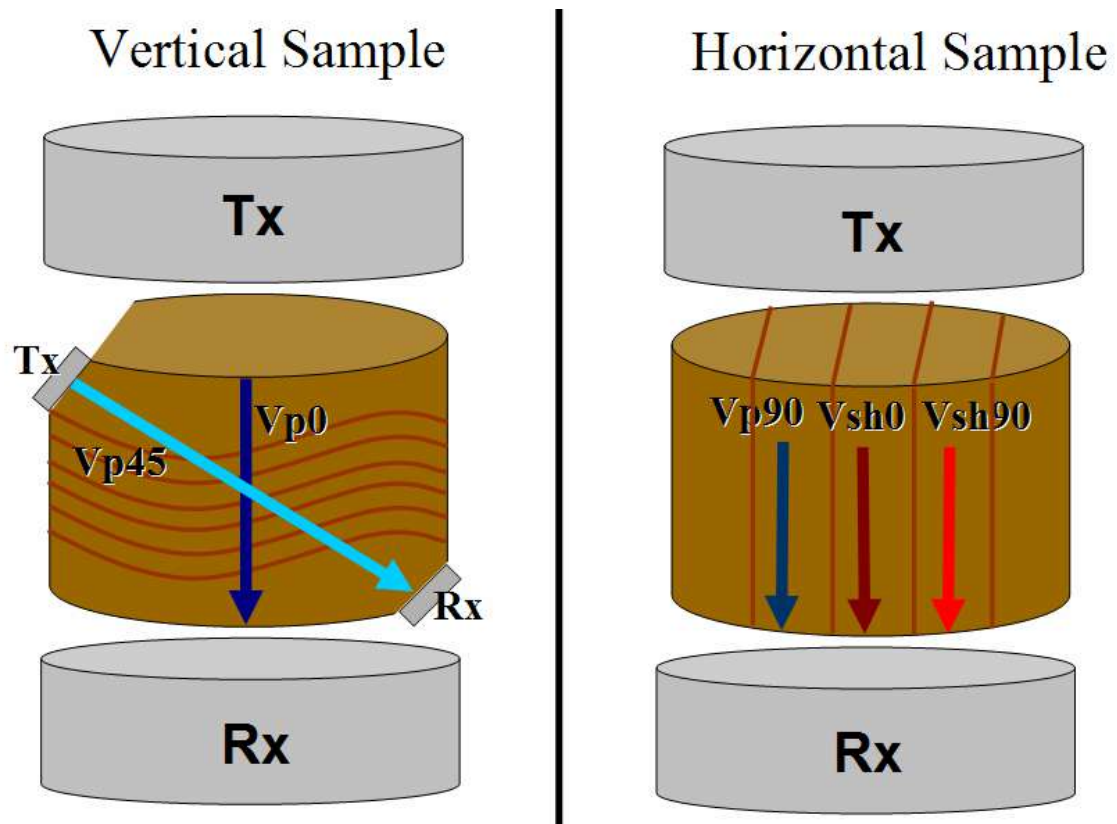


Figure 2-12. Schematic showing the P and S-waves measured in the vertical and horizontal samples. At the left is the vertical sample: two pairs of transducers are used to measure the  $V_{p0}$  and  $V_{p45}$  waves. At right is the horizontal sample: a pair of transducers is used to measure  $V_{p90}$ ,  $V_{SH0}$  and  $V_{SH90}$  waves.

### 2.3.2 Elastic Coefficient and Thomsen Parameters Estimation

The five independent elastic coefficients ( $C_{ij}$ ) for a VTI medium were calculated using the equations 2-2 to 2-6 (Wang, 2002a):

$$C_{11} = \rho V_{p90}^2 \quad (2-2)$$

$$C_{33} = \rho V_{p0}^2 \quad (2-3)$$

$$C_{44} = \rho V_{s1,90}^2 \quad (2-4)$$

$$C_{66} = \rho V_{s2,90}^2 \quad (2-5)$$

$$C_{13} = \left[ \frac{(4\rho V_{p45}^2 - C_{11} - C_{33} - 2C_{44})^2 - (C_{11} - C_{33})^2}{4} \right]^{\frac{1}{2}} - C_{44} \quad (2-6)$$

where  $\rho$  is the bulk density;  $V_{p0}$ ,  $V_{p45}$ , and  $V_{p90}$  are the compressional velocities propagating parallel, 45° and perpendicular to the anisotropy symmetry axis, respectively. The terms  $V_{s1,90}$  and  $V_{s2,90}$  are the shear wave velocities polarized parallel and perpendicular to the anisotropy symmetry axis, respectively, but propagating 90° to the symmetry axis. In this experiment the anisotropy symmetry axis is perpendicular to the bedding, so the compressional velocities are parallel to the bedding plane of the core plug.

The  $\epsilon$  and  $\gamma$  anisotropy parameters for a Vertical Transverse Isotropy (VTI) media were calculated using the equations 2-7 and 2-8 derived from Thomsen (1986):

$$\varepsilon = \frac{C_{11} - C_{33}}{2C_{33}} \quad (2-7)$$

$$\gamma = \frac{C_{66} - C_{44}}{2C_{44}} \quad (2-8)$$

where the elastic constant were calculated from the previous equations.

The  $\delta$  anisotropy parameters for a VTI medium were calculated using the equation 2-10 from Tsvankin (2001):

$$Vp(\theta) = Vp_0(1 + \delta \sin^2 \theta \cos^2 \theta + \varepsilon \sin^4 \theta) \quad (2-9)$$

$$\delta = \frac{\left( \frac{Vp(\theta)}{Vp_0} - 1 - \varepsilon \sin^4 \theta \right)}{\sin^2 \theta \cos^2 \theta} \quad (2-10)$$

where  $Vp(\theta)$  is the P-wave velocity for the measured angle, and  $V_{p0}$  is the P-wave vertical velocity.

The  $\sigma$  and  $\eta$  anisotropy parameters for a Vertical Transverse Isotropy (VTI) media were calculated using the equation 2-11 and 2-12 (from Alkhalifah and Tsvankin, 1995):

$$\sigma = \frac{C_{33}}{C_{44}}(\varepsilon - \delta) \quad (2-11)$$

$$\eta = \frac{\varepsilon - \delta}{1 + 2\delta} \quad (2-12)$$

where the elastic constants were derived from the measured velocities and bulk density, and  $\varepsilon$  and  $\delta$  were estimated from equations 2-7 and 2-8.

### 2.3.3 Measurement Uncertainties

The velocities are calculated from the travel time of the pulse through the sample. First arrivals are interpreted, and the arrival times are corrected by the calibration of the transducer pairs. Velocity is calculated from the travel time and sample's length using equation 2-13:

$$V = \frac{L}{T_T - T_D} \quad (2-13)$$

where, V is P or S wave velocity,

L is the length of the core plug,

$T_t$  is the measured travel time and

$T_d$  is the delay travel time in the transducers

In this experiment, the velocity error calculation is equal to equation 2-14:

$$\Delta V = \frac{\partial V}{\partial L} \Delta L + \frac{\partial V}{\partial T_T} \Delta T_T + \frac{\partial V}{\partial T_D} \Delta T_D \quad (2-14)$$

where  $\Delta V$  is the relative velocity error,

$\Delta L$  is the relative error in the length of the sample,  $\Delta L = \pm 0.01$  mm,

$\Delta T_T$  is the relative error in the oscilloscope,  $\Delta T_T = \pm 0.1$   $\mu$ s and

$\Delta T_D$  is the relative error in the oscilloscope,  $\Delta T_T = \pm 0.1$   $\mu$ s

Errors in picking are minimized with the use of an automated picking routine. First, the waveform amplitude between the baseline (zero voltage) and the first peak is measured. First-arrival times are then picked at the 3% point between the baseline and the first peak value. The uncertainties or errors in the P, SH and SV waves were estimated to be within  $\pm 2\%$ . These uncertainties are higher at low confining pressure and decrease as confining pressure is increased.

The uncertainties in calculated elastic constants increase due to the square of velocities and the inclusion of bulk density. As a result, the estimated uncertainties are  $\pm 4\%$ . Among the elastic constants,  $C_{13}$  has the higher uncertainty because it is calculated from three other elastic constants and the P-wave velocity at  $45^\circ$ . The uncertainty produced by angles different from  $45^\circ$  is reduced using the equation 2-10 that was calculated for different propagation angles.

The uncertainties of Thomsen anisotropy parameters are higher than the elastic constants, because the anisotropy parameters are related to the ratio of the elastic constants, and the random errors are amplified by a factor of two. Wang 2002b estimated that the uncertainties in the Thomsen anisotropy parameters are close to  $\pm 10\%$  for  $\epsilon$  and  $\gamma$  and  $\pm 25\%$  for  $\delta$ ,  $\sigma$ , and  $\eta$  (the last three parameters estimated from  $C_{13}$ ).

#### **2.3.4 Dry Core Plug Ultrasonic Measurements Results**

The eight core plugs were measured at different confining pressures (500 to 6000 psi), so changes in velocities can be observed. The confining pressure is incremented for each measurement and later decremented to the starting pressure (upgoing and downgoing pressure curves) to observe the stress hysteresis and anisotropy changes. The closing and opening of the cracks gave the rock a different modulus producing differences in the elastic behavior.

At each confining pressure, it is important to let the pressure stabilize at least for 5 minutes, in order to reduce errors induced by changes in the pressure vessel. At each confining pressure, a P-wave and two S-waves measurements were made.

The first arrival was calculated to estimate the compressional and shear waves velocities at different angles (0, 45 and 90 degrees). Measurements were made on dry tight sandstones. The behavior of gas (mainly methane saturated) is very close to the air-filled rock. Examples of the recorded signals for the sample 5566H are shown in the Figure 2-13. The good quality of first breaks is due to the high mechanical strength of the tight gas sandstones samples.

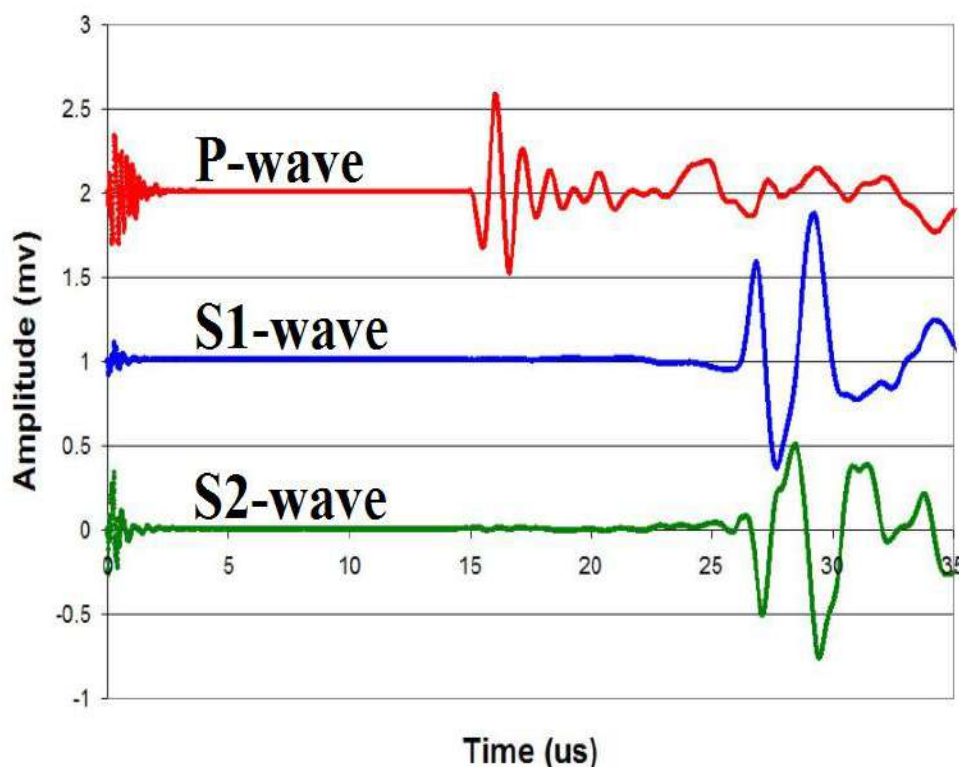


Figure 2-13. Compressional and shear waveforms for the sample 5566H.

Dry rock measurements are simpler than saturated rock measurements. The gas composition of the Rulison Field is methane-saturated tight gas sandstone and the results using dry rock samples are expected to be close to reservoir conditions. Differential pressure is the difference between confining pressure and pore pressure (equation 2-15). In this experiment the pore pressure is zero (atmospheric pressure), so the confining pressure is equal to the differential pressure (equation 2-16).

$$P_d = P_c - P_p \quad (2-15)$$

$$P_d = P_c \quad (2-16)$$

### 2.3.5 Discussion of Results

Compressional and shear wave velocity measurements at different confining pressures needed to be accurate to estimate anisotropy parameters. For some samples the first break estimation was more reliable than others due to the shape of the waveforms.

Figure 2-14a shows the P-wave velocity ranges for sample R-5566. The compressional velocities at different angles were in a range of 13500 to 17000 ft/s for different confining pressures (from 500 to 6000 psi). The assumption, that  $V_{p45}$  was the average between  $V_{p0}$  and  $V_{p90}$ , was close to the actual measured values. The X-axis is plotted in logarithmic scale and the trend-lines show a linear relation between velocity and logarithmic pressure.

Figure 2-14b shows the fast and slow S-wave velocities ( $V_{sh1}$  and  $V_{sh2}$ ) for the sample at 90 degrees from the symmetry plane.

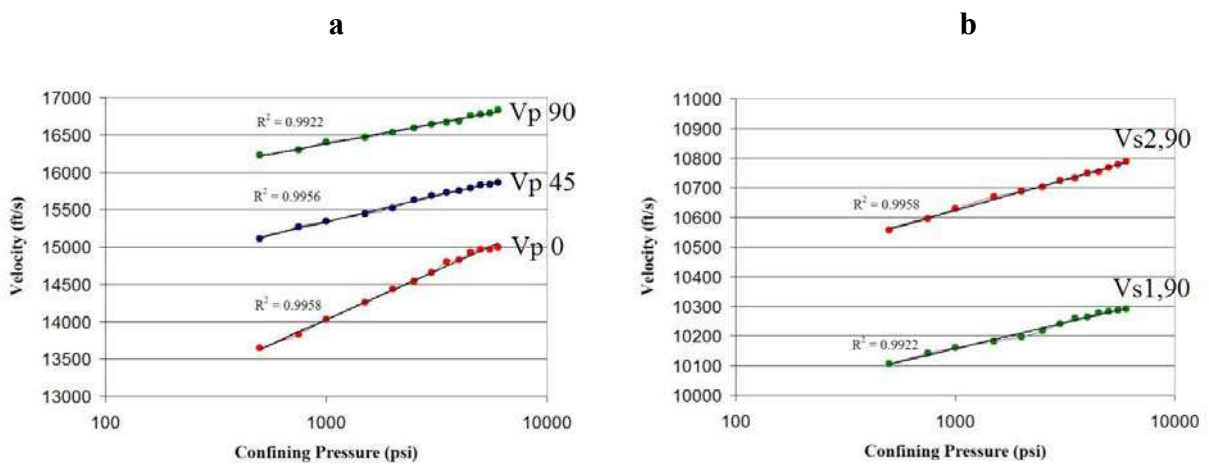


Figure 2-14. P and S-wave velocities versus logarithmic pressure for samples at 5566 feet. a) Velocity of P-waves for 0, 45 and 90 degrees. b) Velocity of fast and slow S-waves for 90 degrees.

Using the equations 2-2 to 2-6, the stiffness coefficients from the different samples at each pressure was calculated. The magnitude relation between coefficients for a VTI material,  $C_{11} > C_{33} > C_{66} > C_{44} > C_{13}$ , agree with the obtained values (Figure 2-15).

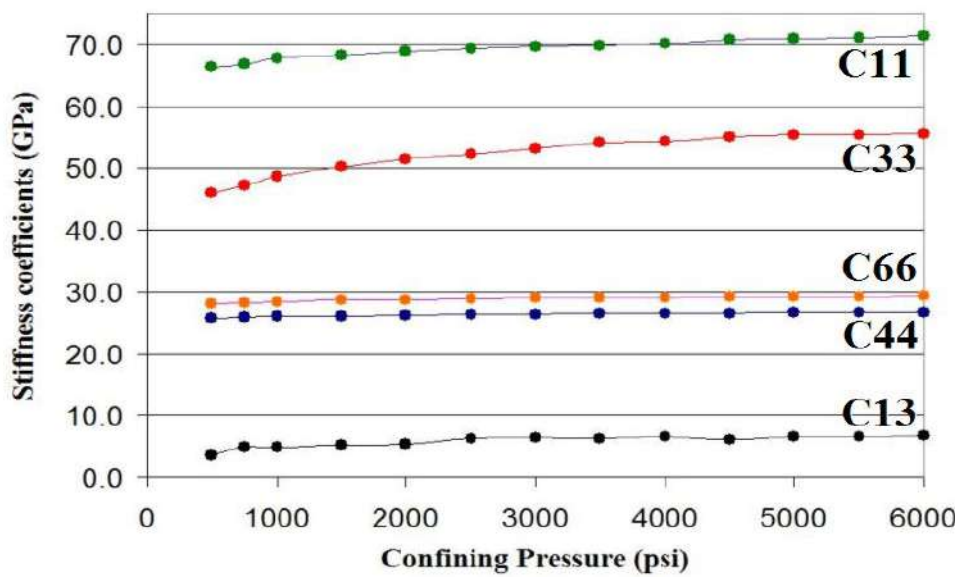


Figure 2-15. Five components of the stiffness tensor for sample 5566.

Figure 2-16 shows  $\epsilon$  or P-wave anisotropy coefficient (blue line) and  $\gamma$  or SH-wave anisotropy coefficient (red line) at different downgoing pressures. The results showed that the Thomsen anisotropy coefficients decrease with pressure. It is intuitive that an increase in pressure closes the cracks within the core samples and the rock becomes more isotropic. A reduction in the matrix seismic anisotropy occurred at high confining pressures (confining pressure of 3500 psi or greater).

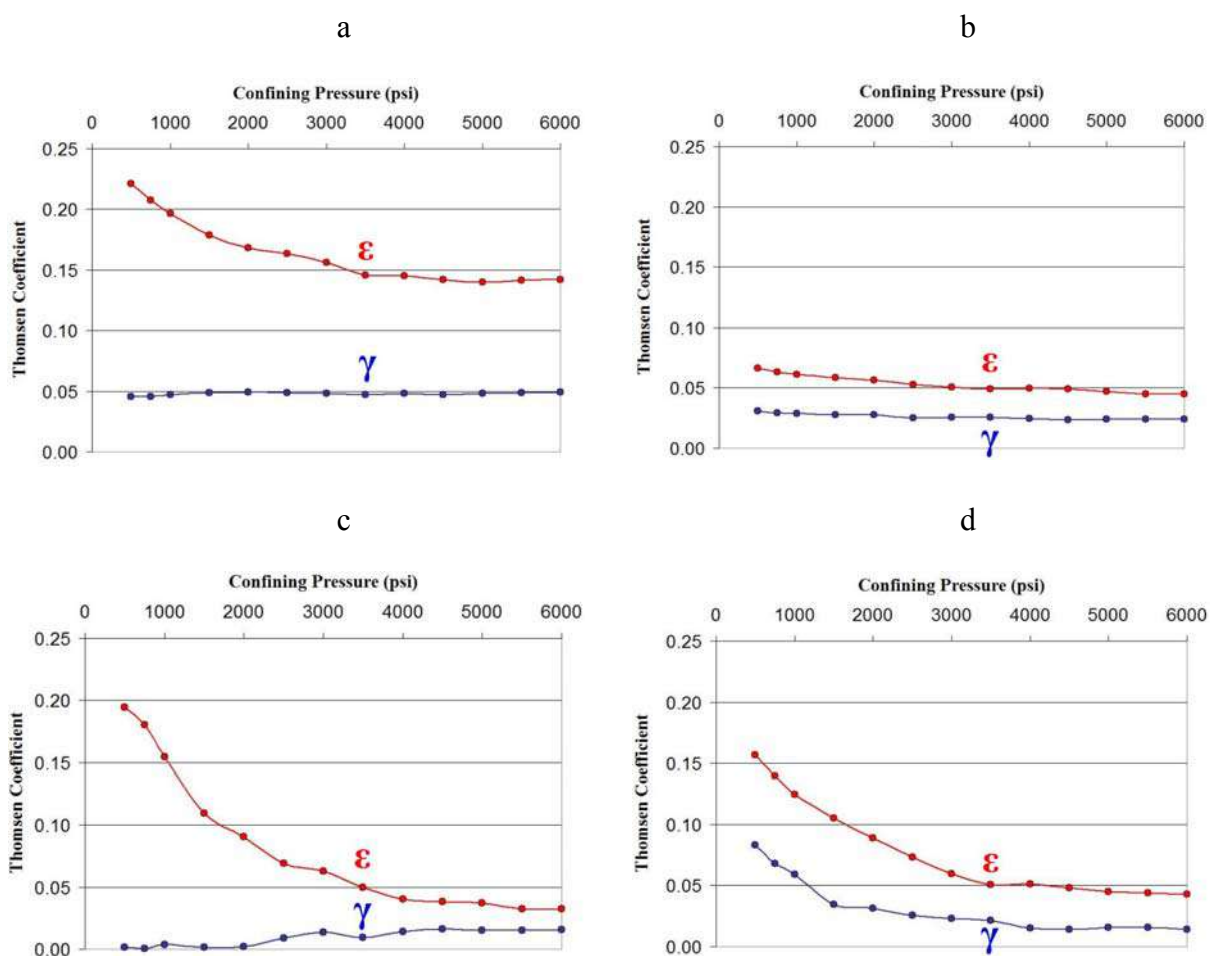


Figure 2-16. Thomsen anisotropy coefficient  $\epsilon$  (blue line) and  $\gamma$  (red line) for samples a) R-5566, b) R-5702, c) R-5727, and d) R-6451.

Figure 2-17 shows the values for anisotropy coefficients  $\delta$  and  $\eta$ . These parameters are important to improve the seismic imaging and this is discussed in detail in section 4.4.  $\eta$  is estimated from the differences of  $\epsilon$  and  $\delta$  (see equation 2-12).

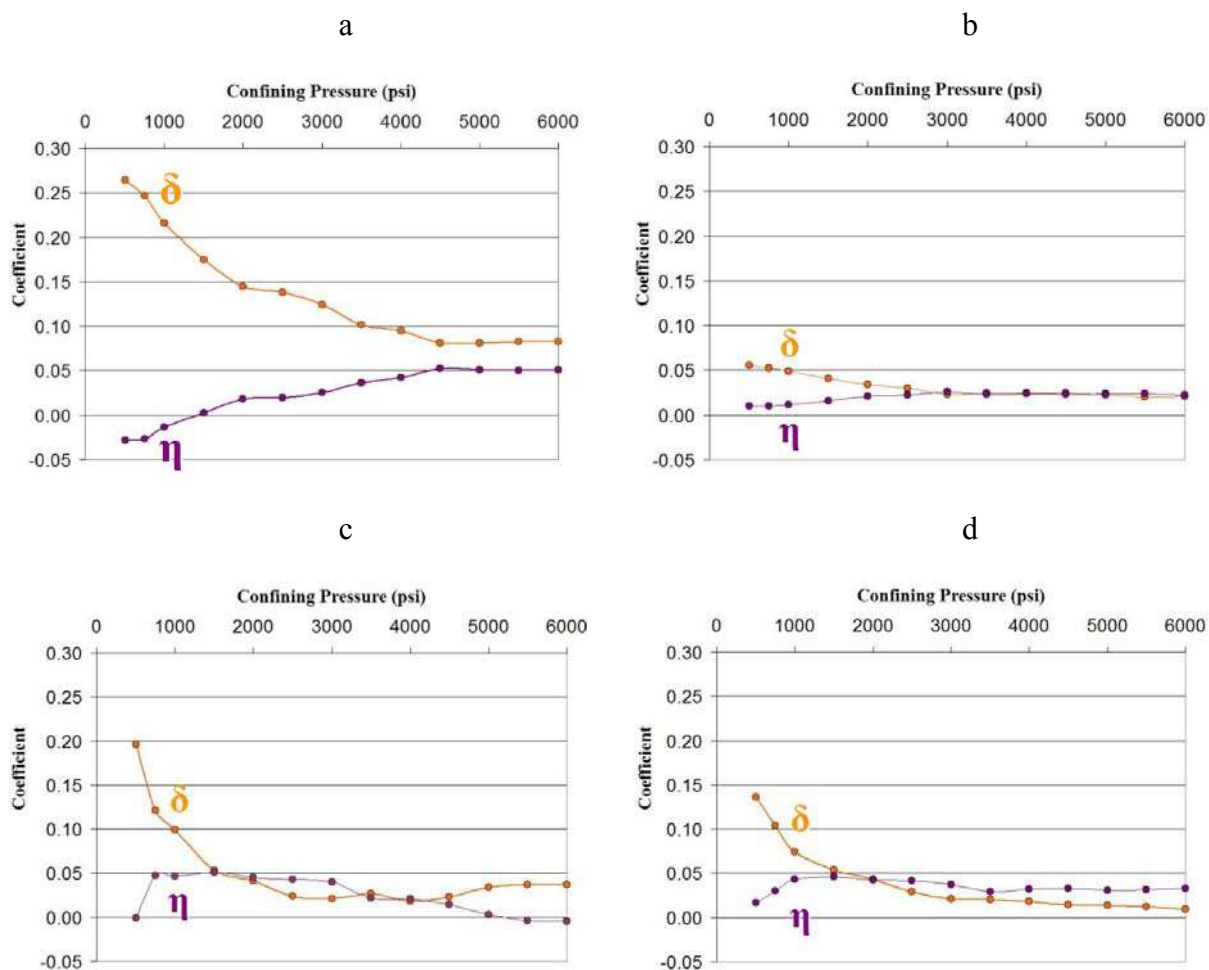


Figure 2-17. Thomsen anisotropy coefficient  $\delta$  (orange line) and  $\eta$  (purple line) for samples a) R-5566, b) R-5702, c) R-5727, and d) R-6451.

The values for  $\delta$  and  $\eta$  have an uncertainty of 25%, providing a reference of the values in tight gas sands, but not allowing a trusty determination of the seismic anisotropy parameters at the reservoir. In Chapter Four, Vertical Seismic Profile was used

to provide a better estimation of  $\delta$  and  $\eta$  at the reservoir overburden using seismic frequencies and scales.

The main objective of the ultrasonic measurements was to estimate the anisotropy parameters at reservoir pressures. From Figure 1-8, reservoir pressure at Rulison was estimated in a range of 2500 psi (hydrostatic pressure) to 5000 psi (overpressure). For shallower sample R-5566 (800 feet below the top of the reservoir), pressures range from 2500 to 4500 psi. For sample R-6451 (close to the reservoir bottom), pressure ranges from 3000 to 5000 psi.

Table 2-3 shows the values of the anisotropy parameters in a range from 2500 psi to 5000 psi of confining pressure. These pressure values are common at the reservoir level and allowed the study of the anisotropy parameters from underpressure to overpressure zones.

The average value of  $\varepsilon$  at reservoir pressure is shown in Table 2-3. For the samples R-5702, R-5727, and R-6451,  $\varepsilon$  was between 4 to 5%. Sample R-5566 had an  $\varepsilon$  average value of 14%. This 10% difference in the  $\varepsilon$  value could be produced by the multiple shaley laminations and heterogeneity that are observed in Figures 2-1 and 2-4. Unlike sample R-5566, the other samples did not have the same amount of laminations and heterogeneity. Another factor that was observed is that grain density and porosity are slightly different between horizontal and vertical samples R-5566 (see table 2.1), which could produce heterogeneities (mineralogy composition) that are not present in the other samples.

The average value of  $\gamma$  at reservoir pressure is shown in Table 2-3.  $\gamma$  is also similar for samples R-5702, R-5727, and R-6451 with values of 1 to 2%. Sample R-5566 has a  $\gamma$  value of 5%, which can be related to the heterogeneity present in the core plug.

Table 2-3. Thomsen anisotropy parameters values at different reservoir confining pressures for samples R-5566, R-5702, R-5727, and R-6451.

<b>Pc (psi)</b>	<b><math>\epsilon \pm 10\%</math></b>	<b><math>\gamma \pm 10\%</math></b>	<b><math>\delta \pm 25\%</math></b>	<b><math>\eta \pm 25\%</math></b>	<b><math>\sigma \pm 25\%</math></b>
<b>5566'</b>					
2500	0.16	0.05	0.14	0.05	0.02
3000	0.16	0.05	0.12	0.06	0.03
3500	0.15	0.05	0.10	0.04	0.09
4000	0.15	0.05	0.10	0.04	0.10
4500	0.14	0.05	0.08	0.05	0.13
5000	0.14	0.05	0.08	0.05	0.12
Average	0.15	0.05	0.10	0.05	0.08
<b>5702'</b>					
2500	0.05	0.02	0.03	0.06	0.02
3000	0.05	0.03	0.02	0.07	0.03
3500	0.05	0.03	0.02	0.02	0.06
4000	0.05	0.02	0.02	0.02	0.06
4500	0.05	0.02	0.02	0.02	0.06
5000	0.05	0.02	0.02	0.02	0.06
Average	0.05	0.02	0.02	0.04	0.05
<b>5727'</b>					
2500	0.07	0.01	0.02	0.10	0.04
3000	0.06	0.01	0.02	0.09	0.04
3500	0.05	0.01	0.03	0.02	0.05
4000	0.04	0.01	0.02	0.02	0.05
4500	0.04	0.02	0.02	0.01	0.03
5000	0.04	0.02	0.03	0.00	0.01
Average	0.05	0.01	0.02	0.04	0.04
<b>6451'</b>					
2500	0.07	0.03	0.03	0.09	0.04
3000	0.06	0.02	0.02	0.08	0.04
3500	0.05	0.02	0.02	0.03	0.07
4000	0.05	0.02	0.02	0.03	0.07
4500	0.05	0.01	0.01	0.03	0.07
5000	0.04	0.02	0.01	0.03	0.07
Average	0.05	0.02	0.02	0.05	0.06

All the samples had  $\delta$  and  $\eta$  values positive and less than 10% at reservoir pressures. As in the case of  $\epsilon$  and  $\gamma$ , the samples R-5702, R-5727, and R-6451 present small values. In the table is shown the average values at the reservoir level in a range of 2 to 3% for both anisotropy parameters. Sample R-5566 had a  $\delta$  value of 9% and  $\eta$  of 5%. These results correlate with the values for shaley sandstone obtained using a VSP at Rulison Field (section 4.2.1).

$V_p/V_s$  ratio increased with pressure and had a range from 1.42 to 1.5. These results agreed with those obtained by Rojas (2005) which studied the relation of  $V_p/V_s$  ratio with lithology and fluids. All the samples have similar  $V_p/V_s$  ratio at reservoir pressure, making it difficult to characterize the lithology content using this parameter alone. Siltstone and shaley sandstone samples R-5566 and R-5702 have a  $V_p/V_s$  higher than sandstones samples R-5727 and R-6451.

## 2.4 Seismic Anisotropy Parameters and Lithology

From the ultrasonic core measurements, it is difficult to determine a correlation between the Thomsen's anisotropy parameters and lithology of the different samples. At lower pressures (below reservoir pressure), differences in the anisotropy parameter values for each sample can be determined. At reservoir pressures the values are similar in all the samples, except R-5566 that is very fine grain sandstone with multiple shaley laminations.

Figure 2-18a shows a relation between  $\epsilon$  and  $\gamma$  for the core samples at reservoir pressures. Three of the samples created a cluster around low values of seismic anisotropy and they correspond to coarse sandstones (R-5727), fine grain sandstone with few siltstones laminations (R-6451) and siltstones (R-5702). Differentiation between these lithologies at reservoir pressures is not feasible. The cluster points at higher anisotropy

values correspond with the shaley sandstones with high amount of laminations. This lithology is easy to recognize even at reservoir pressures.

Figure 2-18b shows a relation between  $\epsilon$  and  $\delta$  for the core samples at reservoir pressures. As in the crossplot of  $\epsilon$  versus  $\gamma$ , the sandstones and siltstones had lower anisotropy, and shaley sandstones had higher anisotropy with  $\delta$  values close to 9%. The uncertainty of  $\delta$  values did not provide definitive conclusions, but from the results obtained, an elliptical anisotropy ( $\epsilon=\delta$ ) is not apparent in the core plugs. These have an important implication at the seismic anisotropy characterization of the reservoir. In the case of elliptical anisotropy, P-wave and SH wave slowness surfaces have an elliptical shape. As in isotropic medium, the phase velocity of the SV-media in elliptical models is constant (Tsvankin, 2001). Therefore, the SV-wave kinematics is not influenced by anisotropy and seismic processing is highly simplified (Normal Moveout or NMO velocity is equal to the horizontal velocity).

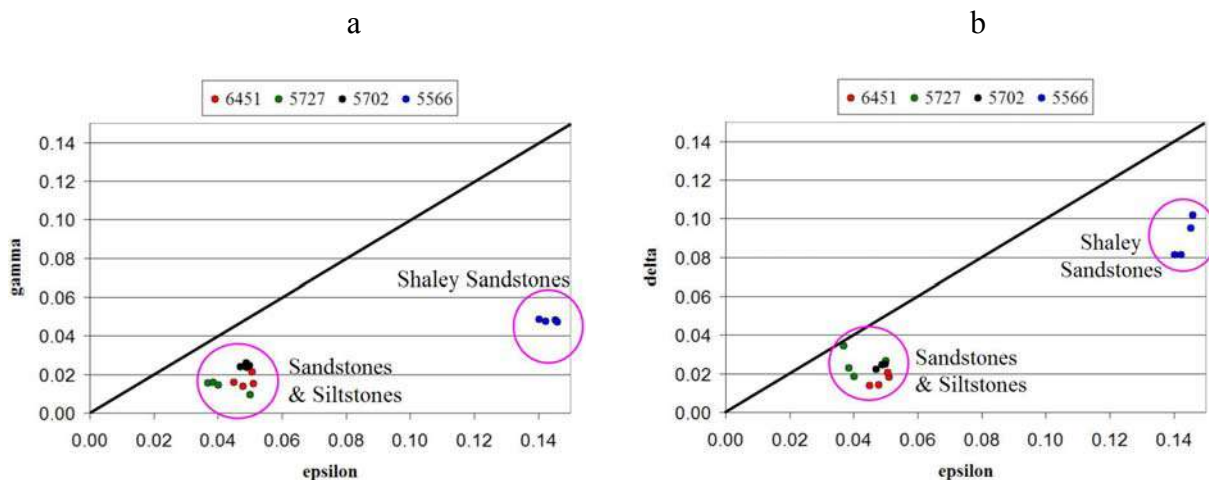


Figure 2-18. a)  $\gamma$  versus  $\epsilon$  for different core samples at reservoir pressure. Sandstones and siltstones samples with few laminations have low anisotropy and values below 5%. Shaley sandstones with high number of laminations have higher anisotropy values with  $\epsilon$  close to 15% and  $\gamma$  close to 5%. b)  $\delta$  versus  $\epsilon$  for different core samples at reservoir pressure. Shaley sandstones with high number of siltstone laminations have higher anisotropy values with  $\delta$  close to 9%.

In general, P-wave anisotropy ( $\varepsilon$ ) is higher than SH-wave anisotropy ( $\gamma$ ) for most of the rocks (Wang, 2002b). Using the 16 data points plotted in Figure 2-18a, a linear relation between  $\gamma$  and  $\varepsilon$  was calculated for sandstones, shaley sandstones and siltstones within Rulison's Mesaverde Group. The best fit to the data is shown in the equation 2-17:

$$\gamma = 0.0042 + 0.3043 \varepsilon \quad R^2 = 0.9026 \quad (2-17)$$

Equation 2-17 is useful where shear wave splitting is known and there is interest in estimated  $\varepsilon$  at the studied interval.

Figure 2-19a shows  $\gamma$  versus  $\varepsilon$  for different lithologies around the world (from Wang 2002b), including the highly anisotropic shales and coals. These lithologies were not measured in the laboratory due to the lack of shale cores from MWX-1. Shear wave anisotropy for these lithologies is determined in Chapter Three from cross-dipoles at Rulison Field. The sandstones tend to cluster around low anisotropy values (below 10%). Figure 2-19b shows the values for tight gas sands. Tight gas sandstones have  $\varepsilon$  values that achieve a maximum of 16% and these P-wave anisotropy values are 2 to 3 times higher than S-wave anisotropy or  $\gamma$ . Wang (2002b) results agree with those obtained in this study with ultrasonic measurements.

A relation between  $\delta$ ,  $\eta$ , and lithology is more difficult to justify due to the uncertainty in the measure of these seismic anisotropy parameters.  $\delta$  and  $\eta$  values higher than 5% are associated with shaley sandstones, and  $\delta$  and  $\eta$  values lower than 3% are related with sandstones or siltstones. This conclusion is verified in Chapter Four with the anisotropy parameters estimated using vertical seismic profiling. A linear relation from Figure 2-18b was estimated in equation 2-18:

$$\delta = -0.0097 + 0.6908 \varepsilon \quad R^2 = 0.9425 \quad (2-18)$$

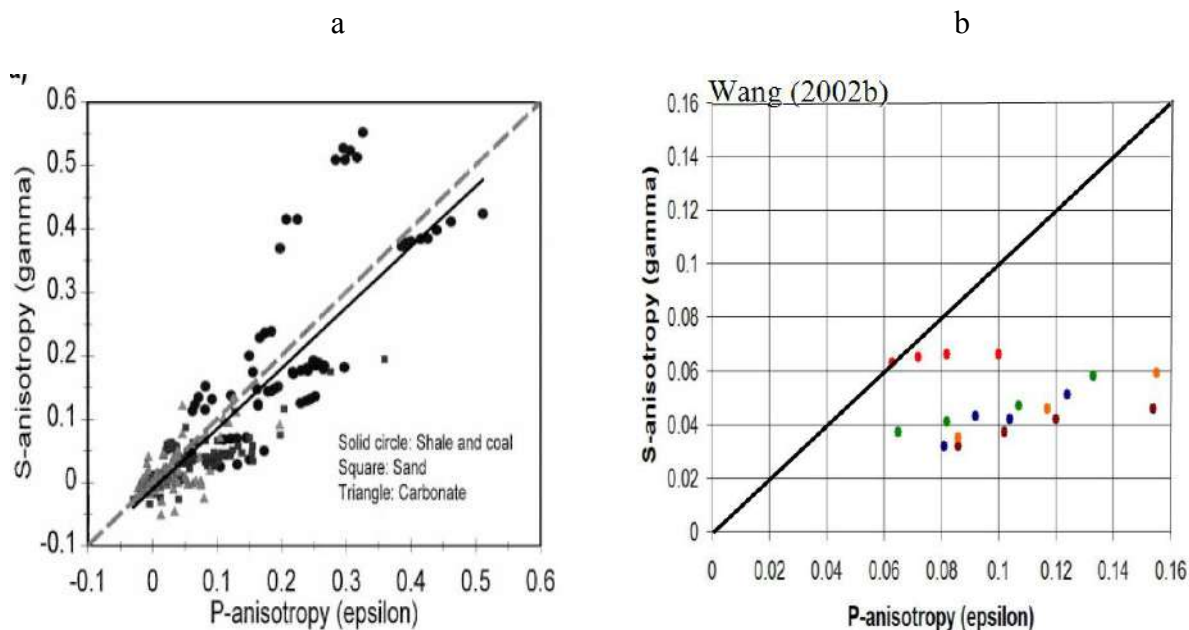


Figure 2-19. Shear wave anisotropy versus P-wave anisotropy for different lithologies. a)  $\gamma$  versus  $\varepsilon$  for shale, coals, sands and carbonates. From Wang (2002b). b)  $\gamma$  versus  $\varepsilon$  for tight gas sands. Created from Wang (2002b).

From the results shown on Figures 2-18 and 2-19 it can be concluded that seismic anisotropy in tight gas sands is not directly affected by porosity. Instead, it is affected by the texture (fractures, cracks, laminations) and clay content.

Figure 2-20 shows the summary of the results from the core plugs measurements. At the left is shown the gamma ray log for every interval, in the middle is a summary of the core sample, lithology and seismic anisotropy parameters, at the right is a plot of NPHI and DPHI (pink areas showed possible gas in the interval). Sample R-5566 was obtained from a mixed interval between sandstone and siltstone, resulting in multiple laminations and heterogeneity. Samples R-5566, R-5702, and R-6451 were obtained from

unmixed lithology intervals, therefore the heterogeneity and laminations were highly reduced.

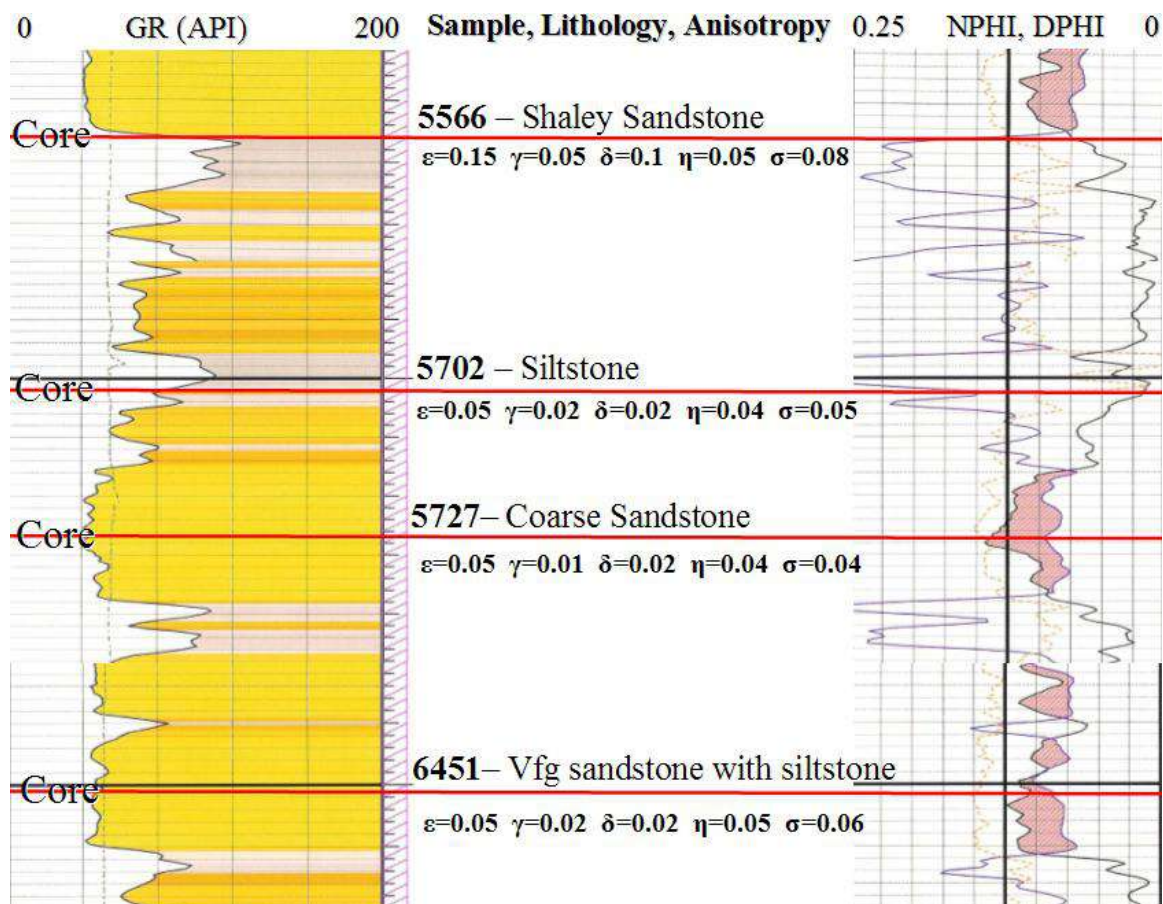


Figure 2-20. Well logs and summary of the core sample measurements results. Left column shows a gamma ray normalized log, middle column shows sample number, lithology and anisotropy coefficients and right column shows a NPHI (neutron) and DPHI logs. Pink zones at the right column are possible gas areas.

## 2.5 Assumptions and Shortcomings

The assumption that the symmetry of the core samples is Vertical Transverse Isotropy (VTI) was an important shortcoming of the anisotropy parameters estimation.

Where the symmetry of the samples was different, the calculations can only provide an approximation of anisotropy parameter values. For every sample, a quality control of the data was made to verify how close they were to VTI symmetry. The results showed that the samples results slightly differ from VTI symmetry, the causes could be produced due to: (1) core samples have a different symmetry (such as orthorhombic) or (2) vertical and horizontal samples were not cut exactly parallel and perpendicular respectively from the symmetry axis.

## 2.6 Summary

The ultrasonic rock measurements obtained from the four core plugs produce coherent results assuming VTI symmetry for sandstones, but this type of symmetry may not be the best one to fit the data. In Chapter Four, an orthorhombic symmetry is suggested to characterize the overburden.

At reservoir pressures, three of the four core plugs showed  $\epsilon$  values of 0.05 and  $\gamma$ ,  $\delta$  and  $\eta$  values of less than 0.03. These results correlated with the assumption that tight gas sandstones are close to isotropic in the lack of heterogeneities.

One of the samples (R-5566) showed values of  $\epsilon$  0.14,  $\gamma$  0.05,  $\delta$  0.09, and  $\eta$  0.05. The CAT analysis showed that R-5566 is highly heterogeneous with multiple sets of laminations in different directions. Furthermore, the grain density and porosity is different between the vertical and horizontal samples showing a high degree of complexity. This sample is an example of the highly heterogeneous Mesaverde Group, and rock type and complexity in the reservoir will determine the seismic anisotropy.

From the measures, it can be estimated that the matrix of sandstones, shaley sandstones, and siltstones of the Mesaverde Group around the well MWX-1 have  $\epsilon$  values from 0.04 to 0.15,  $\gamma$  values from 0.01 to 0.05 (without including fracture areas),  $\delta$  values

from 0.02 to 0.09,  $\eta$  values from 0.02 to 0.05, and  $\sigma$  values from 0.05 to 0.13. All these values were positive and reflected only the anisotropy due to lithology and heterogeneity (mainly laminations) in core samples. From well logs, it is known that shear wave splitting is higher in fractured sandstones and coal layers.

## CHAPTER 3

### ELASTIC PROPERTIES FROM CROSS-DIPOLE SONIC LOGS

In Chapter Two, anisotropy parameters values were obtained from four intervals of the Mesaverde Group. These values provided an estimation of seismic anisotropy. With sonic logging, it is possible to obtain the variations of seismic anisotropy for a complete interval and provide continuous information of rock properties in larger volumes than with the laboratory data. Another advantage is that sonic logs have lower frequency than ultrasonic measurements.

S-waves data from three cross-dipole sonic logs acquired in the field were analyzed with the purpose of estimating shear-wave splitting values of characteristic lithologies (clean to shaley sandstones, shales and coals).

Shear waves are less sensitive to fluid than P-waves, and therefore S-waves provide more information about the rock matrix.

#### 3.1 Quality Control of the Data

Many factors can affect log measurements. For example, when these measurements are made in the borehole with wireline logging tools, they are usually affected by the mud zone around the borehole. Mud may penetrate the formation and immediately affect the results of sonic logs and well logs measurements. Not taking invasion into account can lead to inaccuracies in elastic rock properties estimations.

In tight gas sandstones (low permeability and porosity reservoirs), rock predictions are complicated, because conventional formation-evaluation techniques are often not applicable. Briceno (2004) developed and applied a forward model and inversion routine that uses not only shallow resistivity, but also porosity logs as input, and produces an invasion profile that differs from the typical step invasion model. Briceno (2004) applied this methodology at Rulison Field. She showed that in the Williams Fork Formation, the most frequent invasion models are shallow with a flushed zone shallower than the depth of investigation, and this is explained by the low permeability of the formation.

Briceno's (2004) study shows that in Rulison Field the sonic logs are not directly affected by the invasion. So, this study assumes that the integrity of the sonic logs measurements is preserved and measures the virgin formation.

### **3.2 Maximum Stress Orientation and Fractures from Well Logs**

Borehole breakouts are hole elongations (that point to the  $SH_{\min}$  direction) that resulted from stress concentrations in a nonuniform stress field (Springer, 1987). Using well logs information, several authors suggested that the present-day stress orientation in Rulison area varies from ENE to ESE (Reinecker, 2005 and Koepsell et al., 2003). Matesic (2007) found at Rulison Field a maximum stress orientation N70°W.

Lorenz and Finley (1991) stated that the natural fractures have a west-northwest or east-west regional orientation oblique to the production trends (northwest). Kuuskraa et al. (1997a) suggested natural fractures with a N30°W and N60°E orientation associated with faults and joints that enhance permeability. Kuuskraa et al. (1999) described stress induced micro-fractures oriented N80°W at the MWX site location. Gomez et al. (2003)

used core samples and observed microfractures (fractures observed with magnification of 10x) that coincide with the fracture orientation trend west-northwest.

Matesic (2007) used image logs at Rulison Field and summarized the published natural fracture orientations in three sets: (1) an E-W extensional fracture set parallel to the maximum present-day stress; (2) a N30°W parallel to the main structural and production trend and (3) a N60°E strike orthogonal to the N30°W set. Matesic's (2007) studies found that induced and open fractures show a mean strike of N80°W with minor variations of 15 degrees. Matesic (2007) also found that healed fractures (fractures infill with minerals) have a mean strike of N30°W and two secondary strikes N80°W and N70°E.

Matesic (2007) could not find a definitive relationship between faults, fractures, sandstones beds, and gas seeps. One objective of this chapter is to establish a relation between production and natural fractures using shear-wave splitting and gas concentration logs.

Rojas (2005) observed in her study that high anisotropy values are related to very thin sands at the well RWF 332-21. It is possible that these thin sands are highly fractured and create an increase in the shear-wave splitting. One of the suggestions of Rojas (2005) was to study the sensitivity of  $V_p/V_s$  to fractures. Different studies (Guest et al., 1998) suggest that an increase of  $V_p/V_s$  could be expected due to the effect of fracture filling fluid on shear-wave propagation. Rojas (2005) suggested that gas filled fractures can decrease the shear wave velocity while leaving the P-wave velocity unaffected, hence increasing the  $V_p/V_s$ .

### **3.3 Shear Wave Splitting and Fracture Analysis**

Shear wave propagation is controlled by the rigidity of the rock mass. In the presence of a fracture and the angles of S-wave to that fracture, a shear wave will split into two waves with orthogonal polarizations which will travel at different velocities. Assuming a VTI media, two shear wave directions can be defined. The shear wave that is polarized parallel to the fractures intersects fewer fracture planes and will therefore travel faster, receiving the designation of S1 or fast shear. The shear wave polarized perpendicular to the cracks will travel at a lower velocity, receiving the name S2 or slow shear.

There are three cross-dipole sonic logs located at Rulison field. They are shown in Figure 1-1. Different crossplots of petrophysical properties were done in order to reveal the interdependence among them. These crossplots were used to identify relations between shear-wave splitting, lithology, and fractures.

### **3.4 Cross-dipole Well Logs**

#### **3.4.1 Well RWF 332-21**

RWF 332-21 is located at the southeast corner of Rulison Field. This well is located 2000 feet southwest of the 2003 VSP well (RMW 30-21), providing the best correlation with shear wave splitting from the VSP.

Figure 3-1 shows the well logs used to estimate a relation between lithology, fractures and gas concentrations at Rulison Field between UMV shale to Cameo coal. The lithology indicators included gamma ray, volume of shale, and density logs; the

fracture indicators included shear wave splitting, and the gas concentration indicators included gas unit logs. A mean value of shear wave splitting in this interval was 1.25%, suggesting fractures within the UMV shale to Cameo coal interval. The lithology in the interval varies from shaley sandstones to siltstones, and there are no coal layers within this level. Gas concentration achieved a maximum at proximity to the Cameo coal.

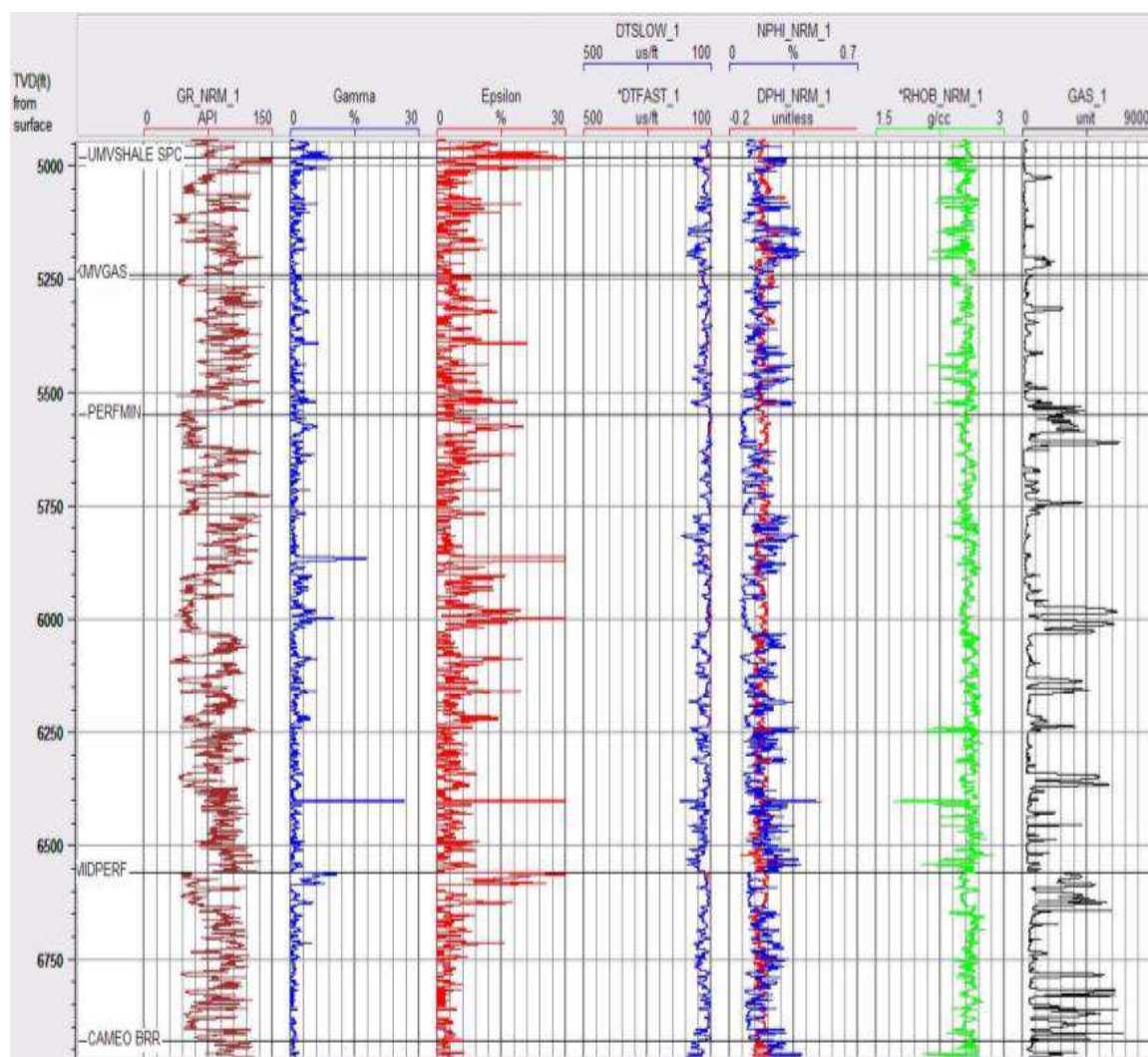


Figure 3-1. RWF 322-21 well logs from UMV shale to Cameo coal. From left to right: normalized gamma ray (brown log), shear wave splitting (blue log),  $\epsilon$  estimated from  $\gamma$  (red log), fast and slow shear (blue and red log), DPHI and NPHI (blue and red log), density (green log), and gas units (black log).

Figure 3-2 shows shear wave splitting ( $\gamma$ ) versus Vshale crossplot for the UMV shale to Cameo interval. Shear wave splitting values higher than 3% accumulated in lithologies with gamma ray values less than 65 GAPI (60% of plotted samples). This concentration of shear wave splitting indicates that fracture areas in this interval are common in sandstones layers. This fracture distribution in sandstones was also observed by other authors (Matesic, 2007 and Rojas, 2005) in Rulison Field.

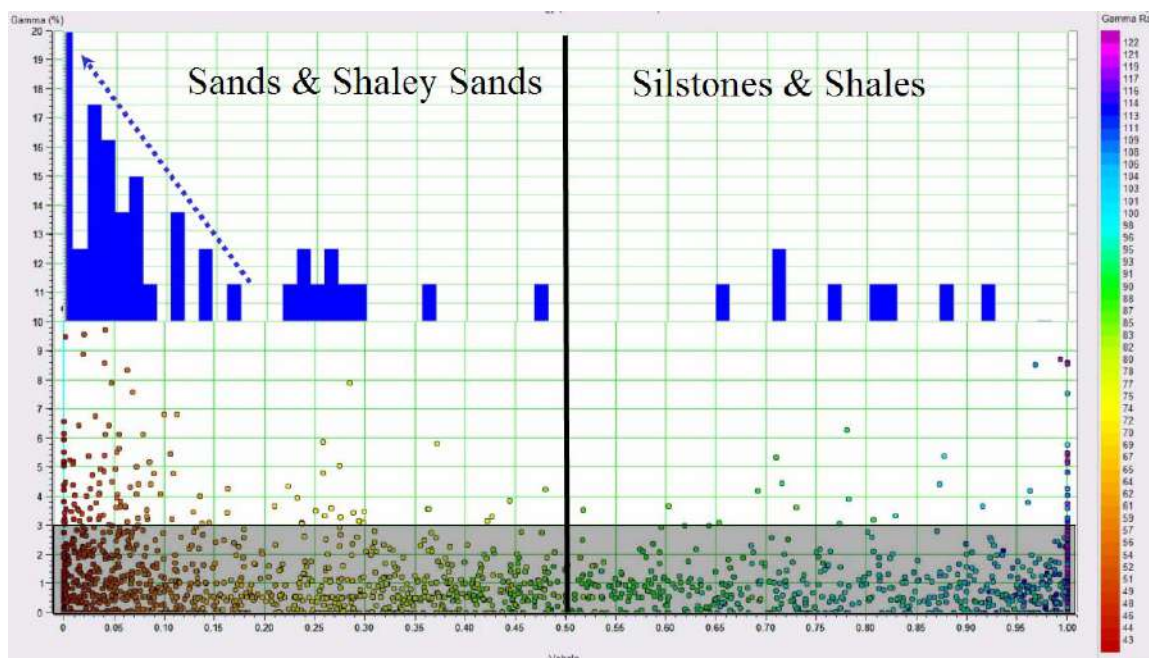


Figure 3-2. Crossplot shear wave splitting versus lithology from UMV shale to Cameo. Y axis plotted shear wave splitting values in percentage. X axis plotted Vshale values (from 0 to 1). Colors indicated gamma ray values from shaley sands (hot colors) to shales (cold colors). Upper graph shows a histogram for  $\gamma$  values higher than 3% (dots outside the shaded black box).

Figure 3-3 shows the well logs used from Cameo Coal to the Rollins Formation. There are several coal layers in this interval that generated high shear wave splitting. Shear wave splitting mean value was 2.7%, showing a significant increase due to the

presence of multiple fractures sets in the coal layers. Lithologies are mixed shaley sandstones, siltstones and coals. The gas concentration is higher within this interval.

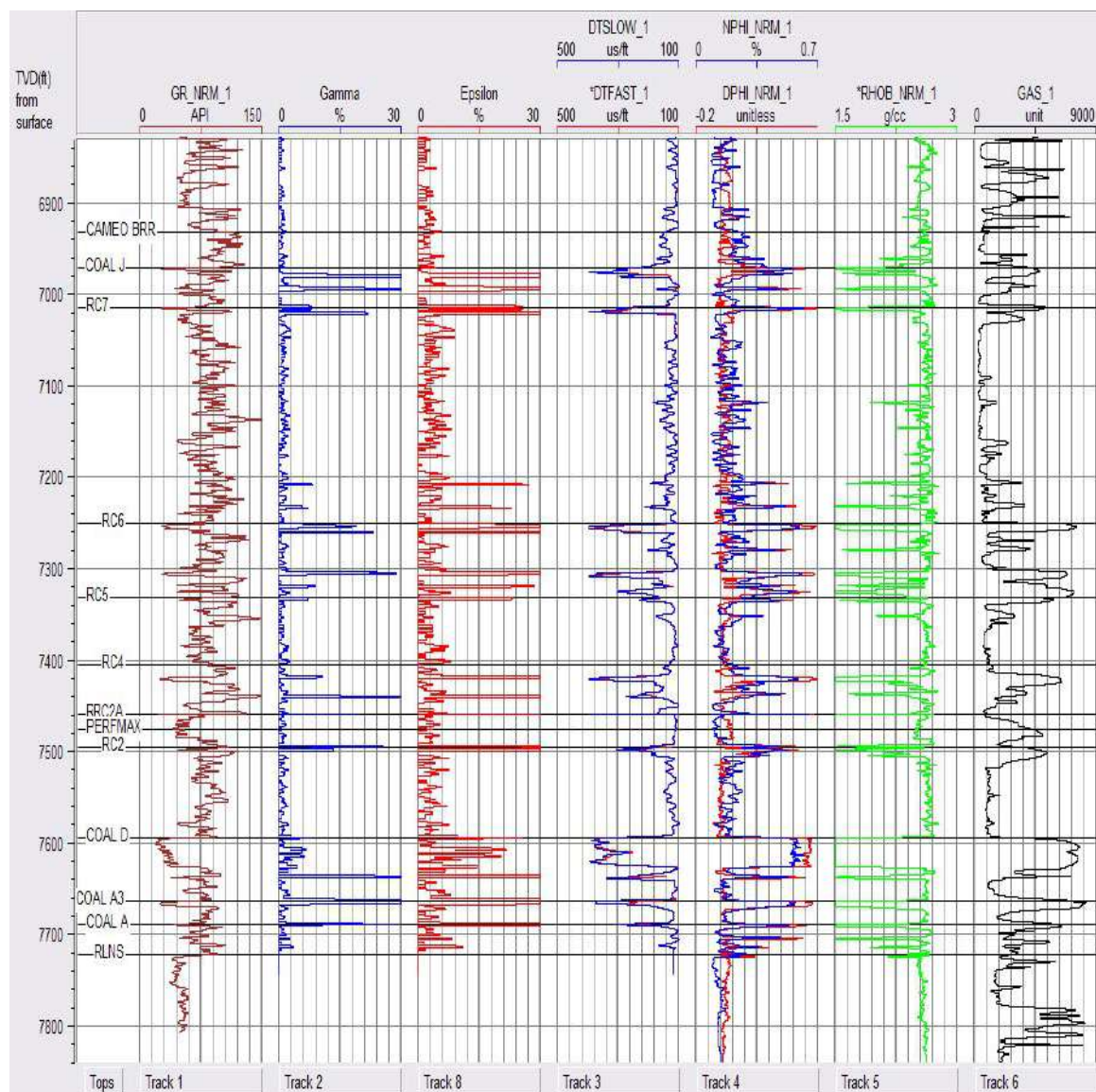


Figure 3-3. RWF 332-21 well logs from Cameo Coal to the Rollins Member. From left to right: normalized gamma ray (brown log), shear wave splitting (blue log),  $\epsilon$  estimated from  $\gamma$  (red log), fast and slow shear (blue and red log), DPHI and NPHI (blue and red log), density (green log), and gas units (black log).

Figure 3-4 shows shear wave splitting versus Vshale crossplot from the Cameo coal to the Rollins Formation. There is a correlation between high shear wave splitting values and coal layers (indicated with blue dots). Shear wave splitting values are higher than 3% in lithologies with gamma ray values less than 65 GAPI (55% of plotted samples). Fifty percent of lithologies with less than 65 GAPI are coal layers.

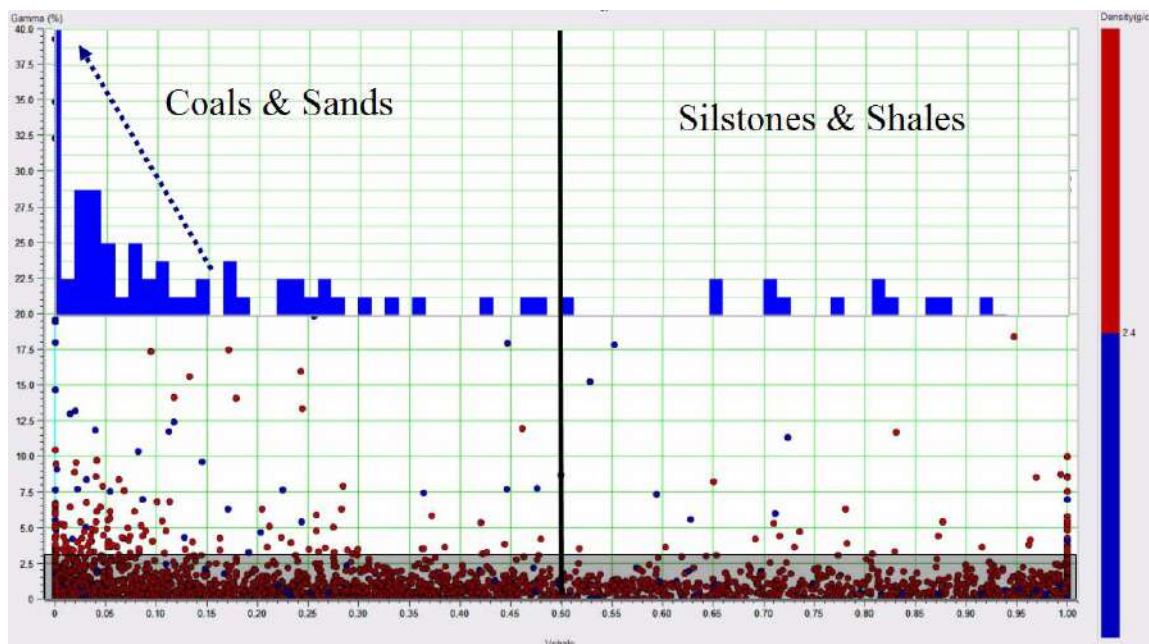


Figure 3-4. Crossplot of shear wave splitting versus lithology from Cameo coal to the Rollins Formation. Y axis plotted shear wave splitting values in percentage. X axis plotted Vshale values (from 0 to 1). Colors indicated density values. Density values less than 2.4 gr/cc (blue dots) represented coals. Upper graph shows a histogram for  $\gamma$  values higher than 3% (dots outside the shaded black box).

Figure 3-5 shows an image log from RWF 332-21 with two coal layers, the upper zone is unfractured and the lower zone is fractured. Coal layers with fractures enhance the natural permeability of the rock. In the early years of Rulison Field production, the main targets were the coal layers within the Cameo.

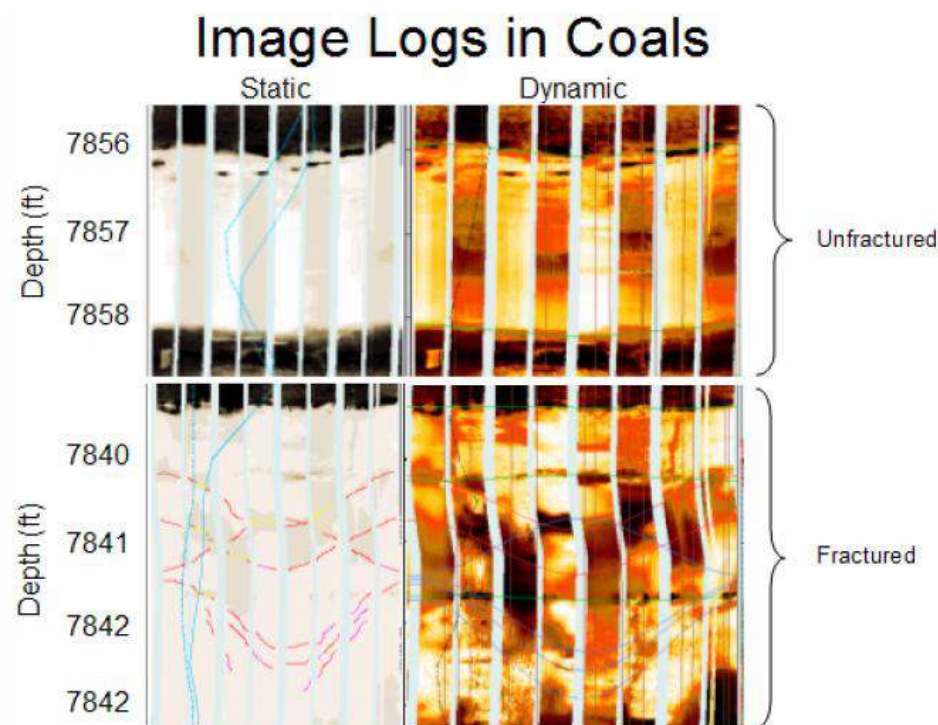


Figure 3-5. RWF 332-21 image logs showing a fracture and unfractured coal. From Keighley (2006).

Figure 3-6 shows possible fracture zones between the UMV shale and the Rollins Formation. From UMV shale to Cameo coal are 9 possible fracture areas spaced over 1900 ft. Most of the fracture areas are located in sandstones to shaley sandstones intervals. From Cameo coal to the Rollins Formation there are 15 fractured areas. Most of the fractures are located in the coal layers, with a few of them located in sandstones. The interval between the Cameo coals to the Rollins shows high gas unit concentrations.

The azimuth frequency shows a consistent east-west trend with a secondary set oriented north-west in the interval between UMV and Cameo coal. Below Cameo coal, the azimuth frequency is more complex, showing multiple sets of fracture orientations. The multiple sets show that coals are heavily fractured with at least three sets (N30°W,

N60°E and N70-80°W) of natural fractures. These fracture orientations correlate with those observed by Kuuskraa et al (1997a).

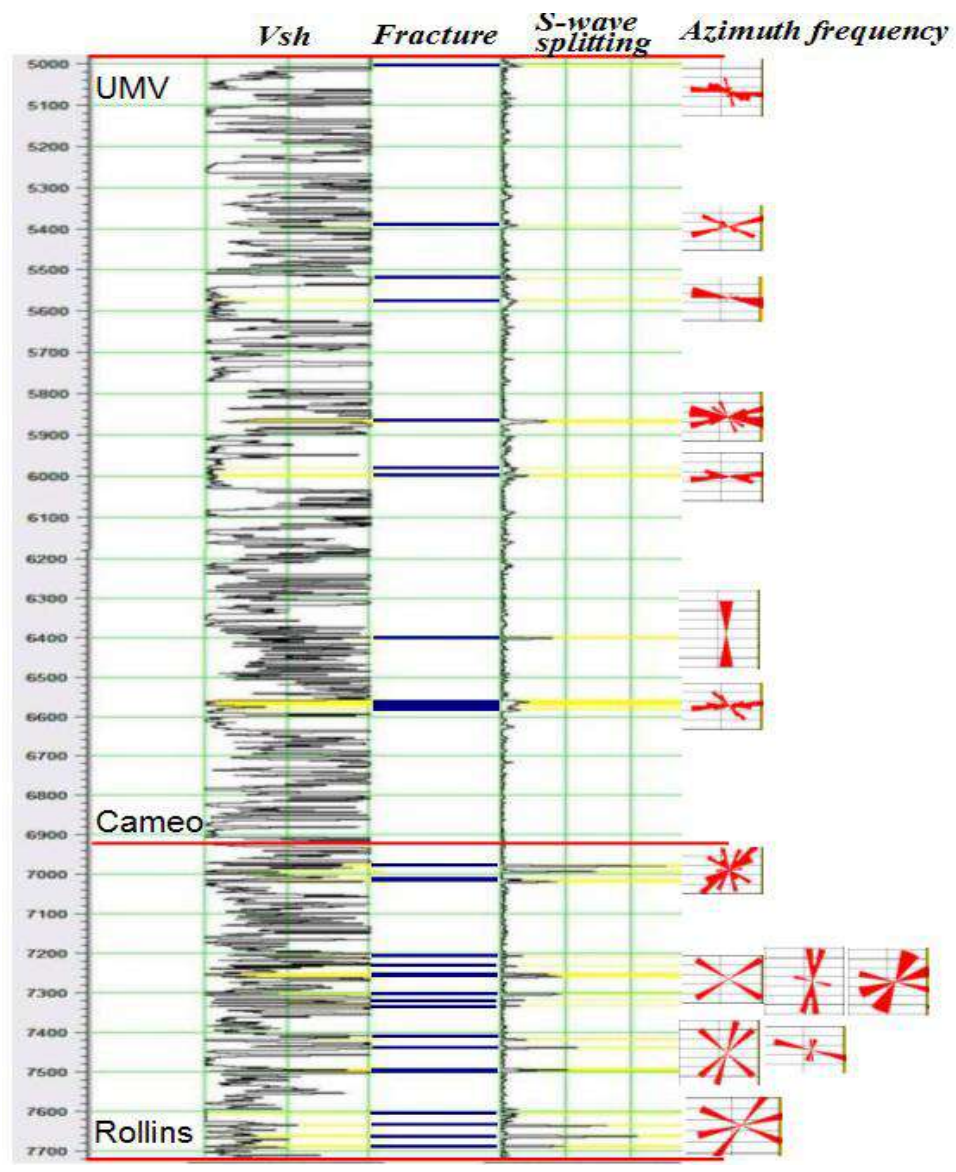


Figure 3-6. Fracture areas in RWF 332-21 from UMV to the Rollins Formation. From left to right: Vshale plot, fracture zones (indicated by blue lines), shear wave splitting percentage and azimuth frequency calculated by Halliburton. Yellow lines indicated areas of more than 5% of shear wave splitting and gamma ray less than 85 GAPI.

There is a good correlation between shear wave splitting and gas content in the well logs. Figure 3-7 shows areas of high anisotropy that correlates with high gas content zones. Figure 3-8 shows a plot of mean gas unit content versus shear wave splitting. As the shear wave splitting increase it also increase the mean gas unit content. Zones with high shear wave splitting (more than 4%) shows high gas unit content (more than 3000 gas units) in 87% of the sample intervals.

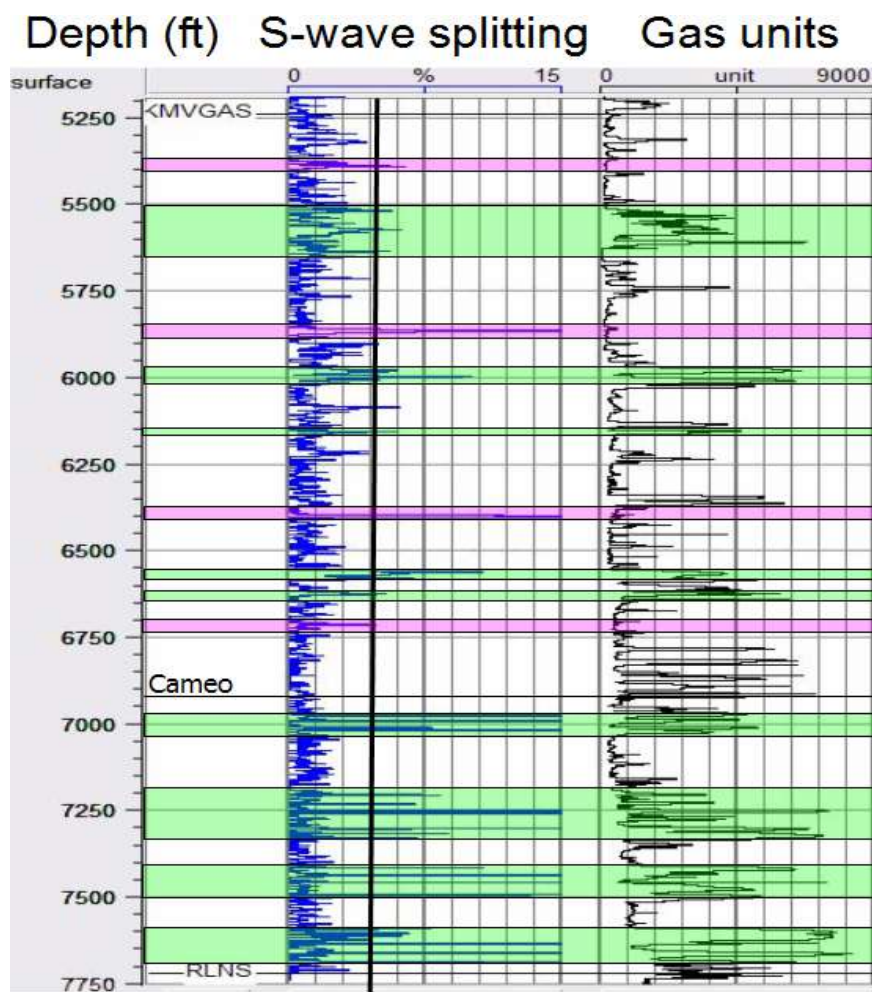


Figure 3-7. RWF 331-20 well logs from KMV gas to the Rollins Formation. From left to right: shear wave splitting (blue log) and gas units (black log). High shear wave anisotropy and gas zones correlation is indicated in green color and areas of poor correlation is indicated in pink color.

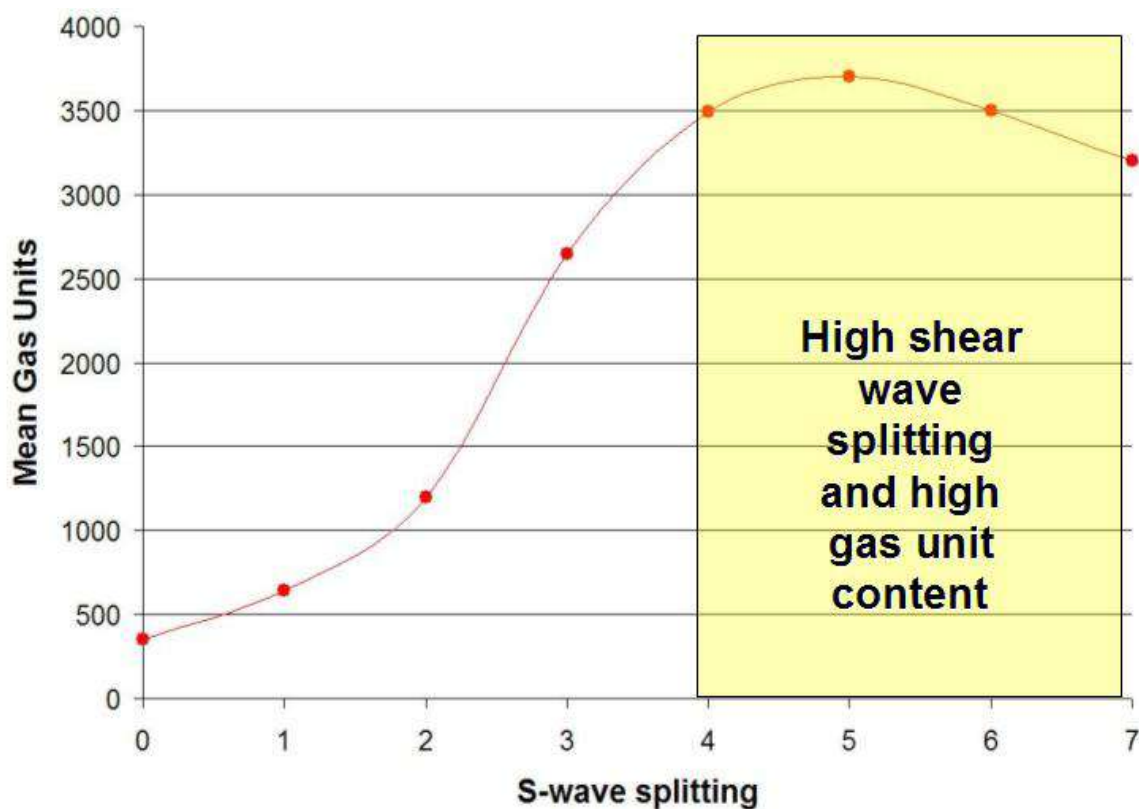


Figure 3-8. Mean gas units versus shear wave splitting at RWF 332-21. There is a good correlation between areas of high shear wave splitting and an increase in the mean gas unit content.

A possible explanation of this good correlation is that gas originated in the coal layers below top Cameo and migrated through natural fracture systems to the overburden layers. In the areas where there is high shear wave anisotropy (fracture zones), the gas concentrates in the layers around the fractures and creates an excellent match between gas content and shear wave splitting. It is also possible that the mud weight affected the measurement of gas unit logs providing a false correlation with areas of high shear wave splitting.

A good agreement between natural fractures and gas content allows the geoscientist to determine perforation zones within the well with confidence and creates a significant importance to identify high shear wave splitting values (more than 4% at Rulison Field). An interesting point is that the areas of poor correlation between 6750 and 6900 feet were just above the Cameo coal interval. One explanation of this anomaly could be the highly fractured nature of Cameo coals. From seismic data, it is known that Rulison Field is compartmentalized by a system of faults. These faults allowed the migration of gas, not just vertically but also laterally (Cole and Cumella, 2003).

### **3.4.2 Well RWF 542-20**

RWF 542-20 is located in the central part of Rulison Field. Figure 3-9 shows the image log analysis at the location (Matesic, 2007). Matesic did not find a correlation between gas seeps (“bubbling” shapes at the image logs) and fracture areas, but suggested that this lack of relation was caused by the mud weight in the borehole. Matesic divided the fractures into three sets: resistive (healed), open, and drilling induced. Healed fractures are natural fractures filled with minerals, and open fractures are natural fractures without mineral fill.

Similarities between shear wave splitting analysis at well RWF 542-20 and RWF 331-20 include:

- Shear wave anisotropy is higher at the Cameo coal to the Rollins Formation interval than the UMV shale to Cameo coal interval. Shear wave splitting value for UMV shale to Cameo is 4%. Shear wave splitting value for Cameo coal to the Rollins Formation is 5.5%.
- High shear wave splitting is located in lithologies with gamma ray value less than 65 GAPI (66% of the samples). As in RWF 331-20, high shear wave

splitting is sometimes located in higher gamma ray values lithologies, suggesting that the fractures are not just limited to clean sandstones and coals.

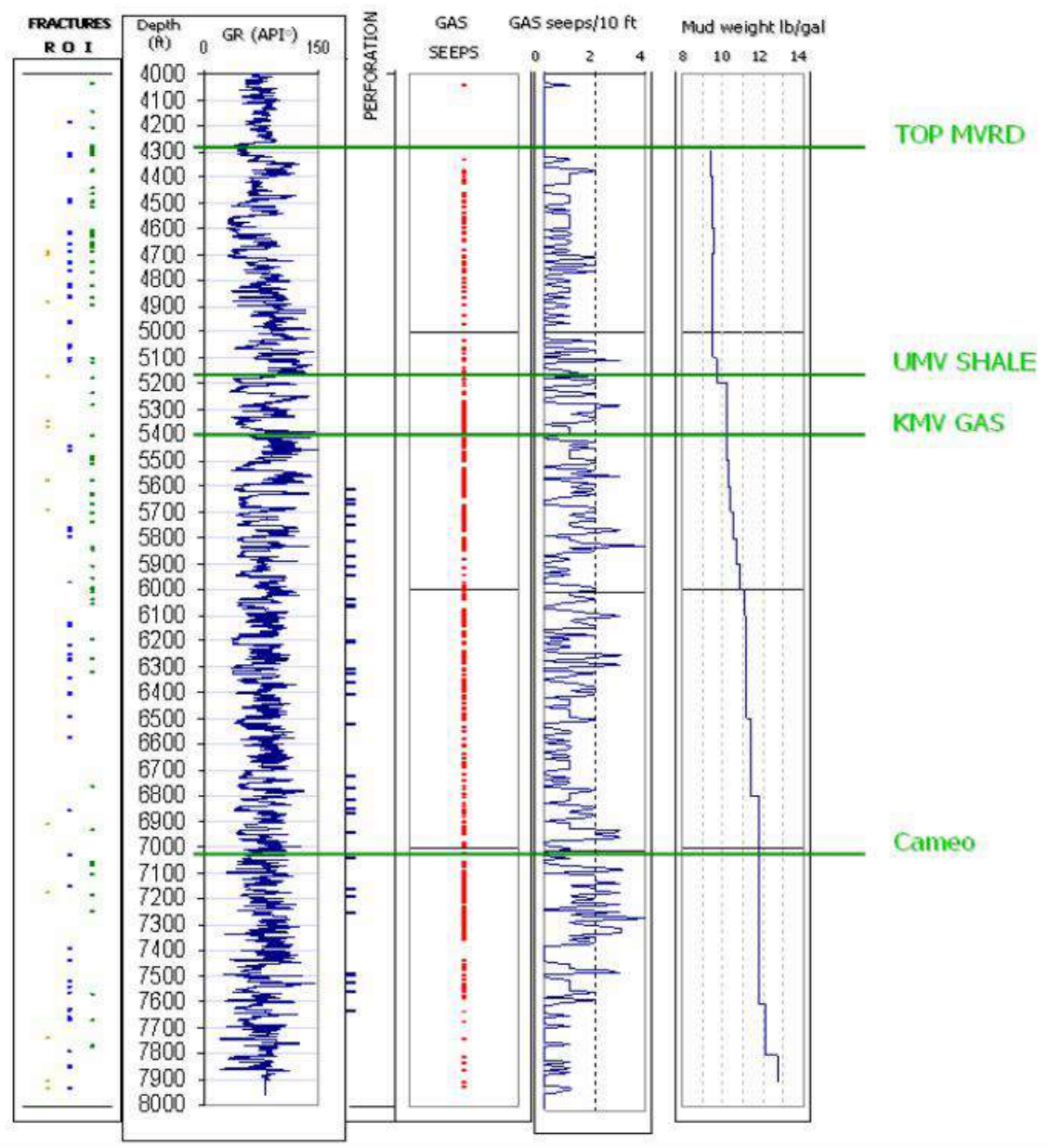


Figure 3-9. Combination of fractures (R=Resistivity or healed fractures, O=Open fractures and I=Induced fractures), gamma ray, gas seep, gas seep density, and mud-weight logs in the RWF 542-20 well. From Matesic (2007).

Gas unit logs were not available in RWF 542-20. This did not allow establishing a relation between high anisotropy areas and gas concentration.

### **3.4.3 Well RWF 441-20**

RWF 441-20 is located in the north central area at Rulison Field (Figure 1-1). The well was drilled in the summer of 2006 in an effort to calibrate the time-lapse data. The datasets include a cross-dipole, passive monitoring, VSP, and pressure test recorded simultaneously. At the time of this study, the cross-dipole information was not available.

A Halliburton report (2006) showed an analysis of the well logs in RWF 441-20. The main conclusions obtained from the report include:

- Drilling induced fractures show a mean orientation east-west (94 and 274 degrees).
- Natural open fractures show a mean orientation east-west (mean strike 89 degrees). The highest density of natural open fractures is between 5570 ft to 6160 ft. The same strike orientation of drilling and natural fractures suggested an alignment of paleo and present day maximum horizontal stress directions. Drilling induced fractures are spread evenly throughout the logged interval.
- Mineralized fractures show a mean orientation east-west (mean strike 99 degrees) with secondary orientations at N60W and N70E. The highest density of mineralized fractures is between 6450 ft to 6500 ft.
- There is a correlation between natural fracture areas and an increase in the total gas curve, along with visible gas entry into the borehole. Locations that exhibit these features are located at 5625 ft., 6075 ft., 6275 ft., and 6650 ft.

- Shear wave anisotropy analysis run in areas of more than 11% of shear wave splitting and GR below 85 API showed an azimuthal direction mean of 94 degrees. This value correlates to the mean natural open and induced fracture strike of 90 degrees.
- Bedding dip direction showed a northerly trend with a highly variable dip magnitude of 30 degrees.
- Structural strike trends strongly to the north-west. Sedimentary dips are north-east.

### **3.6 Summary**

Natural (open and mineralized) and induced fractures have a preferential east-west orientation. The alignment of paleo and present day maximum horizontal stress directions is similar.

A correlation between high shear wave splitting and lithologies was detected. The high shear wave splitting zones from UMV shale to the Rollins Formation are distributed in all lithologies, but showed a clear increase in lithologies of less than 65 GAPI (clean sandstones and coals).

The quantity of fracture events tends to increase four times their density (from 200 feet to 50 feet) in the coal zones (below Cameo coal). The coals are highly fractured with multiple fracture orientations and provide an excellent zone of enhanced natural permeability.

A correlation between high shear wave splitting areas and gas concentrations is observed in the gas production area (below KMV gas marker). This correlation suggests that perforations should be made in high shear wave splitting zones (more than 4%) and

gas rich areas (detected from logs) to take advantage of natural fracture systems. The good correlation between fractures and gas concentrations suggests that gas migration is enhanced by the natural fracture system at Rulison Field.

In this chapter the effect of natural fractures on shear wave splitting at Rulison Field are studied. There are additional causes that could created high shear wave splitting, these include: (1) S-wave velocity affected due to stress and (2) drilling induced fractures.

## CHAPTER 4

### ESTIMATION OF SEISMIC ANISOTROPY USING P-WAVE VSP DATA

The geophones in a typical VSP geometry are located in the subsurface, providing a unique opportunity for measuring local anisotropy in the seismic frequency range. There are different options for anisotropy estimation: one approach relies only on traveltimes of seismic waves (based on velocity analysis or tomography); another approach calculated the slownesses or time derivatives; another supplements those times with directions of polarization or particle motion measured by three-component (3C) geophones in a wellbore.

Hsu et al., 1991; and de Parscau, 1991; independently proposed the so-called slowness-polarization method for anisotropy estimation. Horne and Leaney, 2000; popularized this method. The concept of slowness-polarization is explained in Figure 4-1. The apparent slowness,  $q$ , along a well is the derivative of the traveltime,  $t$ , with respect to the geophone depth,  $h$ . Then,  $q = dt/dh$  is a local quantity that does not depend on the velocity structure of the overburden. Another measurable local quantity is the wave polarization direction,  $U$ , and it is quantified by two angles:  $\psi$  (polar angle) and  $\phi$  (azimuthal angle).

The most important issue for anisotropy estimation is finding the parameter combinations that govern the observed slowness-polarization dependence,  $q(U)$ , of plane waves and determining the wave modes that constrain these combinations. The authors above stated that four quantities defining the elastic properties of VTI media (the vertical velocities  $V_{p0}$ ,  $V_{s0}$  and Thomsen anisotropic coefficients  $\epsilon$ ,  $\delta$ ) influence both the apparent P- and S-wave slownesses,  $qP(\psi)$  and  $qSV(\psi)$ , and can be inverted from them. This theoretical assertion is inconvenient because, in general, it requires identifying the SV

arrivals in the data and separating them from SH-waves. Such an event identification and separation is especially problematic when the geophone azimuths are not measured independently, which is often the case.

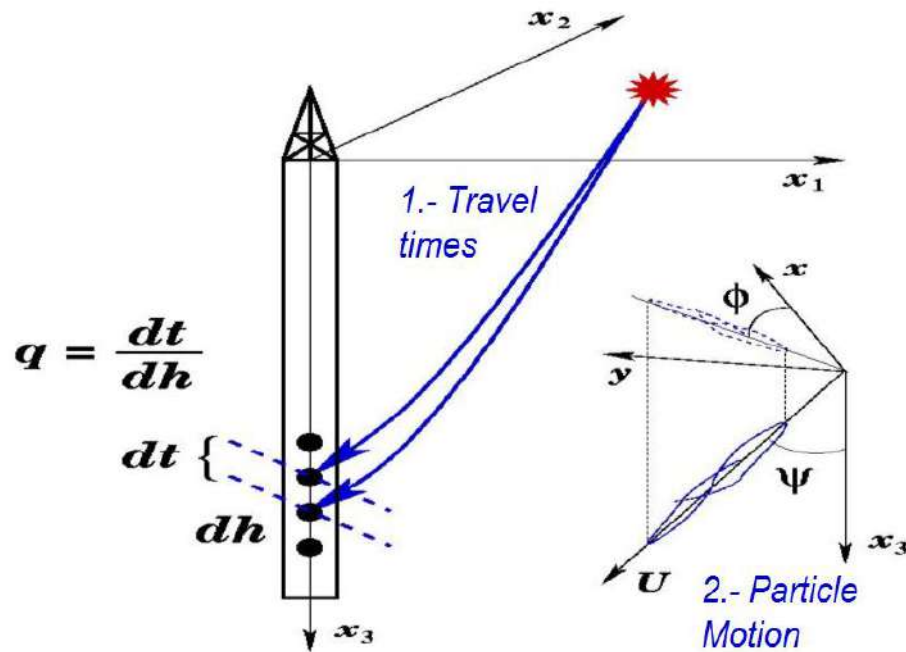


Figure 4-1. Measurements carried out for estimating anisotropy in a typical VSP geometry. The travel-time difference,  $dt$ , between geophones located at a distance  $dh$  along the wellbore defines the apparent slowness,  $q = dt/dh$ . Three-component traces recorded by each downhole geophone yield the direction of particle motion,  $U$ , or the polar polarization angle,  $\psi$ , and azimuth,  $\phi$ . Modified from Grechka and Mateeva (2007).

## 4.1 P-wave Slowness-Polarization Technique

### 4.1.1 VTI Media

To overcome the limitations of available slowness-polarization inversion techniques, Grechka and Mateeva (2007) proposed a method that can be carried out

utilizing the first arriving P-waves only. As no shear-wave information needs to be used, their method (1) works even in the presence of 3D velocity variations in the overburden and (2) can be applied to wide-azimuth VSP data to estimate azimuthal anisotropy.

Grechka and Mateeva (2007) found that the P-wave vertical slowness,  $q_p(\psi)$ , measured along a vertical borehole in VTI media has the form present in Equation 4-1:

$$q_p(\Psi) \approx \frac{\cos \Psi}{V_{P0}} (1 + \delta_{VSP} \sin^2 \Psi + \eta_{VSP} \sin^4 \Psi) \quad (4-1)$$

where “ $\approx$ ” denotes the weak-anisotropy approximation. The anisotropic coefficients  $\delta_{VSP}$  and  $\eta_{VSP}$  are expressed via the Thomsen coefficient  $\delta$  and the anellipticity coefficient  $\eta$  as follows:

$$\delta_{VSP} = (f_0 - 1) \delta \quad (4-2)$$

$$\eta_{VSP} = (2 f_0 - 1) \eta \quad (4-3)$$

The quantity  $f_0$  (shown in equation 4-4) in the above equations contains the ratio of the vertical P- and S-wave velocities,

$$f_0 = 1 / [1 - (V_{s0}/V_{p0})^2] \quad (4-4)$$

The only assumption in the Grechka and Mateeva (2007) method for a media is that the recorded waves are plane. To enter the inversion, each slowness-polarization pair has to satisfy different quality control procedures.

Equation 4-1 shows that the vertical slowness  $q_p$  written as a function of polar polarization angle  $\psi$  is influenced by  $V_{s0}$  in a nonessential way. As a consequence, the anisotropic dependence of  $q_p(\psi)$  is governed by just two quantities  $\delta_{VSP}$  and  $\eta_{VSP}$ , that absorb  $V_{s0}$ . While equation 4-1 establishes this result for weak anisotropy ( $|\delta| \ll 1$ ,  $|\eta| \ll 1$ ), the fact of three-parameter dependence  $q_p(V_{p0}, \delta_{VSP}, \eta_{VSP}; \psi)$  remains valid for strong anisotropy when equation 4-1 might lose its accuracy (Grechka and Mateeva, 2007). Thus, the introduced coefficients  $\delta_{VSP}$  and  $\eta_{VSP}$  are the appropriate parameters for describing the slowness-polarization behavior of P-wave VSP data acquired along vertical boreholes in VTI media.

The shear-wave velocity value might only be needed for converting the estimated  $\delta_{VSP}$  and  $\eta_{VSP}$  into Thomsen coefficients  $\delta$  and anellipticity coefficient  $\eta$ . This conversion, however, does not have to utilize VSP data. Instead, it can be done using  $V_{s0}$  obtained from sonic logs, check-shots, virtual shear check-shots (Bakulin et al., 2007), or any available empirical correlations.

#### 4.1.2 Orthorhombic Media

In contrast to the three quantities ( $V_{p0}$ ,  $\delta_{VSP}$ ,  $\eta_{VSP}$ ) that control the slowness-polarization dependence for P-waves recorded along vertical wells in VTI media, there are seven governing parameters for orthorhombic symmetry with a horizontal symmetry plane. These quantities are: the P-wave vertical velocity  $V_{p0}$ , two  $\delta_{VSP}$ -type coefficients, three coefficients analogous to  $\eta_{VSP}$ , and the azimuth  $\alpha$  of the vertical symmetry planes (Grechka and Mateeva, 2007).

$$\delta_{VSP}^i = (f_0 - 1)\delta^i \quad i = 1,2 \quad (4-5)$$

$$\eta_{VSP}^i = (2f_0 - 1)\eta^i \quad i = 1,2,3 \quad (4-6)$$

These  $\delta_{VSP}$  and  $\eta_{VSP}$  coefficients are shown in the weak-anisotropy approximation. To translate these coefficients into Tsvankin's (1997) parameters of orthorhombic media ( $\delta^{(1)}$ ,  $\delta^{(2)}$ ,  $\eta^{(1)}$ ,  $\eta^{(2)}$ , and  $\eta^{(3)}$ ), the ratio of the vertical velocities,  $V_{s0}/V_{p0}$ , is needed. As for the VTI inversion, this ratio is obtained from sonic logs or check shot.

$$q(\psi, \phi) \cong \frac{\cos \psi}{V_{p0}} \{1 + [\delta_{VSP}^{(1)} \sin^2(\phi - \alpha) + \delta_{VSP}^{(2)} \cos^2(\phi - \alpha)] \sin^2 \psi + [\eta_{VSP}^{(1)} \sin^2(\phi - \alpha) + \eta_{VSP}^{(2)} \cos^2(\phi - \alpha) - \eta_{VSP}^{(3)} \sin^2(\phi - \alpha) \cos^2(\phi - \alpha)] \sin^4 \psi\} \quad (4-7)$$

## 4.2 Anisotropic Parameter Estimation

A 9-component, 3D VSP dataset was acquired in Rulison Field in 2003 simultaneously with 3D surface seismic acquisition (see Figure 4-2a). A total of 708 sources spaced at 110 feet were recorded by downhole geophones at 19 depths with a spacing of 39.4 feet. The wide-azimuth Rulison survey contains offsets ranging between 60 to 7000 feet, and the orientations of the 3C geophones in the borehole have been estimated from the borehole seismic by Mattocks (2004) in a previous study. These acquisition features enable us to go beyond the standard assumption of vertical transverse isotropy and estimate the parameters of an anisotropic orthorhombic model.

The reservoir overburden is fairly simple at Rulison, (Figure 4-2b). The presence of regional faults (such as the one shown in the two-way traveltime in Figure 4-3b) makes the use of standard VSP methods, such as the slowness inversion techniques

(Gaiser, 1990; Dewanga and Grechka, 2003; Jilek et al., 2003), inappropriate due to lateral heterogeneity in the area. The discontinuity can also be observed in the one-wave traveltimes shown in Figure 4-3a.

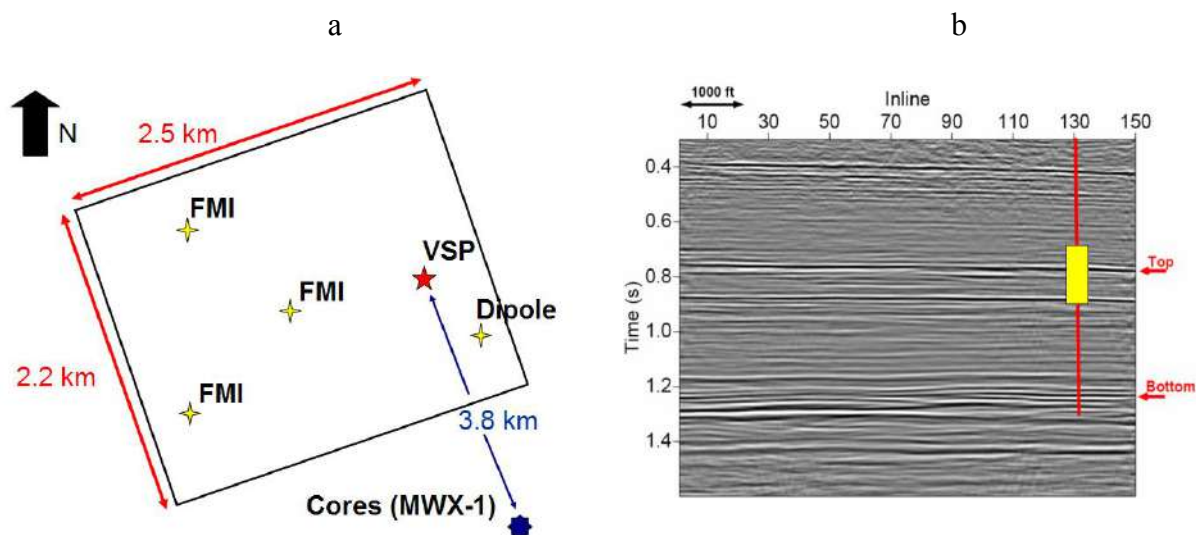


Figure 4-2. a) Plan view of the main wells with respect to the VSP (red star). b) The VSP dataset contains 19 geophones that cover the depth interval from 4,510 to 5,220 ft (yellow) and are shown on the background of seismic reflection data.

The data for the slowness-polarization inversion technique include the first-arrival times and particle-motion information of the P-waves. The plane recorded wave assumption can be verified through several quality control analyses, such as: (1) linearity of particle motion, (2) slowness vector consistent, and (3) accuracy of polarization angles. The  $V_p/V_s$  ratio can be estimated from sonic logs, check shots, or from the VSP data. Figure 4-4 shows a shot gather with the P-wave 3 component data recorded.

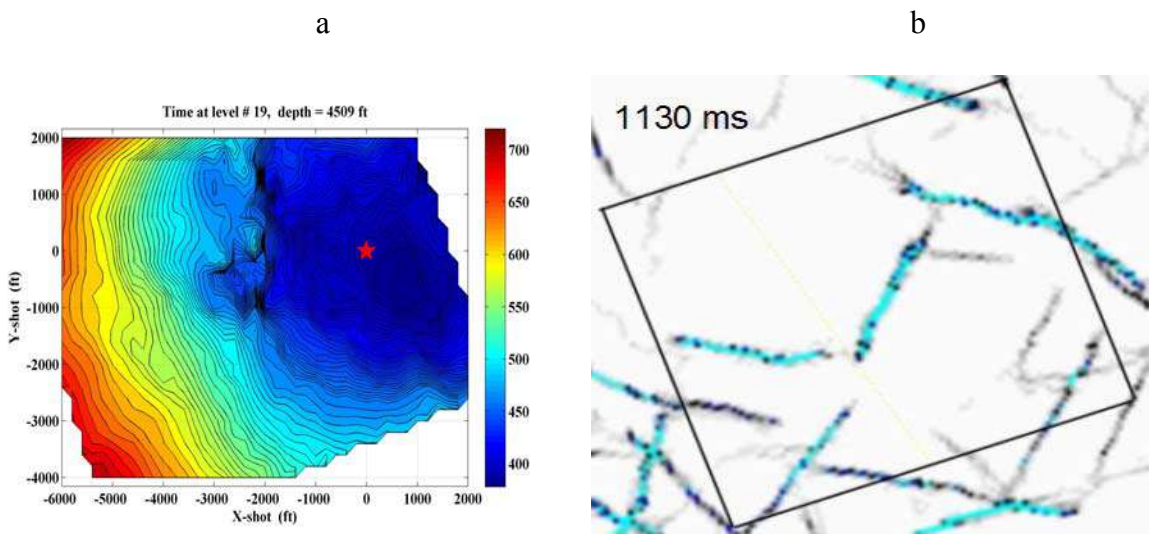


Figure 4-3. a) Travel time of the first arrival for the shallow receiver (depth 4509 feet) and b) Regional faults at 1130 ms (two-way travel time) from Jansen, 2005.

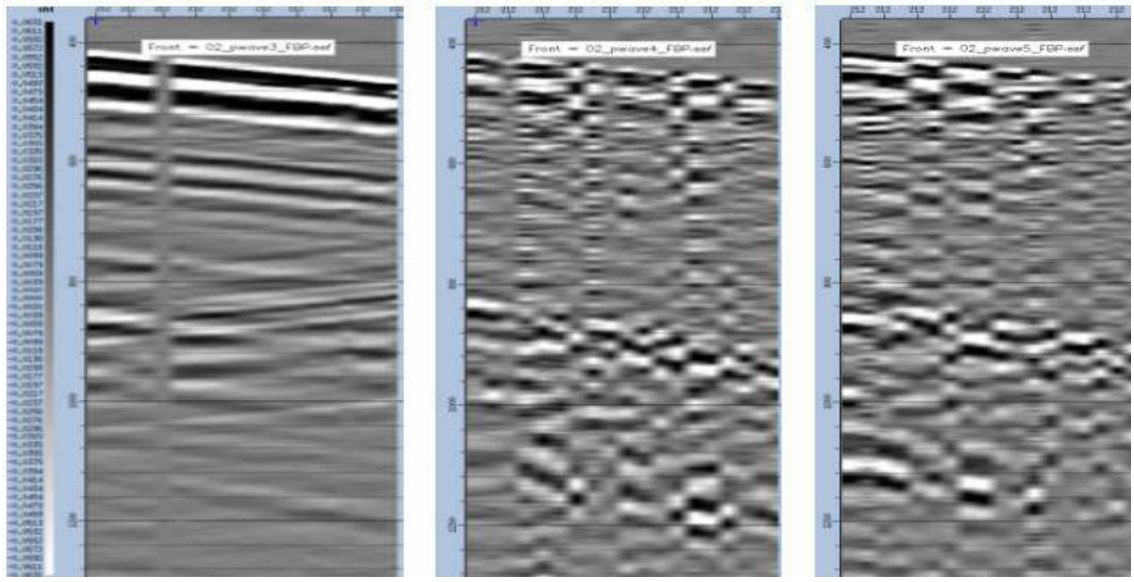


Figure 4-4. The first arrival times of P-waves and particle motion can be estimated in the three component VSP data. From left to right is shown the vertical component (Z), the horizontal component X and the horizontal component Y.

#### 4.2.1 VTI Inversion – Polar Anisotropy

The anisotropy parameters were estimated over a depth range of 400 ft (11 geophones), which is comparable with the wavelength recorded in the VSP. The slowness-polarization pairs allow estimation of the VTI parameters:  $V_{p0}$ ,  $\delta$ , and  $\eta$  at the VSP interval. While the anisotropic coefficients vary depending on the number of geophone levels (especially for highly heterogeneous intervals), the results are consistent for a width range window from 360 to 520 feet (10 to 14 geophones), giving confidence to the results produced by VTI inversion.

Table 4-1 shows the resulted for sandstone to shaley sandstone interval between 4690 to 4870 feet using different geophone levels. The results are consistent for different averaging windows. Under the VTI assumption, the overburden at Rulison Field could be characterized by the mean value  $\delta$  of 10%, the mean value of  $\eta$  of 7%, and the mean value of  $\epsilon$  of 19%.

Table 4-1. Anisotropy parameters for Rulison Field overburden (depth range 4690 to 4870 feet) in a sandstone to shaley sandstone interval.

<b>Depth (ft)</b>	<b>Lithology</b>	<b><math>\delta \pm 0.02</math></b>	<b><math>\eta \pm 0.01</math></b>	<b><math>\epsilon \pm 0.02</math></b>
4690 $\pm$ 180	Sandstones and Shaley sandstones	0.08	0.07	0.16
4710 $\pm$ 200		0.08	0.06	0.15
4730 $\pm$ 220		0.12	0.06	0.19
4750 $\pm$ 200		0.09	0.09	0.20
4770 $\pm$ 260		0.09	0.06	0.16
4790 $\pm$ 280		0.14	0.05	0.20
4830 $\pm$ 200		0.09	0.09	0.20
4870 $\pm$ 200		0.13	0.08	0.23
<b>Average</b>		0.10	0.07	0.19

The Rulison reservoir is composed of highly heterogeneous packages of sandstones, siltstones, shales and coals. Two typical sets of estimated  $V_{p0}$ ,  $\delta$ , and  $\eta$  that correspond to different depths and lithologies are shown in Figures 4-5a and 4-5b. Figure 4-5a gives an example of vertically homogeneous sandstone package, where the anisotropic coefficients are small (as expected). Figure 4-5b corresponds to a coal and shaley interval, which is fractured (shown by the shear wave splitting from cross-dipole). The anisotropic coefficients ( $\delta = -0.10 \pm 0.05$  and  $\eta = 0.14 \pm 0.01$ ) estimated below 4950 ft are affected by fractures at Price coal layer.

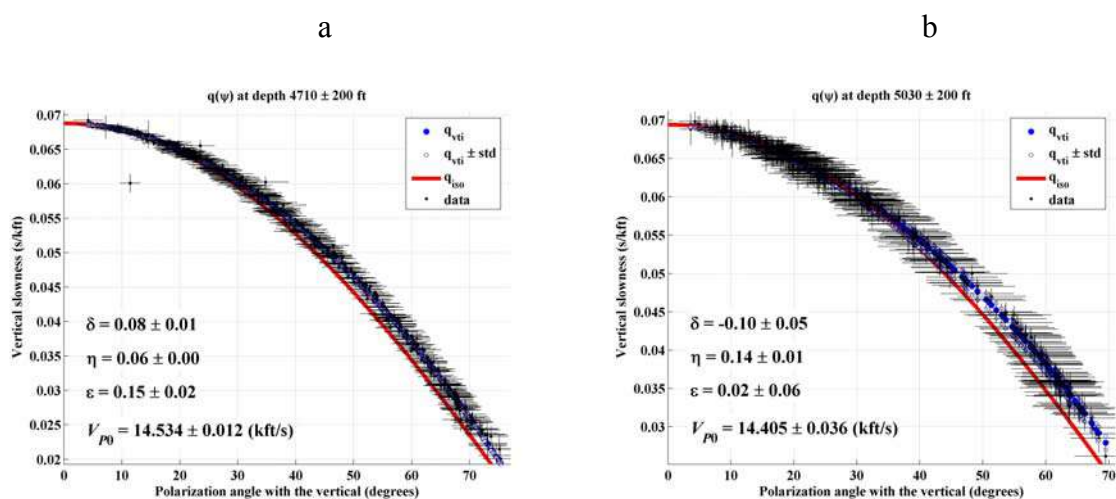


Figure 4-5. a) Anisotropic coefficients estimated from the upper 11 geophones and b) anisotropic coefficients estimate from the lower 11 geophones. Red line shows isotropic curve. Black dots are the data points (one dot for every shot gather use in the estimation) with their standard deviation. Blue dots are the best VTI fit to this dataset.

The Figure 4-6 shows the three parameters estimated from the VTI Inversion. At left is a P-wave vertical velocity profile. The values provide a useful quality control for the inversion, because it can be compared with a P-wave virtual check shot created from the VSP. A virtual check shot gather the wavefields from all the sources in each borehole receiver location to create a virtual shot gather (Bakulin et al., 2007). From this virtual

check shot gather the interval P-wave velocity could calculate between borehole receiver locations. Figure 4-6b displays the estimated  $\eta$  (red line) and  $\delta$  (blue line). The values of  $\eta$  are fairly stable through the VSP interval with the variation from 5 to 9% and the mean value of 8%. The coefficient  $\delta$  is more variable (ranging from 8 to 20%), its variation is related to the changes in lithology, such as sandstones at the top of the interval versus coal and shales at the bottom. Another factor in the variance of  $\delta$  is its dependence on polar angles less than  $25^\circ$  (see equation 4-1). In most of the inversion the amount of data below  $25^\circ$  was relative small and could not provide accurate estimations for all intervals.

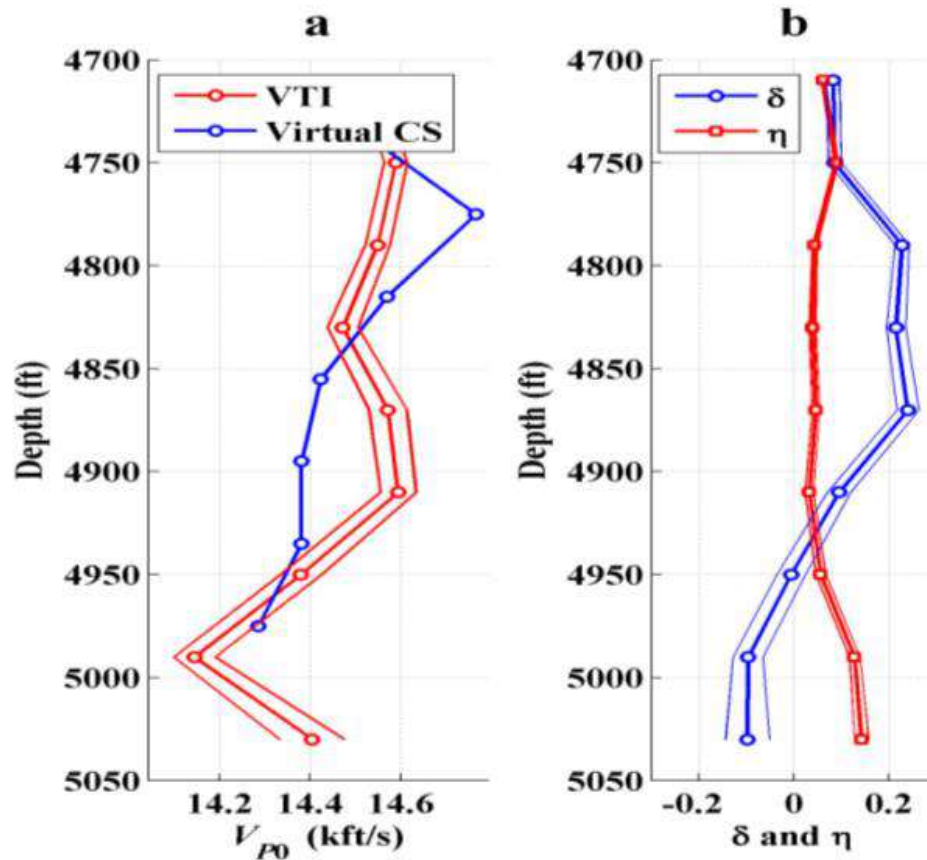


Figure 4-6. Depth profile at the VSP interval showing a) P-wave vertical velocity versus a virtual check shot and b)  $\eta$  and  $\delta$  anisotropy parameters.

Figure 4-7 shows a relation between the anisotropy parameters and gamma-ray log over the interval of interest. Lithologies vary in the VSP interval producing variations in the estimates. The coefficient  $\eta$  is stable for the sandstone and shaly sandstone interval (shallower 7 intervals). At the Price coal interval (deeper 2 intervals) there is an increase in  $\eta$  values produced by the fractured of the coal layer. Also it is important to note that the standard deviation of the anisotropy parameters estimated in the coal interval is higher than that in sandstone to shaly sandstone layers, which reduces the confidence in these estimates.

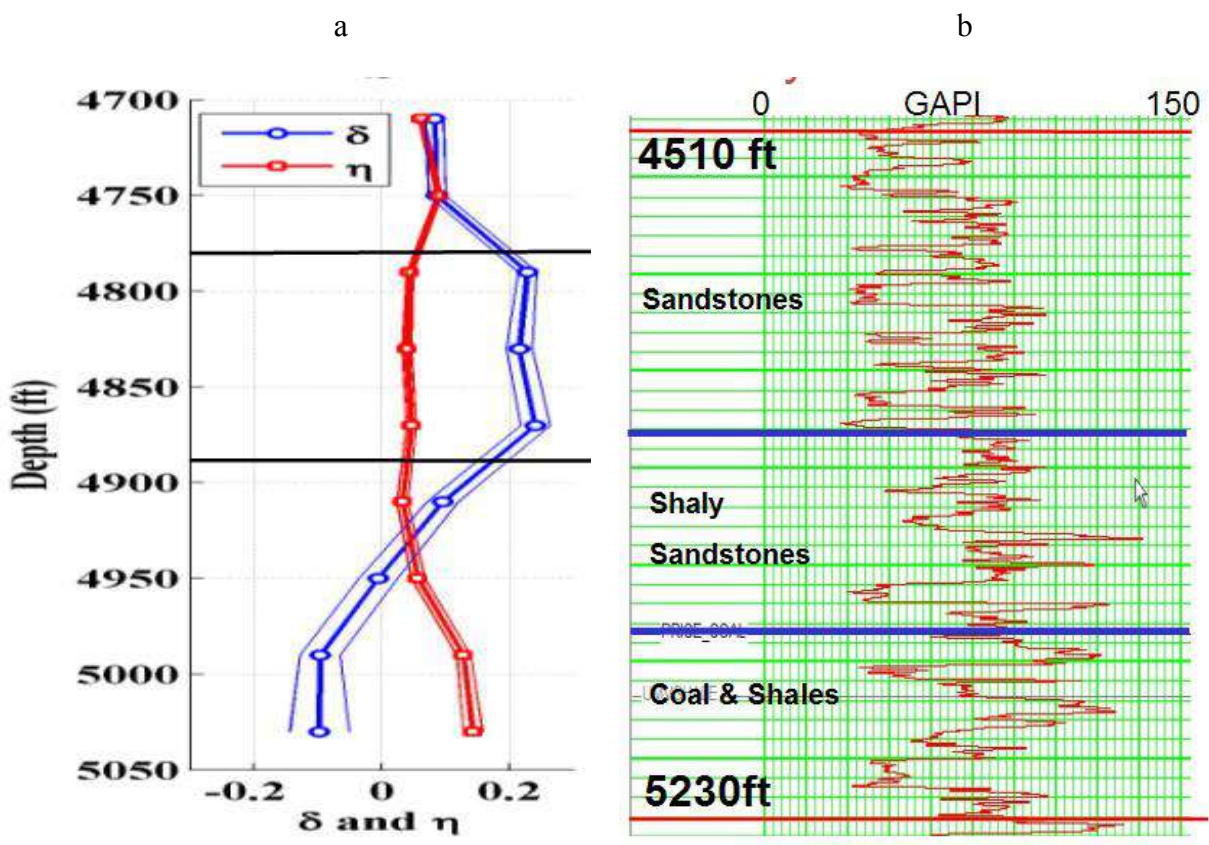


Figure 4-7. a) Depth profile using a window of 400 feet at the VSP interval and b) Gamma-ray log showing the lithology interpreted in the VSP interval.

#### 4.2.2 Orthorhombic Inversion – Azimuthal Anisotropy

In contrast to the three quantities ( $V_{p0}$ ,  $\delta$ ,  $\eta$ ) that control the slowness-polarization P-wave VSP data in VTI media ( $V_{s0}$  is obtained independently), there are seven governing parameters for orthorhombic symmetry. These quantities are: the P-wave vertical velocity  $V_{p0}$ ; two  $\delta$ -type coefficients  $\delta^{(1)}$  and  $\delta^{(2)}$ ; three anellipticity  $\eta$  coefficients  $\eta^{(1)}$ ,  $\eta^{(2)}$ , and  $\eta^{(3)}$ ; and the azimuth  $\alpha$  of the vertical symmetry plane  $X_1$ ,  $X_3$ .

Figures 4-8 and 4-9 show the apparent slownesses (corrected for the isotropic slowness-of-polarization dependence) that are extracted from the data and fit with an orthorhombic model for the same levels showed at Figures 4-5a and 4-5b. The azimuthal dependence of the VSP data displayed is clearly observed at near-vertical propagation (or at small horizontal components of the P-wave polarization) and becomes less obvious away from the vertical. As expected,  $\delta^{(1)} < \delta < \delta^{(2)}$  and  $\eta^{(2)} < \eta < \eta^{(1)}$  because the VTI parameters  $\delta$  and  $\eta$  (Figures 4-5a and 4-5b) average azimuthal anisotropy; the error in the orthorhombic quantities is greater than those in their VTI counterparts because more unknowns are estimated from the same amount of data. While the physical origin of the azimuthal anisotropy is not completely clear at this point, it is presumably related to fractures.

Figure 4-8 shows the azimuthal anisotropy at the overburden of Rulison field. The orthorhombic inversion identifies the north-south and east-west symmetry directions. The east-west direction correlates with the natural and induced fractures orientation at Rulison Field and suggests the fractures to be a likely cause of the azimuthal anisotropic detected in the overburden.

The azimuthal anisotropy associated with the VSP interval shows a constant orientation east-west and north-south. Figure 4-9 shows the results for the depth range 4830 – 5230 ft. The results here deviate from those in the upper and middle part of the

VSP interval. The standard deviations of the anisotropy parameters and the misfit increase and the azimuth of the vertical symmetry planes rotate from 0 to 45 degree. These measures are located in the Price Coal and UMV shale interval, that it is known from shear wave splitting measured in the cross-dipole RWF 332-21 log that is highly fractured with multiples crack sets. The change in azimuthal anisotropy to a northwest orientation is possibly related to: (1) a multiple sets of fractures with preferential orientation N45°W or (2) fewer input data produced a less accurate and bias estimated.

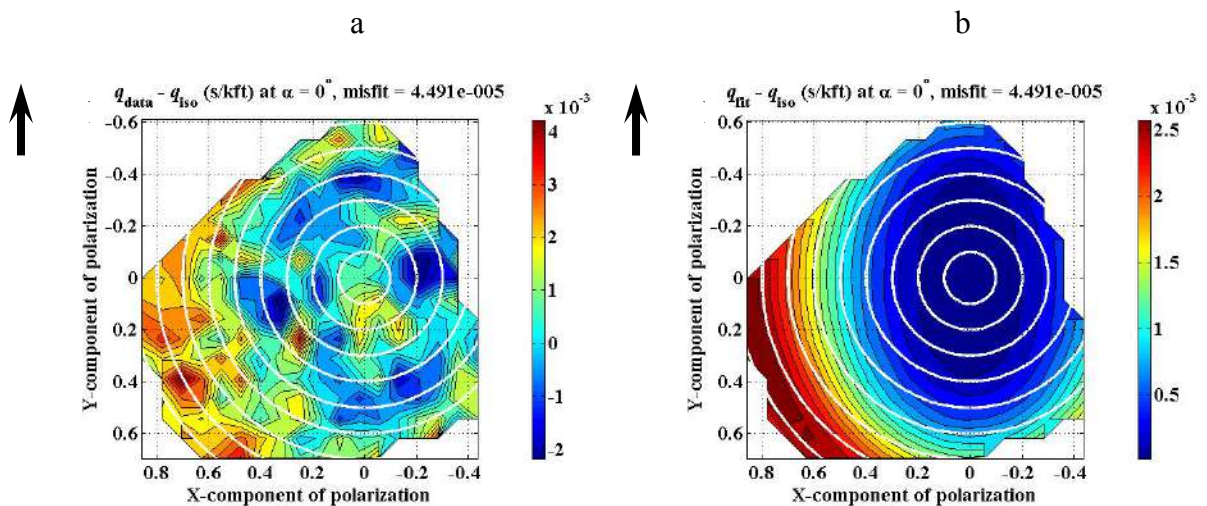


Figure 4-8. Azimuthal variations of the measured a) and fitted b) apparent slownesses (both are corrected for isotropy) as functions of the P-wave horizontal polarization components for the best-fit orthorhombic model in the depth range 4510 – 4910 ft. Model parameters and their standard deviations are:  $\alpha = 0^\circ \pm 5^\circ$ ,  $V_{p0} = 14.527 \pm 0.048$  kft/s,  $\delta^{(1)} = -0.01 \pm 0.06$ ,  $\delta^{(2)} = 0.12 \pm 0.05$ ,  $\eta^{(1)} = 0.07 \pm 0.03$ ,  $\eta^{(2)} = 0.04 \pm 0.02$ , and  $\eta^{(3)} = -0.02 \pm 0.03$ . Color scale shows the difference between the measure data and the isotropic model. White circles indicate the slowness variations expected in the absence of azimuthal anisotropy.

Wolhart et al. (2005) used microseismic data to show that the maximum stress direction could change with depth (e.g. from N87°W to N60°W in a 1200 ft interval). Higgins (2006) analyzed image and sonic logs in four different wells in Rulison Field.

She suggested that it is possible that the maximum horizontal stress direction changes with depth.

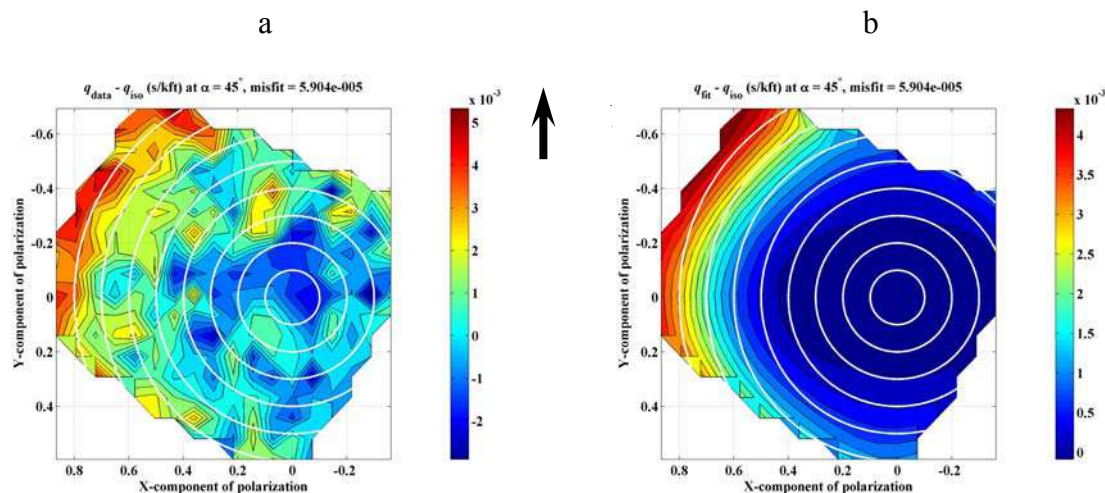


Figure 4-9. Azimuthal variations of the measured a) and fitted b) apparent slownesses (both are corrected for isotropy) as functions of the P-wave horizontal polarization components for the best-fit orthorhombic model in the depth range 4830 - 5230ft. Model parameters and their standard deviations are:  $\alpha = 45^\circ \pm 5^\circ$ ,  $V_{P0} = 14.44 \pm 0.05$  kft/s,  $\delta^{(1)} = 0.03 \pm 0.07$ ,  $\delta^{(2)} = -0.1 \pm 0.06$ ,  $\eta^{(1)} = 0.07 \pm 0.04$ ,  $\eta^{(2)} = 0.13 \pm 0.02$ , and  $\eta^{(3)} = -0.14 \pm 0.06$ . Color scale shows the difference between the measure data and the isotropic model. White circles indicate the slowness variations in the absence of azimuthal anisotropy.

#### 4.3 Correlation with Rock Physics Measurements and Cross-dipole Analysis

Figure 4-10a shows the estimation for  $\delta$  and  $\eta$  in a shaley sandstone core plug; the results are in a good agreement with the VSP inversion.  $\eta$  from core samples range from 2 to 10% and  $\delta$  values range from 2 to 14% at the reservoir confining pressures.

A cross dipole in the well RWF 332-21 was acquired close to the location of the VSP (2000 feet from the well) allowing the determination of the shear wave splitting at the overburden of the reservoir (see Chapter Three). Figure 4-10b shows that average

values of shear wave splitting were about 1.5 to 2% (black curve) and that there is an increase in the anisotropy and fracture density at the Price Coal interval (blue line). The azimuthal anisotropy at this interval is northwest oriented, as shown by the VSP azimuthal anisotropy (Figure 4-9)

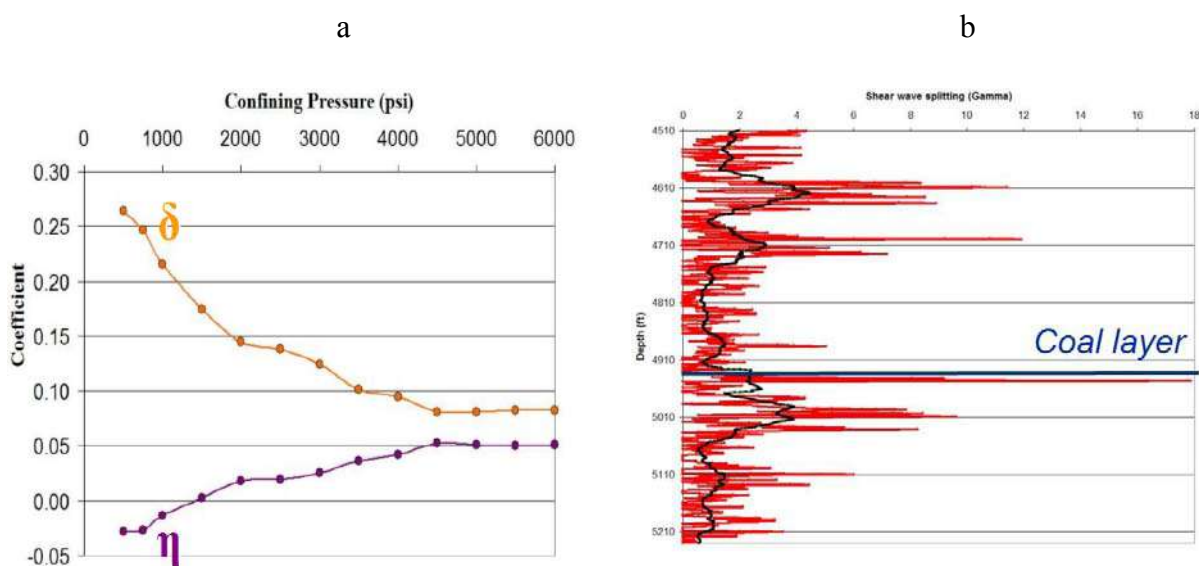


Figure 4-10. a) Anisotropy parameters  $\delta$  and  $\eta$  for a shaley sandstone core plug b) Shear wave splitting percentage at the overburden. Red trend indicates the shear wave splitting and the black line indicates an average shear wave splitting over 40 feet.

Figure 4-11 shows a 700 foot interval image log equivalent to the 2003 VSP interval for the Well RWF 441-20, located in the north central part of Rulison Field. As in the RWF 332-21, the area below the Price coal and within the UMV shale layer is heavily fractured (natural and induced fractured). These high-density fracture areas could be responsible for the drop in  $\delta$  from positive to negative values in the VSP Inversion.

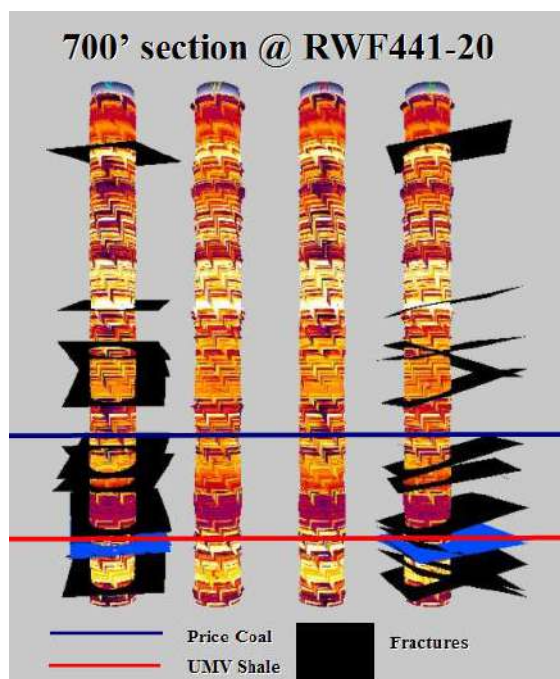


Figure 4-11. 700 foot interval from well RWF 441-20 equivalent to the 2003 VSP interval. Notice the high amount of fractures in the below price coal layer (blue line). From Halliburton (2006).

#### 4.4 Anisotropy Parameters to Improve Seismic Imaging

One of the main reasons for estimating  $\delta$  and  $\eta$  is that they might improve isotropic or conventional seismic imaging. At Rulison Field, the anisotropic seismic parameters estimated from the VSP provide the following conclusions:

1.- The mean  $\delta$  value of 0.1 produces a difference of 10% between  $V_{nmo}$  and  $V_{p0}$ . This difference implies a mis-tie between the real depth and the depth estimated from isotropically processed seismic data. In the seismic section at Rulison Field, this error is not observed because the processing is limited to time domain.

2.- The mean  $\eta$  value of 0.08 produces a difference of 8% between  $V_{\text{nmo}}$  and  $V_{\text{hor}}$ . This difference implies the under correction at far offsets (more than 2 times the target depth) in the time domain CMP gathers. In the poststack seismic section at Rulison Field, this error is not observed due to the muting of large offset ranges in the CMP gathers.

Future seismic processing at Rulison Field could benefit highly from anisotropy seismic processing, especially close to faults and dip areas.

Another important aspect is the change of anisotropy parameters with time and the feasibility of using them in time-lapse studies. Figure 4-12 shows the shear wave impedance volumes difference between the 2003 and 2004 survey (Rumon, 2006) at the crossline 76. VSP 2003 well (RMV 30-21) is shown with the zones of perforation. At the VSP Interval (from 4500 to 5200 ft), there are no observed time lapse changes in the shear-wave. This result suggests that the shear-waves remain constant during the time lapse study, and anisotropy parameters estimated from the 2003 VSP dataset are suitable to characterize the overburden in the 2003 and 2004 surveys.

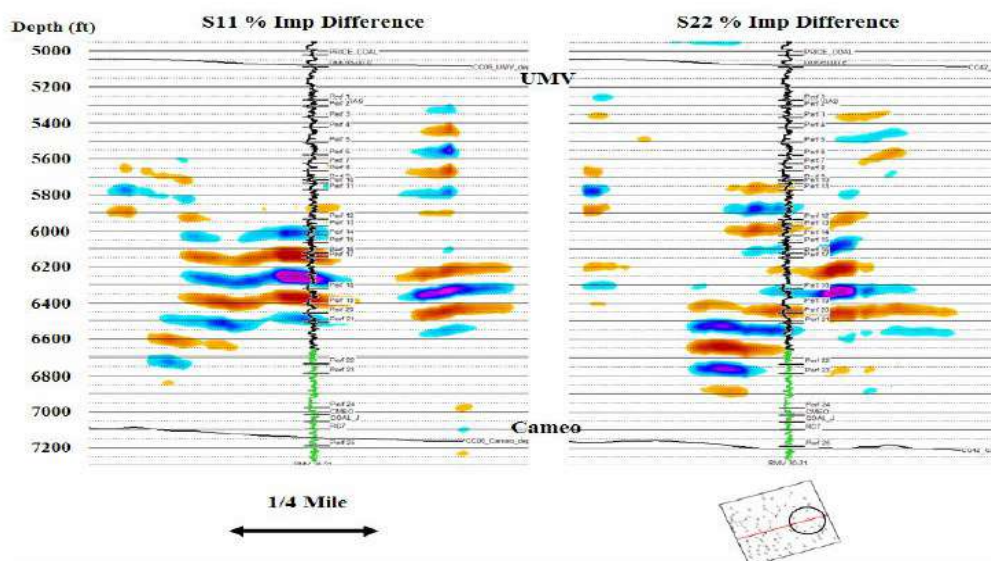


Figure 4-12. S11 and S22 percent impedance change around VSP location. Gamma ray log and well perforations are also displayed. From Rumon (2006).

## 4.5 Summary

Tight gas sandstones at Rulison Field, Colorado are anisotropic. Results from VTI and orthorhombic P-wave inversion show that the anisotropy parameters vary and correlate with lithology (sandstones, siltstones, coals, and shales) and are influenced by fractures (especially in the coal layers).

Azimuthal anisotropy is evident at small and medium offsets, with the principal orientations north-south and east-west and a secondary orientation north-west in the Price coal interval. This change in direction suggests that multiple sets of fractures might exist at Rulison Field, mainly in the coal layers.

The P-wave VSP inversion assuming a VTI symmetry, reveals that sandstones and shaley sandstones at the reservoir overburden of well RMW 30-21 have the mean value  $\delta$  of 10%, the mean value of  $\eta$  of 7%, and the mean value of  $\epsilon$  of 19%. These mean values can be used to produce an anisotropic seismic section.

Mattocks (2004) studies of shear wave VSP data suggested that the overburden in Rulison is close to orthorhombic. The results of the P-wave VSP inversion yield a similar conclusion, but further studies are needed to verify this result. For an orthorhombic symmetry, it can be estimated that  $\delta(1) < \delta < \delta(2)$  and  $\eta(2) < \eta < \eta(1)$ . These orthorhombic quantities also vary and correlate with lithology and fractures.

The VSP acquired in the summer of 2006, located at the reservoir level, provides a unique opportunity to improve the understanding of seismic anisotropy in the Rulison Field reservoir.

## CHAPTER 5

### ESTIMATION OF AZIMUTHAL ANISOTROPY USING P-WAVE SEISMIC

Tight gas sandstones are developed and produced by hydraulic fracturing of the production interval. To increase the gas flow, mixed fluids are pumped into the borehole at high pressure. Well completion produces artificial fractures and enhances the overall permeability of the zone. The ideal case is to identify the natural fracture systems in the reservoir and to enhance the natural permeability with the artificial fracture process.

Characterization of naturally fractured systems using surface seismic has been of interest in the oil and gas industry for a long time. The characterization of these systems can help to control the volume and flow direction of fluids and also provides economic interest to some unconventional reservoirs (such as tight gas sands). The knowledge of the fractures allows engineers to design trajectories of production and injection wells and to understand natural barriers or flow paths that will help to optimize the development of a field.

Azimuthal dependence of the seismic properties (traveltimes, amplitudes and velocities) on the fracture systems or azimuthal anisotropy can affect the properties of the P-waves. Shear wave splitting analysis is well known, and its main limitation lies in the acquisition and processing of multicomponent data. It is well known that to make a complete characterization of the fracture sets in a field, a nine component (9C) survey is needed, but due to the limited amount of surveys with these specifications, geoscientists rely on conventional P-wave data. A P-wave wide-azimuth survey is not capable of providing all the information needed, so additional data from a borehole is necessary to calibrate these results.

Previous work in this topic includes Lynn et al., (1995), Corrigan et al., (1996), Craft et al., (1997), Grechka and Tsvankin (1999), Bakulin et al., (2000), Gray et al., (2003). In the presence of azimuthal anisotropy, the data it is affected, and its influence during the analysis should be considered; thus, the seismic processor must correct this azimuthal anisotropy effect in order to improve the seismic imaging and the geological interpretation of the dataset.

A P-wave azimuthal anisotropy analysis was used to determine a qualitative estimate of fracture density and its correlation with production areas. At Rulison Field, two additional surface seismic studies have been conducted to characterize the azimuthal anisotropy: (1) an azimuthal AVO and full-scale azimuthal moveout analysis processing from Xiaoxia Xu (2006) and (2) a fracture characterization analysis for an orthorhombic model from Vasconcelos and Grechka (2006). Both studies provide valuable information about the characteristics of the reservoir and show the importance of accounting for azimuthal anisotropy in tight gas sands reservoirs.

## **5.1 Quality Control of Surface Seismic Data**

Quality control of seismic data and review of pre-stack processing workflows were done to obtain the best processing parameters for the azimuthal anisotropy analysis. Data analyses show several challenges, including:

1.- High noise level and low S/N ratio. Noise was introduced due to railroad traffic, highway I-70, and drilling operations.

2.- Low fold on the border of the survey areas and small full fold P-wave zone (Figure 5-1b). The northern extent of the survey includes steep slopes and cliffs that hampered seismic acquisition. The full fold P-wave area is limited to the middle of the survey.

3.- Statics corrections. Estimation of the statics became a difficult task due to the complexity of the weathering layer.

4.- Low P-wave reflectivity at the reservoir level. Between the top and bottom horizons (UMV shale and Cameo coal) it was difficult to detect additional horizons from P-wave seismic.

5.- RCP survey was optimized for shear wave acquisition and time-lapse repeatability processing.

Figure 5-1a shows the 2003 survey acquisition grid. The survey included approximately 1500 receiver and 700 source locations. The receiver grid azimuth was N26°E with the sources orthogonal to that orientation. Receiver inline spacing was 110 ft. and 330 ft. between lines. Source inline spacing was 110 ft. and 660 ft. between lines. P-wave sweep range was 6 Hz to 120 Hz. I/O VectorSeis Four single sensors digital multicomponent receivers were used as geophones. Subsurface bin size was 55 ft<sup>2</sup>.

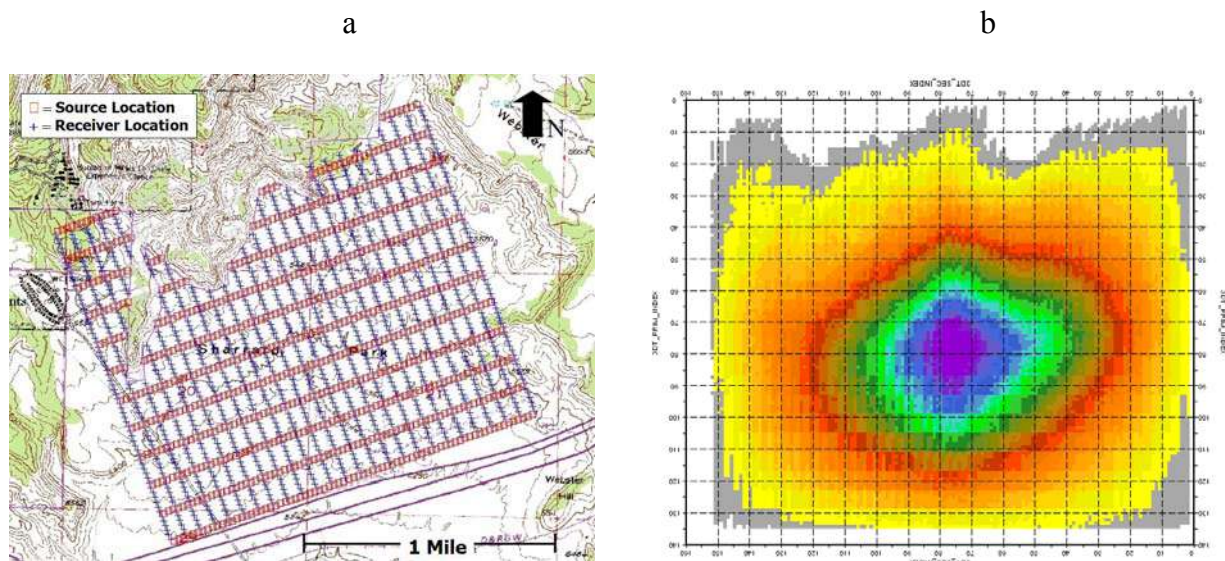


Figure 5-1. a) RCP's 2003 seismic acquisition design. Red squares represent P-wave sources (708 shots), and the blue crosses represent receiver locations (1500 geophones). b) Rulison 2003 survey fold map. Color scale represents the subsurface fold: 175 to 220 (purple), 110 to 175 (green and blue), 75 to 110 (red) and less than 20 (yellow).

It is important to estimate the vertical and lateral resolution of the surface seismic. The seismic frequency at the reservoir level for P-wave seismic is approximately 35 Hz and the P-wave velocity is approximately 13500 ft/s. Using these average values, the vertical resolution of the surface seismic was estimated as 100 ft using the equation 5-1 for obtaining the seismic wavelength and dividing the result by four (vertical tuning of the seismic wavelength).

$$\lambda = \frac{V_p}{\nu}, \quad (5-1)$$

where  $\lambda$  is the seismic wavelength,  $V_p$  is the P-wave velocity, and  $\nu$  is the seismic frequency.

Spatial resolution at the reservoir can be estimated with the Fresnel zone. Using the equation 5-2, the Fresnel zone was estimated as 1100 ft.

$$R_F = \frac{V_p}{2} \sqrt{\frac{t}{\nu}} \quad (5-2)$$

where  $R_F$  is the radii of the Fresnel zone,  $V_p$  is the P-wave velocity,  $\nu$  is the seismic frequency, and  $t$  is the two way travel time. The dominant frequency from a given area is governed by the physical properties of the subsurface and the quality of the seismic acquisition and processing.

## 5.2 Processing Sequence

The processing sequence to produce the azimuthal processing analysis started with the P-wave prestack gathers processed by Veritas. The processing sequence applied to the data at Veritas included:

1. Tilt correction for Vectorseis geophones applied in field
2. Demultiplex/Geometry/First Break Picks
3. Refraction tomography statics
4. Manual trace edits
5. Amplitude recovery using  $T^2$
6. Surface consistent deconvolution

From this stage the complete processing sequence to generate the azimuthal anisotropy analysis included preconditioning of the data (steps 7 to 11), splitting of the data into azimuth bins (steps 12 to 14) and azimuthal anisotropy analysis (steps 14 to 16):

7. Noise attenuation (see raw gathers in Figure 5-2a). Several processing flows were used to attenuate the high level of noise in the data.

8. Surface consistent amplitude correction
9. Reflection static corrections
10. Velocity Analysis (Preliminary)
11. First Break Mutes

12. Selection of the offset range. By limiting the range of offsets, the survey design azimuthal bias was highly reduced. The offset ranges were selected with an azimuth versus offset crossplot. Full azimuth coverage was achieved for a maximum offset of 5500 ft.

13. Selection of the data in azimuth bins (4 bins of 45 degrees each). Equation 5-3 involves three unknowns, so it is necessary to use at least three independent azimuths to obtain a unique solution to fracture orientation and density.

14. Kirchoff pre-stack migration (KPSTM) for every bin. After PSTM, the dip-effect on the velocities was minimized, and diffraction hyperbolae were collapsed. The result were four azimuth limited volumes migrated with the same velocity field.

15. High density interval velocity picking. A high density velocity (one for every CMP) analysis was made to detect the small azimuthal variations.

16. Azimuthal anisotropy analysis in velocities. There were four main steps: (1) stacking of every azimuth bin, (2) RMS velocity to Interval velocity conversion for every azimuth bin, (3) fractograms generation, and (4) fractograms interpretation.

### 5.3 Azimuthal Anisotropy Analysis in P-wave Data using Fractograms

Seismic anisotropy is defined as the dependence of physical properties (as seismic velocities) on the direction of wave propagation or angle (azimuth). Fractures that are aligned can produce azimuthal anisotropy and the differences in the seismic properties can be detected in the surface seismic.

The processing sequence applied includes WesternGeco flows that are based in P-wave NMO ellipses analysis. The orientation and eccentricity of the ellipse reflect the fracture directions and magnitudes in the subsurface. The P-wave velocity variations are fitted at each time sample to the ellipse equation 5-3:

$$f(\phi) = A + B \cos(2(\phi - \phi_0)) \quad (5-3)$$

where:  $\phi$  is the source to receiver azimuth,

$\phi_0$  is the orientation of major axis of ellipse,

A is the average value of the property, and

B is the modulus value or ellipticity

The results for the computations of the ellipses are stored in different 3D volumes (interval velocity, amplitude modulus, fracture orientation, apparent percentage of anisotropy and RMS fit error) called fractograms.

The work flow includes the analysis of certain attributes to select the optimum offset range, which will then be migrated for all the azimuths bins and the different azimuth volumes to subdivide the data. In our specific case, four volumes of 45 degrees azimuth each were selected. Then the pre-stack time migration (Figure 5-2b) of each individual azimuth bin was processed, using a migration velocity field. After the prestack processing and migration, a high density velocity analysis was produced and interpreted using data from each of the volumes independently. These interval velocity volumes were fitted to the NMO ellipse equation to obtain the velocity fractograms.

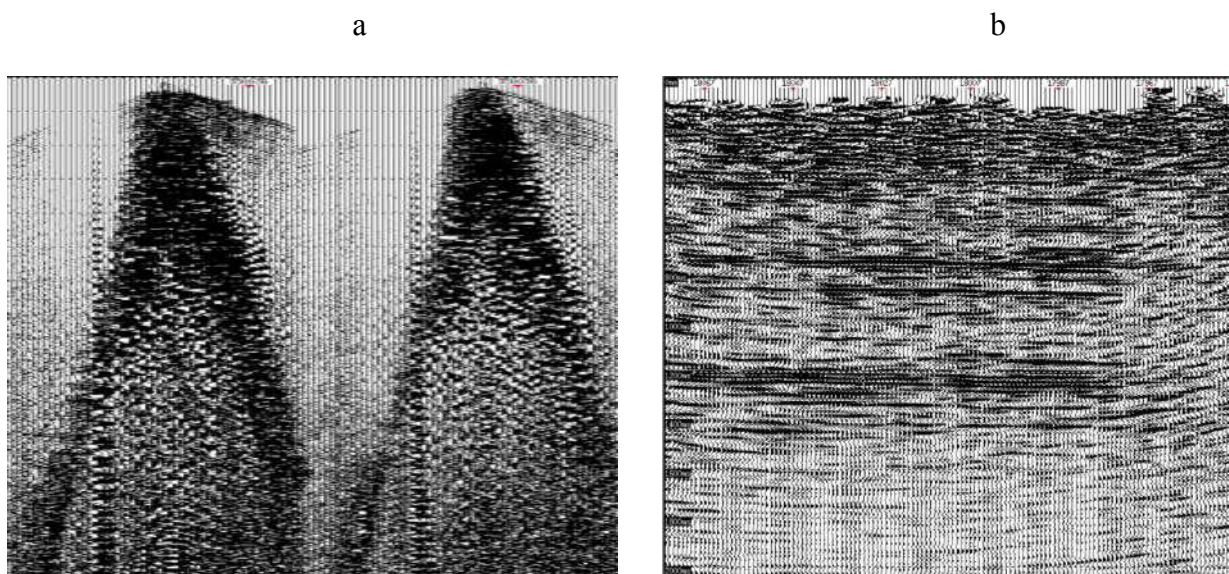


Figure 5-2. a) Areal gathers before noise attenuation processing. b) Kirchoff Prestack Time Migration (KPSTM) image from one of the four bins (azimuth 45 to 90).

The fractograms included were:

- 1.-  $A$  or mean fit amplitude, which represents the mean interval velocity of least square error fit as a function of time,
- 2.-  $B$  or modulus, which represents the magnitude of modulation in interval velocity as a function of azimuth,
- 3.-  $\phi$  or fracture orientation, which represents the orientation of the major axis of the ellipse as a function of time,
- 4.- RMS error or least square error fit, and
- 5.- Apparent percentage of anisotropy.

The volume of percent anisotropy is defined by the eccentricity of the NMO ellipse:

$$\text{Percent anisotropy} = \frac{2B}{A + B} * 100 \quad (5-4)$$

Percent anisotropy volume indicates areas with high azimuthal anisotropy. In areas where there are fractures, there is an azimuthal dependent behavior of the amplitude and velocity; therefore, a relative high percentage of anisotropy may be present. The RMS error volume may indicate the validity of the results. If an RMS error value is significantly smaller than a corresponding interval velocity modulus value, the measured anisotropy is likely to be real. One important step in the interpretation is the calibration and corroboration of the fractogram results with borehole measurements. Also, faults and stress mechanisms need to be interpreted to understand the fracture systems.

## 5.4 Azimuthal Anisotropy Results

Four main horizons were interpreted at different intervals. The horizons include: (1) Top of MSRVD, (2) Top of UMV shale, (3) Top of Cameo, and (4) Top of Coal D.

Figure 5-3 shows the percent anisotropy maps at UMV shale and Cameo Coal horizons. Blue colors indicate low or non-existent azimuthal anisotropy areas, and white and red colors indicate high azimuthal anisotropy areas. It is important to understand that in the case where multiple fracture sets exist, that two or more directions of high open fracture density will cause the P-wave azimuthal anisotropy to approach zero. UMV shale shows fractures at the west and northeast side of the RCP survey. Cameo Coal is more fractured in the entire horizon except the middle area. It is possible that in the Cameo coal middle area there is more depletion and fracture closure.

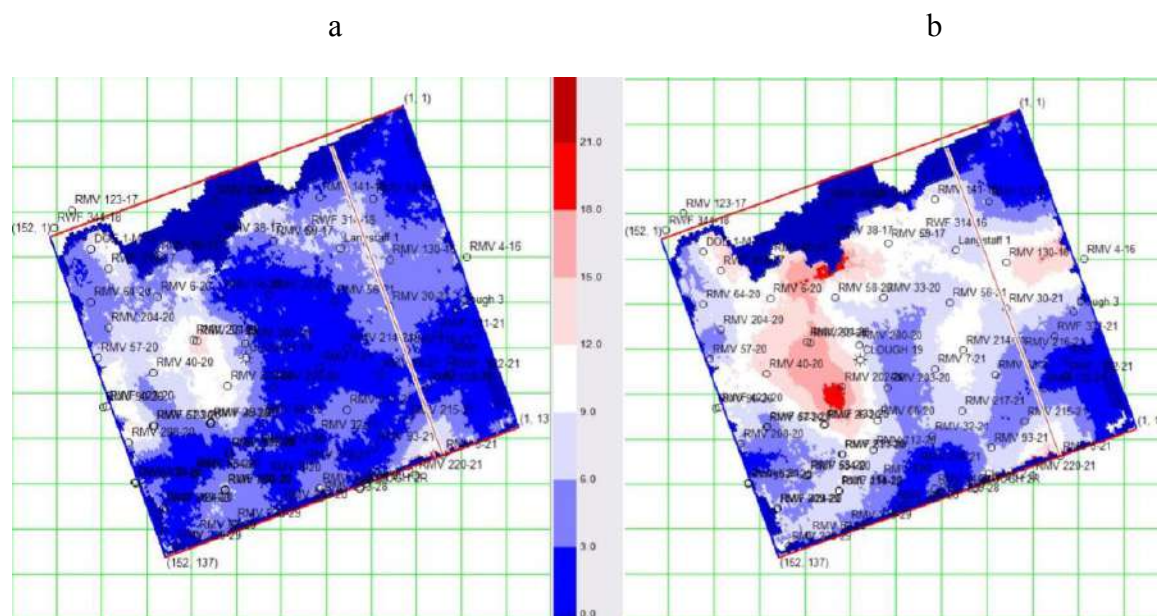


Figure 5-3. Percent of anisotropy for a) UMV shale (reservoir's overburden) and b) Cameo Coal. The blue color indicates areas of small azimuthal anisotropy, and the white and red colors indicate areas of high azimuthal anisotropy.

Cameo Coal zone consists of several coal intervals ranging from 30 ft. to 100 ft. in thickness (Cumella et al., 1992). Olson (2003) suggested that coals are mechanically weak and deform in a brittle manner. The permeability in the Cameo coal is 10 times higher than the reservoir sandstones and highly variable. This suggests that the coals are intensively fractured by the wrench fault system, and this was verified with the shear wave splitting analysis (Chapter Three).

Jansen (2005) suggested that at the middle of the reservoir (1010 ms two way time), one can see only smaller fault fragments. He suggested that the northwest trending faults are controlled by the larger continuous faults below the reservoir. Also, he suggested the existence of northeast stepovers that create fault intersections, enhancing the possibilities of fractures.

UMV shale (890 ms) shows a significant decrease in faulting and azimuthal anisotropy. The reason for this can be linked to the ductile properties of the shale that reduce the amount of fractures in the interval. Another important characteristic at Rulison Field is that the fractures are located mainly in sandstone and coal intervals (see chapter Three).

The percentage of azimuthal anisotropy or interval NMO ellipse maps from UMV shale and Cameo Coal (main reservoir area) is shown in Figure 5-4. The color scale at the right indicates the percentage of azimuthal anisotropy (eccentricity of the interval NMO ellipses). The Estimated Ultimate Recovery (EUR) from wells in BCF is overlapped and the legend is at the left bottom side of the figure. There is a poor correlation between EUR and P-wave azimuthal anisotropy analysis. The causes of a poor correlation in Rulison Field are explained in more detail in section 5.6.

Figure 5-4 shows an anomaly of more than 11% of percentage of azimuthal anisotropy at the west central area of Rulison Field. This high azimuthal anisotropy anomaly was also detected by Lynn et al. (1999) in a previous study at Rulison Field using the 1996 DOE seismic survey. This anomaly correlates with an uplift block

boundary by faults below Cameo coal. This anomaly also suggested a high fracture area close to these faults. It is important to notice that the EUR of the wells around the anomaly is higher than 1.5 BCF, correlating with the expected higher production around fracture areas.

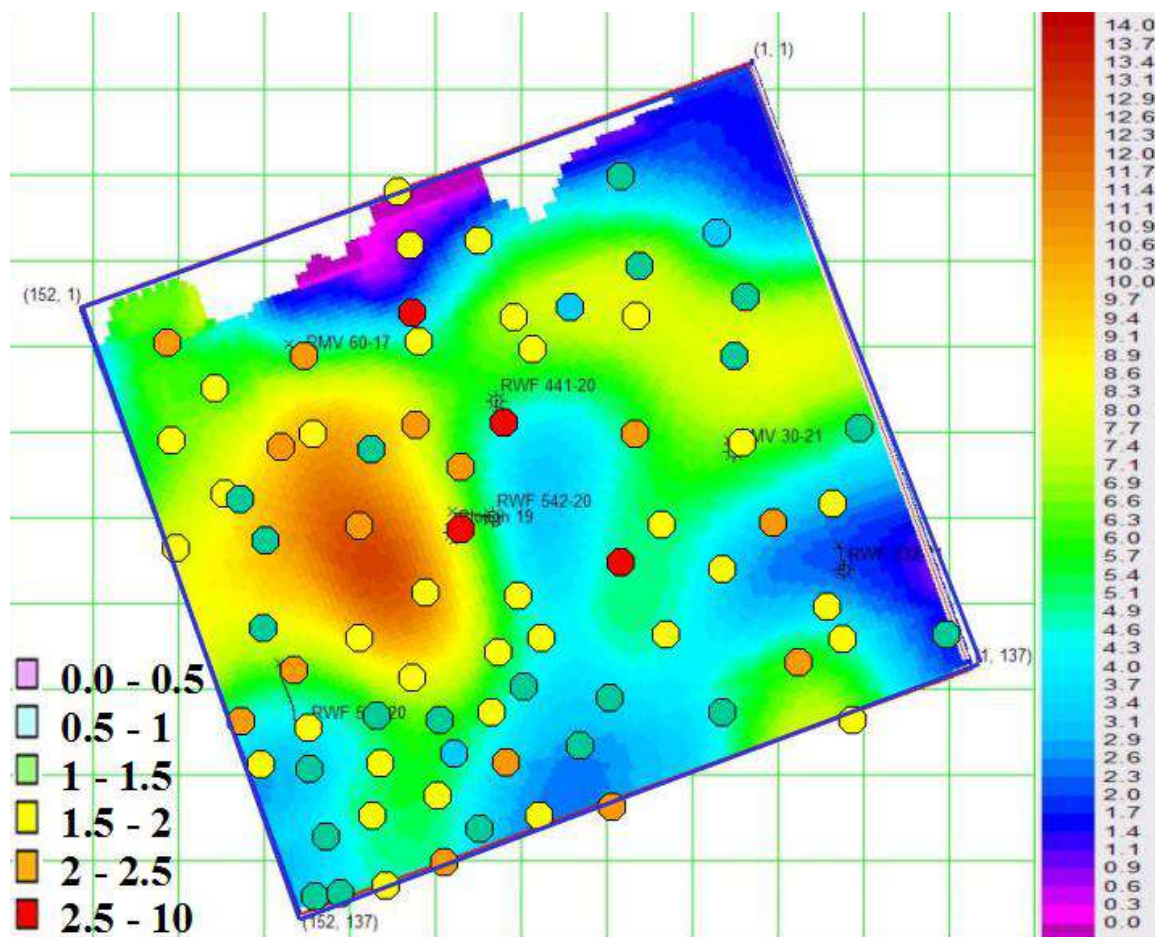


Figure 5-4. Percent of azimuthal anisotropy from UMV shale to Cameo coal including the production of the wells (legend at left bottom side are EUR quantities in BCF).

The quality of the NMO ellipses fits or RMS error is shown in Figure 5-5b. This error is being compared with the modulus value or ellipticity (Figure 5-5a). In the case

that the error is much less than the modulus, the fracture density estimation can be made with confidence. Only two areas of poor correlation can be identified: one at the southeast corner and another at the north central area.

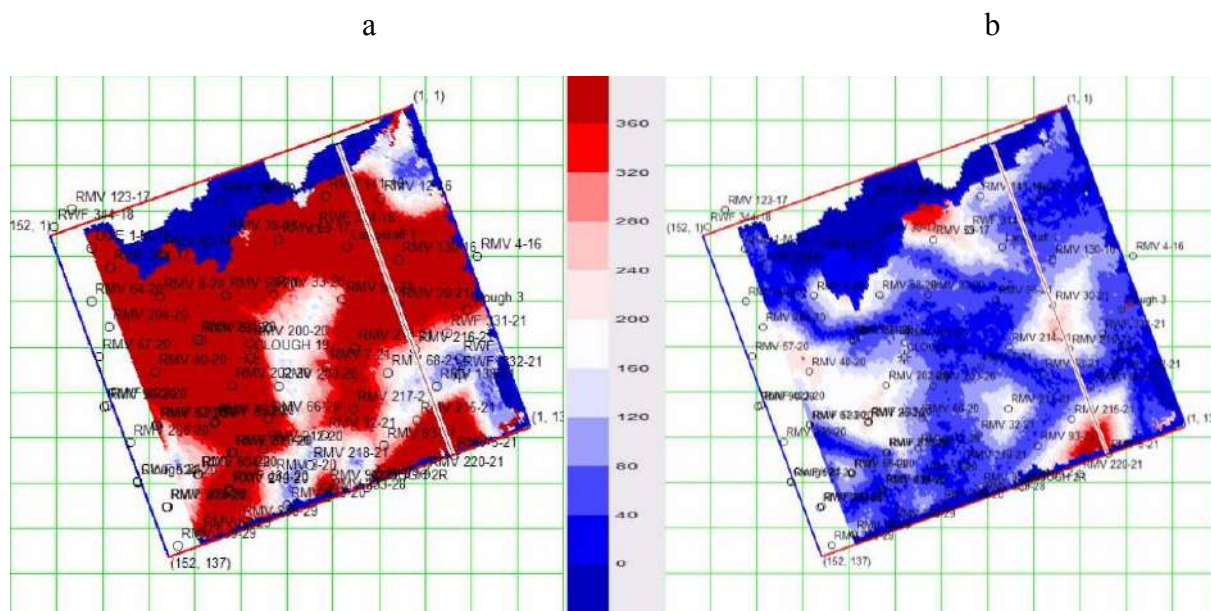


Figure 5-5. Fractogram from UMV to Cameo Coal for a) Modulus and b) RMS Error.

Figure 5-6a shows the average orientation fractogram at Cameo coal interval. Figure 5-6b shows the natural fracture orientation obtain from well logs (created from Matesic, 2007). Figure 5-7 shows a histogram of the orientation distribution before calibration of the surface seismic with the well logs. Using this information and the fracture orientation information from well logs, the orientation of fracture maps was calibrated shifting the orientation obtained with the surface seismic to the orientation from the well logs.

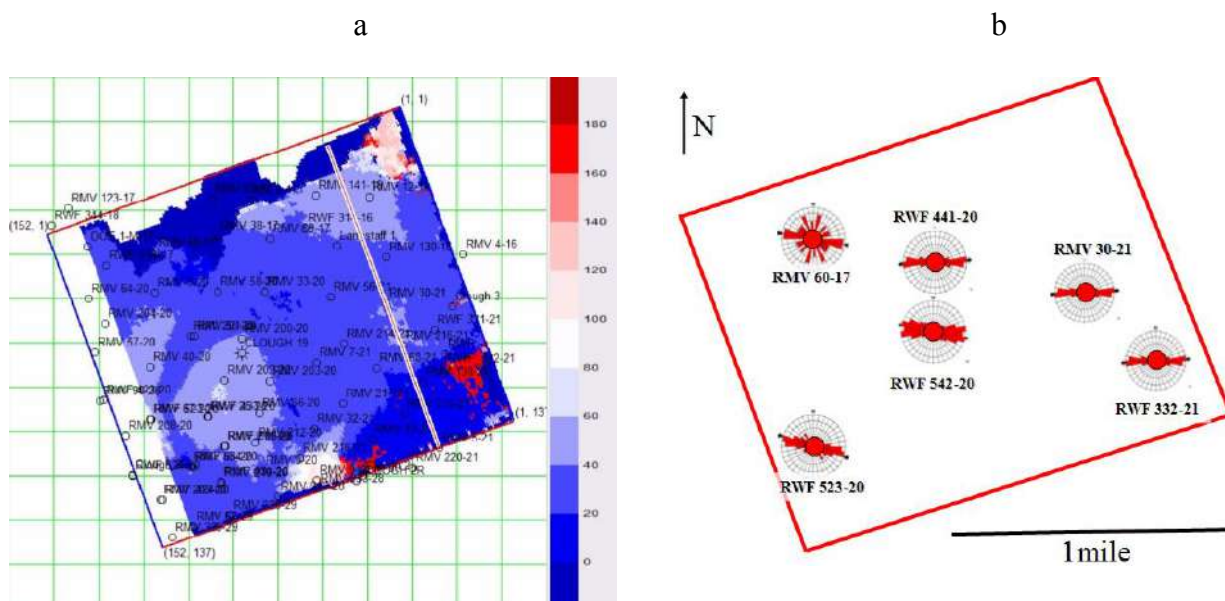


Figure 5-6. a) Fractogram showing the average orientation of the fractures at Cameo coal level. b) Natural fracture orientation for the main wells at Rulison Field. Created from Matesic (2007).

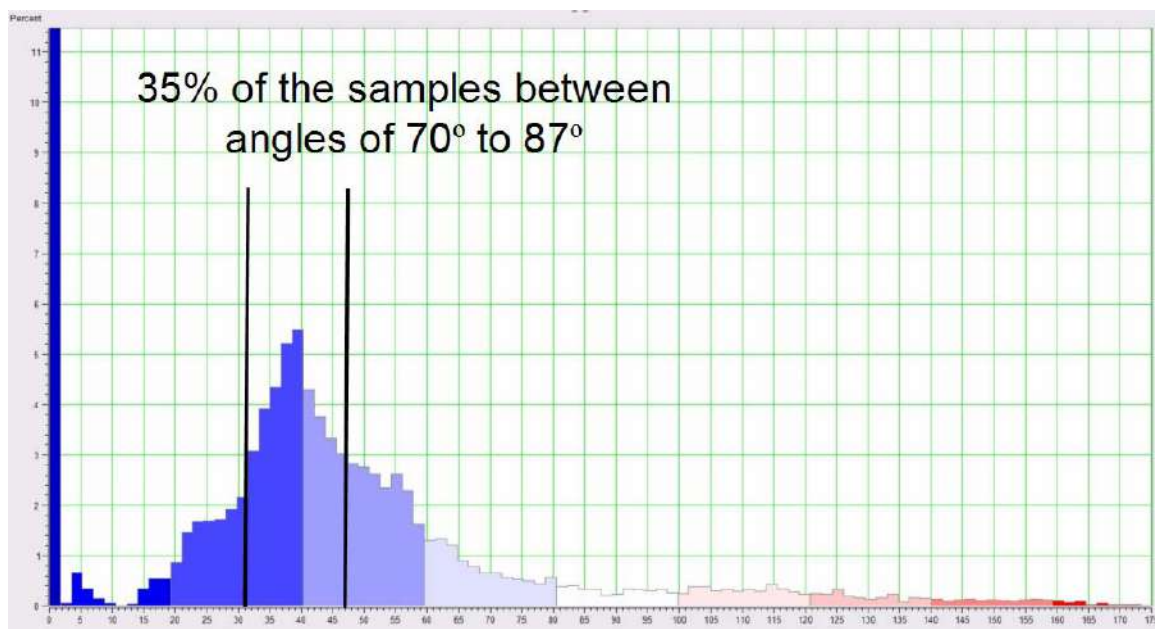


Figure 5.7 Histogram showing the angles distribution before calibrated with the well logs orientation.

An example of the calibration can be seen at the location of the wells RWF 542-20 and RWF 332-21 with an orientation of 50 and 0 degrees in the azimuthal anisotropy map. The orientation from the crossdipoles has a preference orientation of 90 and 40 degrees respectively at this interval, giving an average shift of +40 degrees from original surface seismic to calibrated surface seismic. After calibrating the orientation, a preference direction from 70 to 85 degrees was found. This direction agrees with the orientation of natural and induced fractures at Rulison Field.

#### **5.4.1 Azimuthal Anisotropy Percentage Sections**

Figure 5-8 shows two sections of the percent anisotropy volume. Figure 5-8a corresponds to the Inline 33, where the 2003 VSP (indicated in yellow) is located. The anisotropy estimation from the VSP shows  $\delta$  and  $\eta$  values that correlate with the lithology (sandstone and shaley sandstone). The deeper part of the VSP below the UMV shale shows an increase in the anisotropy probably related with fractures in this interval. This increase also correlates with increases in the percent azimuthal anisotropy volume from 3 to 6%. Figure 5-8b shows the location of one of the main producing areas in the field, where it can be observed that at the producing interval there are values between 6 to 10%. In both sections, an increase in fracture density in the coal areas could be observed.

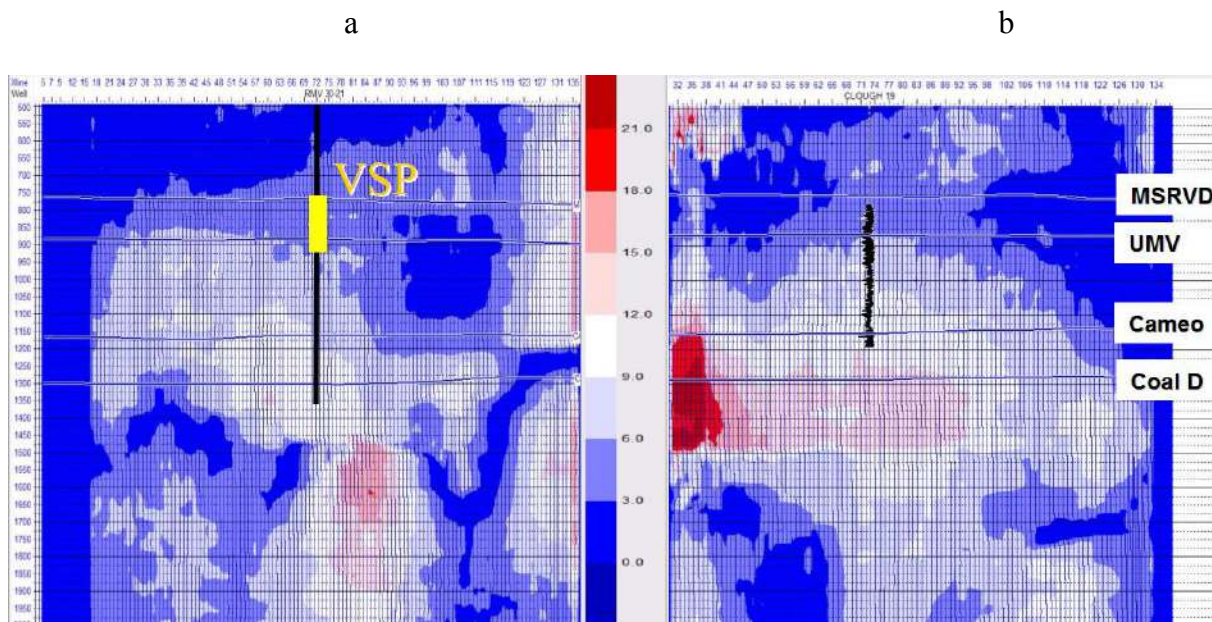


Figure 5-8. Percent anisotropy volume for different seismic sections a) Inline 33 with the location of the VSP (yellow rectangle) and b) Inline 95 with the location of one of the main well producers. Y axis are the two-way travel time and X axis is the inline or crossline number. Color scale indicated the amount of azimuthal anisotropy or eccentricity.

Figure 5-9 shows an azimuthal anisotropy section of the crossline 52. The shallow zone (above UMV shale) has small azimuthal anisotropy values (less than 4%); this suggested that the overburden of the reservoir is not fracture. The reservoir interval (between UMV shale and Cameo coal) shows an increase of the azimuthal anisotropy at the west side of the reservoir. This increase could be related with: (1) several faults that create a compartments within the reservoir (suggested position show in white lines); (2) higher density of wells that produced a higher number of induced fractures and (3) presence of different fracture sets orientations at the east side of the reservoir (Vasconcelos and Grechka, 2006) than could not be detected by P-wave studies.

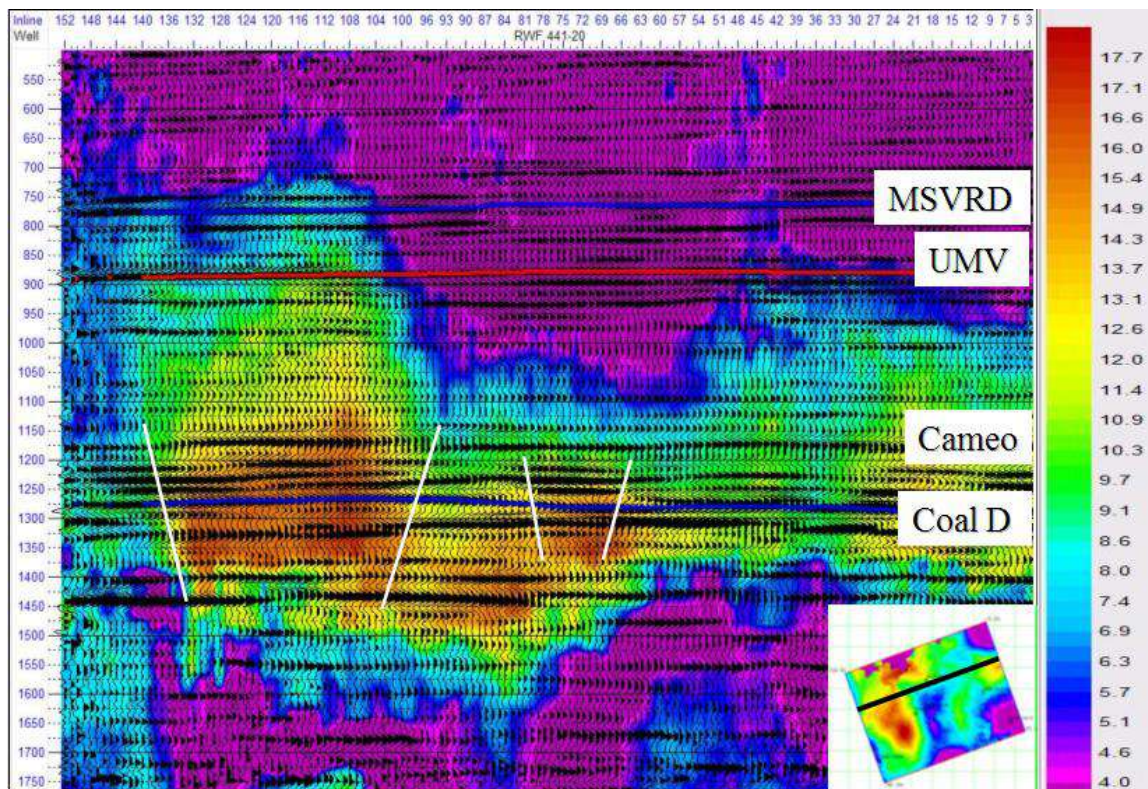


Figure 5-9. Percent azimuthal anisotropy section at crossline 52. Seismic traces are overlapping the volume and the main horizons are indicated at the right side. Purple colors indicate values with less than 4% of azimuthal anisotropy and hot colors represent areas of high azimuthal anisotropy. The white lines indicate suggests compartments below the Cameo coal layer. West side is at the left of the section.

The deep zone (below Cameo coal) have high values of azimuthal anisotropy (more than 10%), this correlates with the well logs and shear wave splitting analysis (Chapter Three) that showed that coal zone layers are highly fractured. The areas of high azimuthal anisotropy correlates with compartments create by faults below Cameo coal. These faults have been observed by other authors (Jansen, 2005 and Jackson, 2007) using P-wave seismic data (see Figure 5-14).

Figure 5-10 shows cross-line 72 for two different datasets. Figure 5-10a shows a cross correlation time shift for the  $S_{22}$  volume between the 2003 (base) and 2004 (monitor) survey (from Rumon, 2006). In the middle of the section, there is a negative value (close to 9 ms) that indicates a velocity decrease in the 10 month period between surveys. Figure 5-10b shows the azimuthal anisotropy percentage for the same cross-line using the 2003 P-wave survey. In the middle of the section, there is a small azimuthal anisotropy value (less than 5%). In both cases, the anomaly area is significant, and one explanation that can be suggested for this similarity is a fault area that (1) generates small azimuthal anisotropy in the P-wave due to the presence of multiple fracture sets or complicated structural features and, (2) generates negative values in  $S_{22}$  between the time shifts due to the lack of correlation in the fault area. In both sections, a possible compartment within the reservoir is shown.

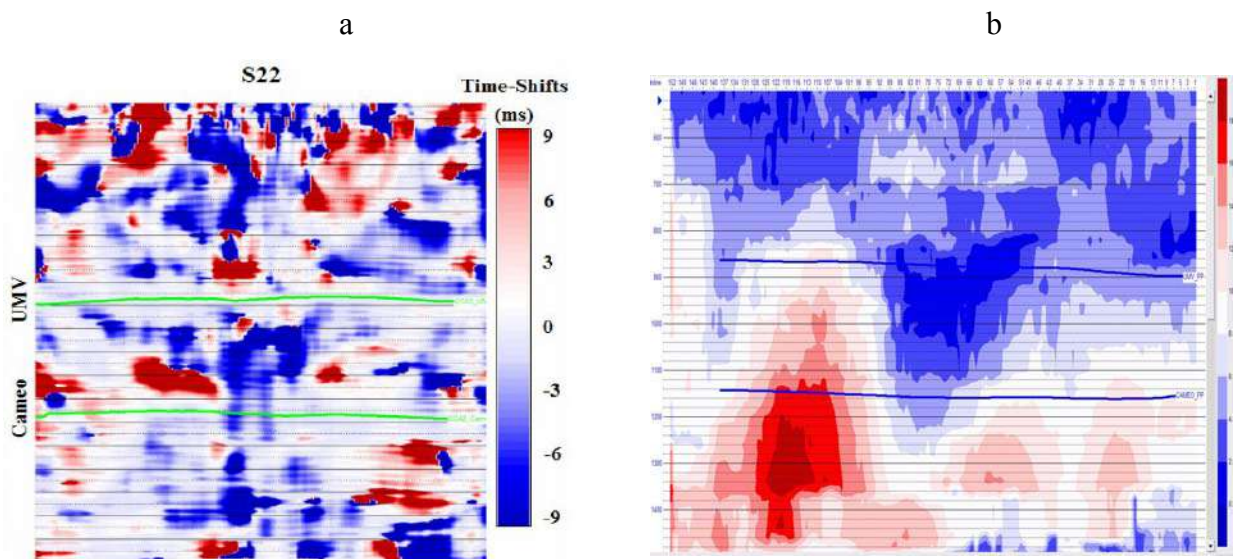


Figure 5-10. Xline 72 is displayed. a) Cross correlation time-shift for the  $S_{22}$  volume between the 2003 and 2004 survey. Negative values (blue colors) indicate a pull up or velocity decrease from 2003 to 2004 survey. From Rumon (2006) b) Azimuthal anisotropy volume with blue values indicating low azimuthal anisotropy in the 2003 survey.

## 5.5 Correlation between Azimuthal Anisotropy Zones and Production Areas

A correlation between the P-wave azimuthal anisotropy (as shown in other studies in the survey area) and production areas is difficult at Rulison Field due to the general lack of zonal production tests.

- 1.- Every well includes all the perforation zones with production co-mingled.
- 2.- New and old wells are mixed in the same period of time. New wells will have a higher production than old wells, and this affects the interpretation of results.
- 3.- Wells were completed with different techniques. Recent wells have the advantage of improved fracturing techniques compare to old wells.

A cumulative gas production map for a 10 month period after the 2003 survey was produced by Keighley (2006). A relatively consistent rate of between 55 and 105 MMCF in new wells is presented. There are a few higher productivity wells in the southeast corner of the survey area. The south west quadrant shows high well production from 155 to 255 MMCF. The high azimuthal anisotropy and the decrease of the shear-wave splitting during a 10 month period suggested a high connectivity of fractures in this area. Connectivity may be a result of a large fault trending through the area causing fracturing or the high well density in the area or both. An enhanced natural fracturing system, along with hydraulic fractures created during the completion of the wells, would allow for high azimuthal anisotropy and a decrease of the shear wave splitting during production (as the crack system closes within the reservoir).

## 5.6 Assumptions and Shortcomings of P-wave Azimuthal Anisotropy Analysis

P-wave azimuthal anisotropy analysis has provided an important tool to characterize many reservoirs. The main advantage lies in the use of a well established and conventional technique to obtain additional information.

In the case of Rulison there are four main factors that provide additional difficulty to correlate EUR and fractures with azimuthal anisotropy analysis based on P-wave. These are: (1) multiple sets of fractures, (2) sandstone net pay distribution (3) fault distribution, and (4) compartments within the reservoir.

Additional factors can involve the quality of the acquisition and processing sequence. The high levels of noise, static analysis, and high density velocity analysis can create anomalies not related with sub-surface changes. Also, stress changes may affect adjacent formations through a process called stress arching.

Xu (2006) and Vasconcelos and Grechka (2006) made P-wave NMO ellipses analysis at Rulison Field. Xu (2006) suggested that the most serious problem in the estimation of the NMO ellipses was the bias observed for different superbins sizes. The NMO ellipticity systematically increases over the area when the superbins size was increased. This change in the NMO ellipticity was produced by the lateral heterogeneity at Rulison Field (NMO ellipses in the reservoir have very small eccentricity).

### 5.6.1 Multiple Sets of Fractures

Figure 5-11 shows the results (at left) from Matesic (2007) and the suggested relation of the structural features with a left-lateral shear model (at right). The faults have a N30°W and N60°E orientation. The natural open fractures have a N80°W orientation

with variations of  $\pm 15$  degrees. This result correlates with the orientation obtained from the azimuthal anisotropy analysis from P-wave data. The healed fracture sets have a main orientation N30°W, with secondary orientations N80°W and N70°E. Faults and two sets of resistive fractures could be explained as Riedel conjugate shear fractures (Matesic, 2007).

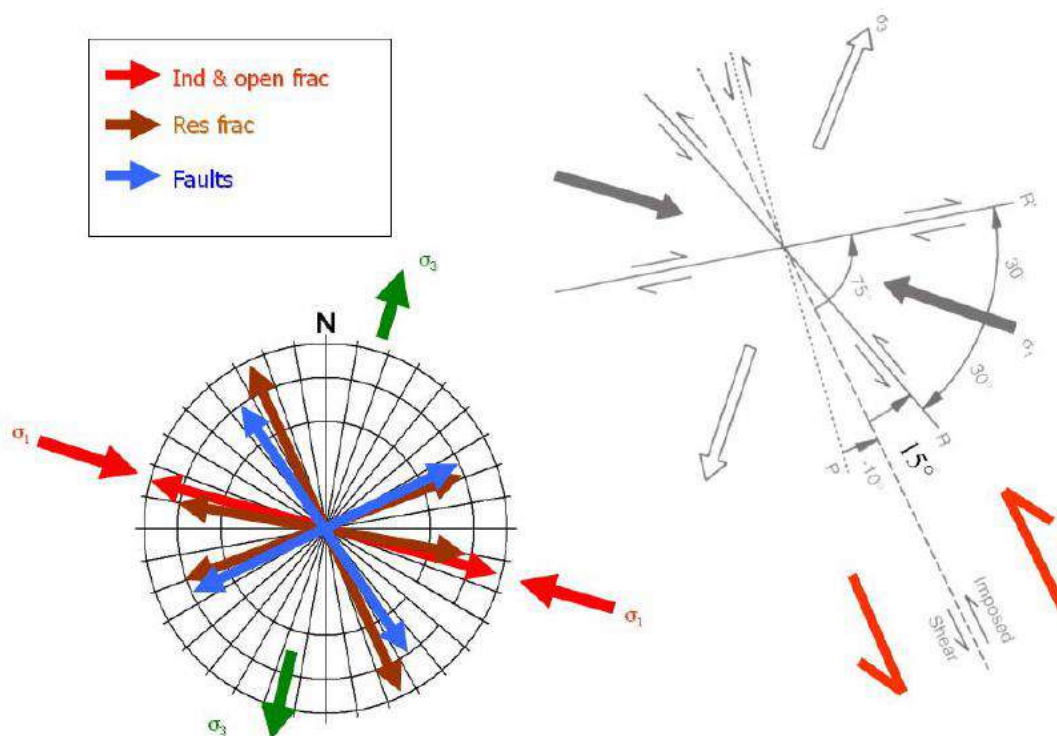


Figure 5-11. Left-lateral shear model proposed for Rulison Field. The arrows in the sketch (at left) represent the mean of interpreted structural features. Present-day stress orientation shows the same orientation of the stress axes as the proposed model (extension of the Piceance basin). Abbreviations: Ind frac=drilling induced fractures, Res frac= natural resistive (healed) fractures, and Open frac = natural open fractures. From Matesic (2007).

Matesic (2007) results can be correlated with previous studies made by Kuuskraa et al. (1997a), Gomez et al. (2003), and Cummella and Ostby (2003).

The presence of multiple sets of fractures is a strong limitation to the use of P-wave to characterize the reservoir. From the well logs, different fracture sets can be observed in the field. At the west side of Rulison Field, there is a predominant set of fractures (orientation east-west) that provides a strong azimuthal anisotropy observed with P-wave. On the east side, the sets of fractures have more than one preference direction of orientation (Vasconcelos and Grechka, 2006).

### **5.6.2 Sandstone Net Pay Distribution**

The relation between net sands and Estimated Ultimate Recovery (EUR) is difficult to establish in tight gas sandstones. Figure 5-12a shows a crossplot between EUR and net pay where there is little correlation between both parameters. This lack of correlation indicates that additional factors existing in the field affect production, and the possible explanation can be found in the fault and fracture areas. Figure 5-12b presents a map of the net pay thickness at Rulison Field. The sandstones are concentrated in the southwest quadrant of the field, and this area correlates with the highest number of wells and gas production.

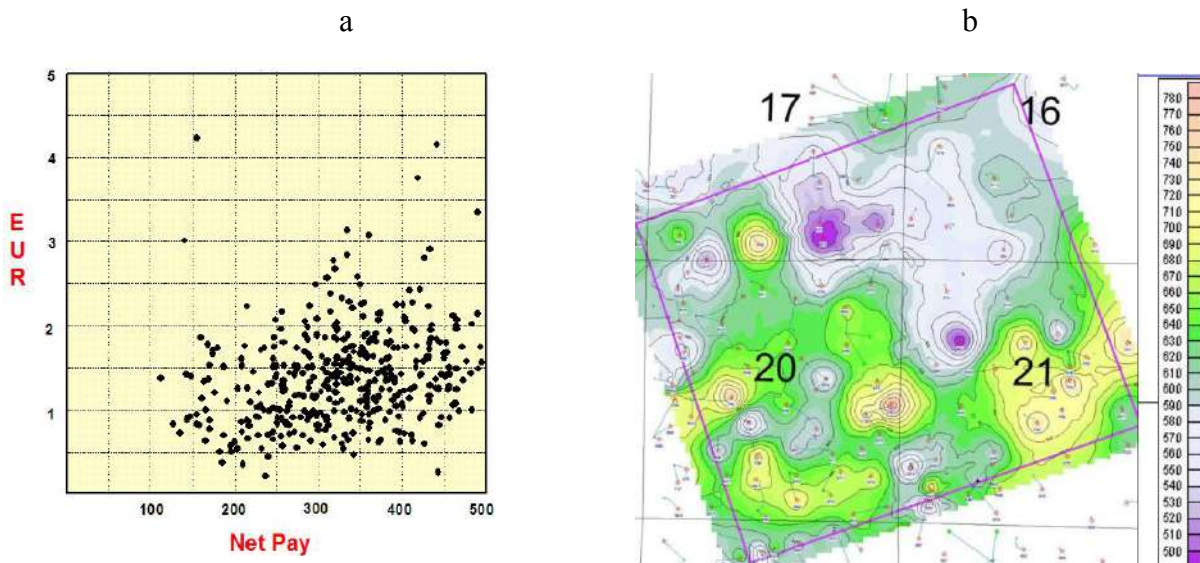


Figure 5-12. a) Estimated Ultimate Recovery (EUR) vs. Net Pay. b) Net Pay thickness map from Williams Company.

### 5.6.3 Fault Distribution

There are areas at Rulison Field that show multiple fracture sets. These fractures are associated with faults in the vicinity of wells RWF 542-20 and RMV 60-17. This structural complexity was shown by Labarre (2006) using shear wave surface seismic (Figure 5-13).

Fault distribution is of extreme importance at Rulison Field. In most of the studies at the survey, there is a significant difference in the seismic properties and attributes between the east and west side of the RCP area (separated by a fault). The P-wave azimuthal anisotropy analysis is not an exception, and the boundaries of the azimuthal anisotropy zones are delineated by faults in the Cameo interval shown in Figure 5-13.

Matesic (2007) suggested that the best wells, in terms of estimated ultimate recovery, are spaced away from Labarre's (2006) seismic interpreted fault by 600 ft. He

provided two possible explanations: (1) Wells close to the fault penetrate relatively small compartments and (2) fault zone has excessive permeability, which causes partial leakage and poor gas production. An additional explanation of the low P-wave azimuthal anisotropy percentage in this middle area is the presence of multiple set of fractures and higher fracture density close to the main fault. Therefore, as the production wells depleted the reservoir the fractures could closed and reduce the P-wave azimuthal anisotropy.

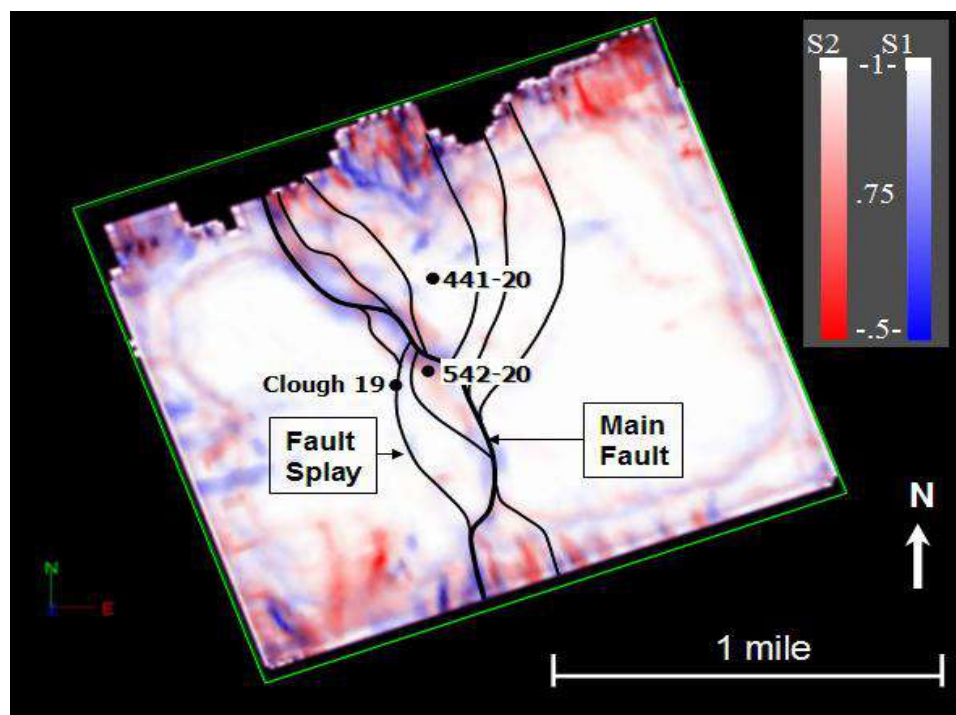


Figure 5-13. Similarity volumes for  $S_{11}$  (pure fast shear, in red) and  $S_{22}$  (pure slow shear, in blue) at the Cameo interval (depth slice of 7080). Color bar: “1” means that there are no trace-to-trace differences. “.5” means that there is a 50% change in the wavelet shape from one trace to the next. Linear feature (possible fault) is interpreted with the dashed line. Modified from LaBarre (2006).

#### 5.6.4 Compartments

Strike-slip faults or wrench faults caused by stresses are believed to be the main cause of fracturing at Rulison Field. Strike-slip faults form in response to horizontal shear movement within the subsurface. Strike-slip faults are characterized by a linear or curvilinear displacement zone in plan view (Christie-Brick and Biddle, 1985). Other features include oversteps, branching, and braiding. The branching of the faults is produced by the stress redistribution related to faulting.

The stepovers combined with the palm tree structures generate fault blocks within the principal displacement zone. The fault blocks create compartments within the reservoir and provide an attractive objective to identify. Jansen (2005) suggested the existence of pressure difference between closely spaced wells, especially in an east-west direction. A reservoir 13 miles southeast of the survey area is compartmentalized by a series of fault blocks (Hoak and Klawitter, 1997).

Kuuskræa et al. (1997a) suggested that fault planes terminate within mid pay sections and splay into a wedge of fracture systems characterized by reflector offset, amplitude dimming, and generally poor amplitude coherency. He observed that areas where faults splay into the reservoir are more likely to be naturally fractured, increasing the well productivity. Jansen (2005) showed that the faults at Rulison Field are extensive faults and splay upward into the reservoir zone. Natural fractures are strongly controlled by fault intersections that experience extension.

Figure 5-14b shows a cross-section southwest-northeast with several wrench faults interpreted from Jansen (2005). The splays advanced from Cameo into the reservoir indicate possible areas of fractures. Two major factors are suggested for the discontinuous character of wrench faults: lithology variations and non-uniformities in the tectonic stress field.

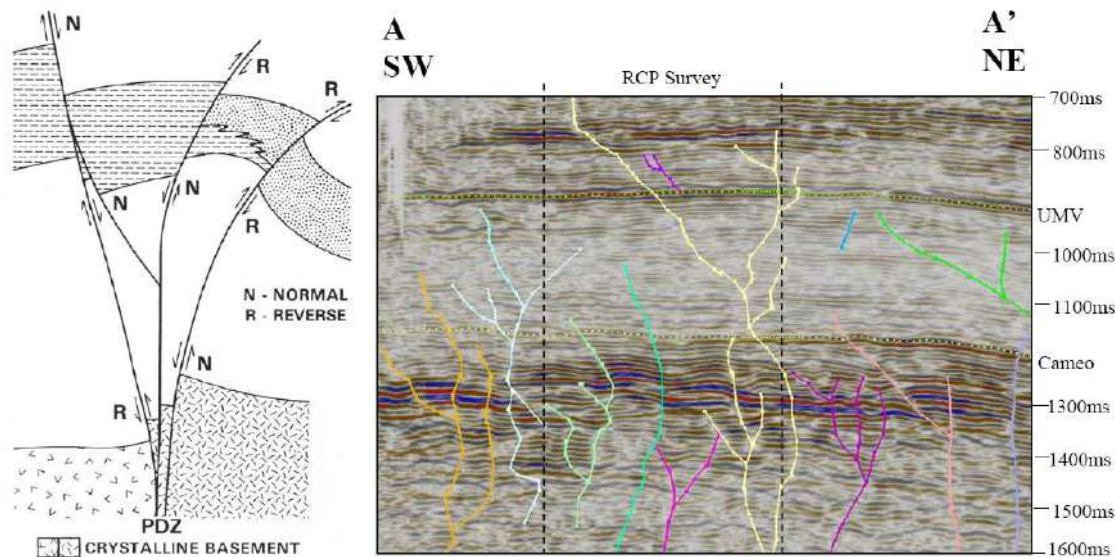


Figure 5-14. a) Schematic showing idealized wrench faults. The splays are referred to as palm tree structures. At the splays' zone, the location of fracture areas and increased well productivity are expected. From Christie-Blick and Biddle (1985). b) Cross-section showing fault system and wrench faults at Rulison Field. RCP survey area is outlined by dotted lines. Vertical exaggeration is close to 20 times. From Jansen (2005).

## 5.7 Shear Wave Splitting Surface Seismic Analysis

Jansen (2005) and Rumon (2006) used shear wave splitting in post-stack data to generate aerial maps of possible fracture zones at Rulison. They suggested that shear wave splitting within the reservoir would help to detect fractures areas. Figure 5-15 shows the calculation of shear-wave splitting coefficient between the UMV and Cameo horizons. Most of the shear-wave splitting coefficient values are in the range of 0% to 5%. These indicate that the shear wave splitting within the reservoir is small, as shown in Chapter Three with the cross-dipole analysis. Also, in the 2003 survey, there is a division between the east and west side of the survey as in the P-wave azimuthal anisotropy

analysis. Both studies show a higher azimuthal anisotropy on the west side of the survey, which correlates with areas of high well density and highly induced fractures.

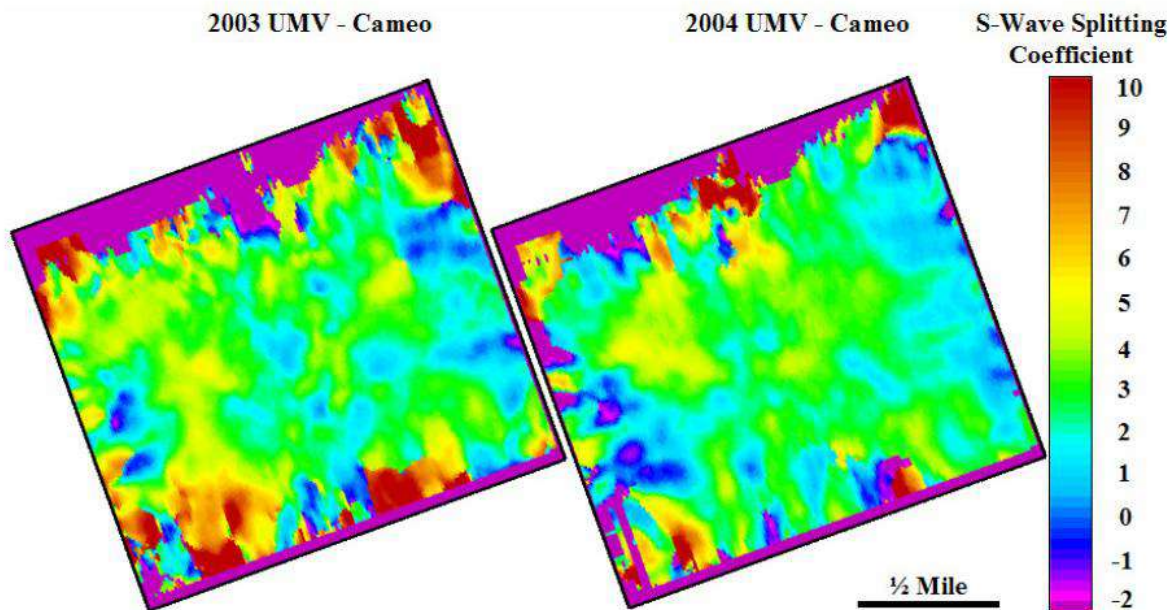


Figure 5-15. Shear-wave splitting coefficients calculated between the UMV and Cameo horizons for the 2003 and 2004 surveys. From Rumon (2006).

## 5.8 Summary

The results show a high azimuthal anisotropy area on the west side of the RCP area that correlates with uplift blocks created from faults below Cameo coal. Also, the orientation of the fractures has been calibrated with well logs providing an N70°W to N85°W direction that correlates with previous estimates from well logs and Vertical Seismic Profile data.

The azimuthal anisotropy analysis is a key method in the identification of fracture systems. The processing sequence to produce the final fractogram volumes produced

coherent results that were calibrated with the well information of the area. In this study, results of this analysis were shown using the most common data available in the market (P-wave). In the case where only one set of fractures exists, a good correlation between production areas and possible high fracture density zones might exist.

There is a poor correlation between the P-wave NMO ellipses and EUR at Rulison Field. This lack of correlation could be caused by the small value of the eccentricity at the reservoir interval and geological factors, such as: (1) multiple sets of fractures, (2) sandstone net pay distribution, (3) fault distribution, and (4) compartments.

Other studies (Vasconcelos and Grechka, 2006, Xu, 2006, Labarre, 2006) have shown the advantages of integrating multicomponent data for the estimation of areas of fractures at Rulison field. For most of the current seismic datasets, where only P-wave data are available, a detailed study of the azimuthal anisotropy can provide valuable insight into the fracture systems and target interest areas with minimal additional time effort and cost.

## CHAPTER 6

### CONCLUSIONS AND RECOMMENDATIONS

#### 6.1 Conclusions from this Study

As the demand for energy increases, the need for unconventional resources will expand, providing challenges to scientists and engineers around the world. Understanding of seismic anisotropy is needed for characterization of a tight gas reservoir.

Based on my study of seismic anisotropy at Rulison Field, I conclude:

1. Tight gas sandstones at Rulison Field are anisotropic. Results from VTI and orthorhombic P-wave inversion show that anisotropy parameters vary and correlate with lithology (sandstones, siltstones, coals, and shales) and are influenced by fractures (mainly in coal layers) at reservoir overburden.

2. Azimuthal anisotropy is evident at small and medium offsets; its orientation varies from north to north-west within the VSP interval (700 feet) at reservoir overburden. This azimuthal anisotropy suggested that the overburden symmetry is at least orthorhombic.

3. Sandstones and shaley sandstones in the overburden are anisotropic. Their mean values of  $\delta$ ,  $\eta$  and  $\varepsilon$  are 10%, 8% and 19% respectively. This determination was made from P-wave inversion of the VSP in the well RMW 30-21.

4. Sandstones, shaley sandstones and siltstones of Mesaverde Group from cores in the well MWX-1 assuming a VTI symmetry have  $\varepsilon$  values from 4 to 15%,  $\gamma$  values from 1 to 5% (without include fracture areas),  $\delta$  values from 2 to 9%,  $\eta$  values from 2 to

5%, and  $\sigma$  values from 3 to 11%. All these values were positive and reflected only the anisotropy due to lithology and heterogeneity (mainly laminations) in core sample matrix.

5. A correlation exists between high shear wave splitting and lithologies from UMV shale to the Rollins Formation marker. Results from crossdipoles well logs shows that high shear wave splitting zones from UMV shale to the Rollins Formation are mainly distributed in sandstones and coals. The quantity of fractures tends to increase four times their density in the coal zones (below Cameo coal).

6. Crossdipoles well logs shows a correlation between high shear wave splitting areas and gas concentrations in the gas production area (below KMV gas marker). This correlation suggests that perforations should be made in high shear wave splitting (more than 4%) and gas rich intervals to take advantage of natural fracture systems. The good correlation between fractures and gas concentrations suggests that gas migration is enhanced by the natural fracture system at Rulison Field.

7. P-wave interval NMO ellipses showed high azimuthal anisotropy anomalies area on the west side of the RCP survey. This anomaly correlates with uplift blocks created by faults below Cameo coal level. Also, the orientation of the fractures has been calibrated with well logs providing an N70°W to N85°W direction that correlates with previous estimates from well logs and Vertical Seismic Profile data.

8. There is a poor correlation between P-wave NMO azimuthal anisotropy and EUR. The poor correlation is caused by small eccentricity values of the P-wave NMO ellipses at the reservoir intervals. There are four geological factors that cause additional difficulty in correlating EUR with P-wave NMO azimuthal anisotropy. These are: (1) multiple sets of fractures, (2) sandstone net pay distribution (3) fault distribution, and (4) compartments within the reservoir. These factors provide limitations in the study of fracture systems using only P-wave information.

9. Multicomponent data provides additional and valuable information to characterize tight gas sandstone reservoirs. The use of P-wave information is important but not enough to characterize different fracture networks at Rulison Field.

## 6.2 Recommendations

From the RCP study at the Rulison Field new questions have arisen about the application of geophysical methods to improve the reservoir characterization. We are just starting to understand the challenges and difficulties that tight gas sands present and further research work needs to be done. A list of recommendations for future work includes:

- Use the seismic anisotropy parameters from the 2003 VSP (Chapter Four) to create and compare isotropic versus anisotropic seismic imaging.  $\delta$  and  $\eta$  values should provide an improvement in the seismic section, especially for areas of relative structural complexity, such as faults.
- Use the 2006 VSP to estimate seismic anisotropy parameters. This VSP can provide continuous seismic anisotropy parameters within the reservoir (60 channels tool from UMV shale to Cameo coal).
- Measure ultrasonic core samples in shales and coals. Measurements in Chapter Two provide results for sandstones, shaley sandstones and siltstones within Rulison Field. A study in coals and shales will provide key information to complete the overall picture of seismic anisotropy in tight gas sands reservoirs.
- Measure core samples at seismic frequencies in the laboratory.

- Compare results of P-wave azimuthal anisotropy for different tight gas sandstones reservoirs. A complete study of the capabilities of P-waves at Rulison will provide an overall picture of the effectiveness of this method in tight gas sands.
- Study effects of stress induced anisotropy in the field. In this study we found a relation of anisotropy with lithology and fractures. Further studies are needed to relate seismic anisotropy in tight gas sands with stress effects in the field.

## REFERENCES

- Alkhalifah, T. and I. Tsvankin, 1995, Velocity analysis for transversely isotropic media: *Geophysics*, 60, 1550-1566.
- Bakulin, A., V. Grechka and I. Tsvankin, 2000, Estimation of fracture parameters from reflection seismic data – Part II: Fractured models with orthorhombic symmetry, 65, 1803-1817.
- Bakulin, A., A. Mateeva, R. Calvert, P. Jorgensen, and J. Lopez, 2007, Virtual shear source makes shear waves with airguns: *Geophysics*, 72, in print.
- Briceno, G., 2004, Rock and fluid properties II: Reservoir Characterization Project Report, Spring 2004 Sponsor Meeting, Colorado School of Mines, Golden.
- Burke, L., 2005, Anisotropy from RWF 542-20 crossdipole sonic log analysis; Reservoir Characterization Project Report, Spring 2005 Sponsor Meeting, Colorado School of Mines, Golden.
- Christie-Blick, N. and K. T. Biddle, 1985, Deformation and basin formation along strike-slip faults. Strike-slip deformation, basin formation, and sedimentation: *Society of Economic Palaeontologist and Mineralogist, Special Publication*, 37, p 1-34.
- Cole, R., and S. Cumella, 2003, Sand-body architecture in the Lower Williams Fork Formation, Coal Canyon, Colorado: *The Mountain Geologist*, v.42, p. 85-107.
- Corrigan, D., R. Withers, J. Darnall, and T. Skopinsky, 1996, Fracture mapping from azimuthal velocity analysis using 3-D surface seismic data, 66th Ann. Internat. Mtg., Soc. Explor. Geophys., Expanded abstracts, 1834-1837.
- Craft, K., S. Mallick, L. Meister and R. Van Dok, 1997, Azimuthal anisotropy analysis from P-wave seismic traveltime data, 67th Ann. Internat. Mtg., Soc. Explor. Geophys., Expanded abstracts, 1214-1217.
- Cumella, S.P., and D.B. Ostby, 2003, Geology of the basin-centered gas accumulation, Piceance Basin, Colorado. Piceance Basin 2003 Guidebook: Rocky Mountain Association of Geologists, 171-193.

Cumella, S.P., 2006, Overview of a giant basin-centered gas accumulation, Mesaverde Group, Piceance Basin, Colorado, in S.A. Sonnenberg, and E.D. Dolly, eds., *The Mountain Geologist*, A special theme issue on Rocky Mountain gas reservoirs revisited. Rocky Mountain Association of Geologists, v. 43, No. 3, p. 219-224.

Davis, T., 2005, Phase XI proposal: Integrating dynamic data into high resolution reservoir characterization II – Time-lapse multicomponent seismic, geomechanical modeling and flow simulation at Rulison field, Colorado School of Mines.

de Parscau, J., 1991, P- and SV-wave Transverse isotropic phase velocity analysis from VSP data: *Geophysical Journal International*, 107, 629–638.

Dewangan, P. and V. Grechka, 2003, Inversion of multicomponent, multiazimuth, walkaway VSP data for the stiffness tensor: *Geophysics*, 68, 1022-1031

Gaiser, J.E., 1990, Transverse isotropic phase velocity analysis from slowness estimates: *Journal of Geophysical Research*, 95, 241-254.

Gomez, L., J. F. W. Gale, S. E. Laubach, and S. Cumella, 2003, Quantifying fracture intensity: An example from the Piceance basin, in K.M. Peterson, T. M. Olsen, and D.S. Anderson, eds., *Piceance basin 2003 guidebook*: Rocky Mountain Association of Geologists, p. 96 -113.

Gray, D., S. Boerner, D. Todorovic-Marinic and Y. Zheng, 2003, Fractured Reservoir Characterization AVAZ on the Pinedale Anticline, Wyoming: *CSEG Recorder*,40-46.

Grechka, V. and I. Tsvankin, 1999, 3-D moveout velocity analysis and parameter estimation for orthorhombic media, *Geophysics*, 64, 820-837.

Grechka, V., and A. Mateeva, 2007, Inversion of P-wave VSP data for local anisotropy: Theory and a case study: *Geophysics*, submitted.

Guliyev, E., 2007, Vp/Vs estimation from multicomponent seismic data for improved characterization of a tight sandstone gas reservoir, Rulison Field, Colorado. M.S. thesis, Colorado School of Mines.

Halliburton, 2006. RWF 441-20 XRMI Processing.

Hemborg, H. T., 2000, Gas production characteristics of the Rulison, Grand Valley, Mamm Creek, and Parachute Fields, Garfield County, Colorado: Turning marginally economic Basin-centered Tight-Gas Sands into profitable reservoirs in the southern Piceance Basin: *Colorado Geological Survey, Resource Series 39*, p. 1-30.

Higgins, S., 2006, Geomechanical modeling as a reservoir characterization tool at Rulison field, Piceance basin, Colorado. M.S. thesis, Colorado School of Mines.

Hoak, T.E. and Klawiter, A.L., 1997, Prediction of fractured reservoir production trends and compartmentalization using an integrated analysis of basement structures in the Piceance Basin, western Colorado, in T.E. Hoak, A. L. Klawitter, and P.K. Blomquist, eds., *Fractured reservoirs: characterization and modeling*: Rocky Mountain Association of Geologist Guidebook, p. 67-102.

Horne, S., and S. Leaney, 2000, Short note: Polarization and slowness component inversion for TI anisotropy: *Geophysical Prospecting*, 48, 779–788.

Hsu, K., M. Schoenberg, and J. Walsh, 1991, Anisotropy from polarization and moveout: 61st Annual International Meeting, SEG, Expanded Abstracts, 1526–1529.

Jackson, J., 2007. Personal communication.

Jansen, K., 2005, Seismic investigation of wrench faulting and fracturing at Rulison Field, Colorado. M.S. thesis, Colorado School of Mines.

Jilek, P., B. Hornby, and A. Ray, 2003, Inversion of 3D VSP P-wave data for local anisotropy: a case study: 73<sup>rd</sup> Annual International Meeting, SEG, Expanded Abstracts, 1322-1325.

Johnson, R.C., 1989, Geologic history and hydrocarbon potential of Late Cretaceous-age, low-permeability reservoirs, Piceance Basin, western Colorado, United States Geological Survey Bulletin 1787-E, 51 p.

Keighley, D., 2006, P-wave Time Lapse seismic data interpretation at Rulison Field, Piceance Basin, Colorado. M.S. thesis, Colorado School of Mines.

Koepsell, R., S.P. Cumella and D. Uhl, 2003, Applications of borehole images in the Piceance Basin in K.M. Oeterson, T.M. Olsen and D.S. Anderson, eds. *Piceance Basin 2003 guidebook*: Rocky Mountain Association of Geologists, p. 233-251.

Kusuma, M., 2005, Analysis of time-lapse P-wave seismic data from Rulison field, Colorado. M.S. thesis, Colorado School of Mines.

Kuuskraa, V. A., T. Barrett, R. Mueller, and J. Hansen, 1997a, Reservoir characterization for development of Mesaverde Group sandstones of the Piceance

Basin, Colorado, in E. B. Coalson, J. C. Osmond, and E. T. Williams, eds., Innovative applications of petroleum technology guidebook: Rocky Mountain Association of Geologists, p. 61 - 72.

Kuuskraa, V. A., D. Vello, and H. Lynn, 1997b, Optimizing technologies for detecting natural fractures in the Tight gas sand of the Rulison Field, Piceance Basin. National Energy Technology Laboratory.

Kuuskraa, V.A., D. Campagna, I. Drayton, F. Joyce, G. Koperna, J. Kuuskraa, and M. Marquis, 1999, Portfolio of emerging natural gas resources, Rocky Mountain Basins, Section 2. Piceance Basin: Advanced Resources International Inc., 45 p.

Labarre, E., 2006, Fault and fracture characterization from multi-component seismic: Reservoir Characterization Project Report, Fall 2006 Sponsor Meeting, Colorado School of Mines, Golden.

Lynn, H.B., C. Bates, K. Simon, and R. Van Dok, 1995, The effects of azimuthal anisotropy in P-wave 3-D seismic, 65th Ann. Internat. Mtg., SEG, Expanded abstracts, 727-730.

Lynn, H.B., D. Campagna, K.M. Simon, and W.E. Beckham, 1999, Relationship of P-wave seismic attributes, azimuthal anisotropy, and commercial gas pay in 3-D P-wave multiazimuth data, Rulison Field, Piceance Basin, Colorado, Geophysics, 64, 1293-1311.

Lorenz, J.C., D.M. Heinze, J.A. Clark, and C.A. Searls, 1985, Determination of widths of meander-belt sandstone reservoirs from vertical downhole data, Mesaverde group, Piceance Creek Basin, Colorado: AAPG Bulletin, v. 69, p. 710-721.

Lorenz, J. C., and S. J. Finley, 1991, Regional fractures II: Fracturing of Mesaverde reservoirs in the Piceance basin, Colorado: AAPG Bulletin, v. 75, p. 1738 – 1757.

Lorenz, J. C., 2003, Fracture systems in the Piceance basin, overview and comparison with fractures in the San Juan and Green River basin, in K.M. Peterson, T. M. Olsen, and D.S. Anderson, eds., Piceance basin 2003 guidebook: Rocky Mountain Association of Geologists, p. 75 -94.

Maggon, L. B., and W. G. Dow, 1994, The petroleum system – from source to trap: AAPG Memoir 60, p. 3-24.

Matesic, M., 2007, Structural and stratigraphic controls on Mesaverde reservoir performance: Rulison Field, Garfield County, Colorado. M.S. thesis, Colorado School of Mines.

Mattocks, B., 2004, Rulison 3D-VSP Polarization Analysis. Reservoir Characterization Project Fall 2004 Sponsor Meeting, Colorado School of Mines.

Mavko, G., T. Mukerji, and J. Dvorkin. The rock physics handbook: Tools for seismic analysis in porous media: Cambridge University Press, 1998.

McCallister, T., 2000. Impact of unconventional gas technology. Annual energy outlook 2000. Department of Energy, Energy Information Association Report.

Reinecke K.M., D.D. Rice and R.C. Johnson, 1991, Characteristics and development of fluvial sandstone and coalbed reservoirs of Upper Cretaceous Mesaverde Group, Grand Valley field, RMAG Guidebook, 209-225.

Reinecker, J., O. Heidbach, M. Tingay, B. Sperner, and B. Muller, 2005, The 2005 release of the World stress map.

Rojas, E., 2005, Elastic rock properties of tight gas sandstones for reservoir characterization at Rulison field, Colorado. M.S. thesis, Colorado School of Mines.

Rumon, M., 2006, Shear wave time-lapse seismic monitoring of a tight gas sandstone reservoir, Rulison field, Colorado. M.S. thesis, Colorado School of Mines.

Sattler, A., 1989, Core analysis in low permeability sandstone reservoir: Results from Multiwell Experiment: Sandia National Laboratories report SAND89-0710, UC-92a, p.58.

Scheevel, J. and S. P. Cumella, 2005, Stratigraphic and rock mechanics control of Mesaverde gas distribution: Piceance Basin, Colorado: RMAG PTTC Fall Symposium. Low Permeability Reservoirs in the Rockies. Denver, Colorado.

Sondergeld, C., and C.S. Rai, 1986, Laboratory observations of shear wave propagation in anisotropic media: The Leading Edge, 11, no.2, 38-48.

Spencer, C.W., 1989, Review of characteristics of low-permeability gas reservoirs in Western United States: AAPG Bulletin, v. 73, p. 613-629.

- Springer, J., 1987, Stress orientations from wellbore breakouts in the Coalinga region: *Tectonics*, v. 6, p. 667-676.
- Thomsen, L., 1986, Weak elastic anisotropy: *Geophysics*, 51, 1954-1966.
- Thomsen, L., 2002, Understanding seismic anisotropy in exploration and exploitation: SEG/EAGE Distinguished Instructor Short Course Lecture Notes, No. 5.
- Tsvankin, I., and L. Thomsen, 1994, Nonhyperbolic reflection moveout in anisotropic media: *Geophysics*, 59, 1290–1304.
- Tsvankin, I., 1997, Anisotropic parameters and P-wave velocity for orthorhombic media: *Geophysics*, 62, 1292–1309.
- Tsvankin, I. Seismic signatures and analysis of reflection data in anisotropic media: Elsevier, 2001.
- Vasconcelos, I. and V. Grechka, 2006, Seismic characterization of multiple fracture sets from multicomponent, multiazimuth, 3D data: Rulison Field, CO: CWP Project Review.
- Wang, Z., 2002a, Seismic anisotropy in sedimentary rocks, part 1: A single-plug laboratory method: *Geophysics*, 67, 1415-1422.
- Wang, Z., 2002b, Seismic anisotropy in sedimentary rocks, part 2: Laboratory data: *Geophysics*, 67, 1423-1440.
- Wolhart, S.L., Odegard, C.E., Warpinski, N.R., Waltman, C.K., and Machovoe, S.R., 2005, Microseismic fracture mapping optimizes development of low-permeability sands of the Williams Fork Formation in the Piceance Basin. 2005 SPE Annual technical conference and exhibition, Dallas, TX, SPE# 95637.
- Xu, X., 2006, Anisotropic geometrical spreading correction and its application in azimuthal AVO analysis. Ph.D. thesis, Colorado School of Mines.